AN ABSTRACT OF THE DISSERTATION OF

Robert Kykyneshi for the degree of Doctor of Philosophy in Materials Science presented on October 29, 2007.

Title: Pulsed Laser Deposition and Thin Film Properties of p-type BaCuSF, BaCuSeF, BaCuTeF and n-type $Zn_2In_2O_5$ Wide Band-Gap Semiconductors.

Abstract approved:_____
Janet Tate

Thin films of wide band-gap semiconductors are deposited by the pulsed laser deposition method. Optimal deposition parameters for the individual compounds are reported. A family of *p*-type BaCuQF (Q = S, Se, Te) ceramics with a layered crystalline structure is investigated for active and passive device applications. Epitaxial films of BaCuTeF are grown *in-situ* on single-crystal MgO substrates. These films exhibit a maximum hole mobility of 8 cm^2/Vs and conductivity of 167 S/cm. The band gap of BaCuTeF is 3 eV, much higher than 2.3 eV expected from powder results. BaCuSeF textured films are also grown on MgO substrates with a lower 1.5 cm^2/Vs and 1.7 x 10^{18} cm^{-3} carrier concentration. Crystalline films of BaCuSF are obtained by post-annealing in H_2S and Ar gases. Excitonic absorptions above 3 eV in BaCuSeF and BaCuSF indicate the upper limit of photon transmission. Various photoluminescence colors in the visible range are observed under UV excitation. The $Zn_2In_2O_5$ (ZIO) is also a layered semiconductor, but with electron majority carrier-type. Amorphous and crystalline ZIO films have 2 x 10^3 S/cm conductivity and indirect band gaps between 2.8 and 3.2 eV, respectively. The amorphous phase is stable to high temperature exposure up to 500˚C.

Pulsed Laser Deposition and Thin Film Properties of p-type BaCuSF, BaCuSeF, BaCuTeF and n-type $Zn_2In_2O_5$ Wide Band-Gap Semiconductors

by

Robert Kykyneshi

A DISSERTATION

submitted to

Oregon State University

in partial fulfillment of
the requirements for the
degree of

Doctor of Philosophy

Presented October 29, 2007
Commencement June 2008

Doctor of Philosophy dissertation of Robert Kykyneshi presented on October 29, 2007

APPROVED:

Major Professor, representing Materials Science

Director of the Materials Science Program

Dean of the Graduate School

I understand that my dissertation will become part of the permanent collection of Oregon State University libraries. My signature below authorizes release of my dissertation to any reader upon request.

Robert Kykyneshi, Author

ACKNOWLEDGEMENTS

I want to express my gratitude to my major professor, Janet Tate, for many years of support, teaching and training. To Douglas Keszler, John Wager, David McIntyre and Brady Gibbons go my sincere thanks for their helpful guidance in the progress of my research work. For materials synthesis, sample characterization, everyday interactions, talks, and friendship, I want to acknowledge the present and past members of the Tate Group, Keszler Group, Wager Group: Paul Newhouse, Andriy Zakutaev, Ben Nielsen, Cheol-Hee Park, Peter Hersh, Heather Platt, Joayoung Jeong, Matt Spiegelberg, Jack Spies, David Hong and Richard Schafer. I want to thank David Johnson, John Donovan, Kurt Langworthy and Daisuke Ito of the University of Oregon for help with thin film characterization. To Ted Hinke and Joe Magner in recognition of their help in building and fixing research tools. This research work was funded by NSF grants No. DMR-0071727 and DMR-00245386 and the Hewlett-Packard Company.

To my dear wife for lots of encouragement, and to my son for happy moments of distraction feeling him build those muscles and vital neuropathways which will serve him well in his life to come. My deep appreciation goes especially to my parents, for giving me this life, teaching me by example the pleasure of hard work well done, and for all their good advice.

TABLE OF CONTENTS

TABLE OF CONTENTS (Continued)

Page

TABLE OF CONTENTS (Continued)

Page

LIST OF FIGURES

LIST OF FIGURES (Continued)

Figure Page

LIST OF FIGURES (Continued)

LIST OF FIGURES (Continued)

Figure Page

LIST OF FIGURES (Continued)

Figure Page

LIST OF FIGURES (Continued)

Figure Page

LIST OF FIGURES (Continued)

Figure Page

LIST OF TABLES.

Chapter 1. Introduction

The aim of this research work is to prepare wide band gap semiconductor thin films with hole- and electron-majority carriers using pulsed laser deposition (PLD). The significant thin film deposition parameters of the PLD method are described in Chapter 2, along with the characterization methods used throughout this work. Chapters 3, 4, and 5 present results thin films of BaCuQF (Q = S, Se, Te) – a new family of transparent *p*-type semiconductors. The PLD method is also used to prepare amorphous and crystalline thin films of wide band gap *n*-type $Zn_2In_2O_5$, presented in Chapter 6. This dissertation is concluded by a summary of main results, proposed future work on BaCuQF materials for electronics application, and a few technical notes. The layout of this dissertation is presented in Fig. 1.1.

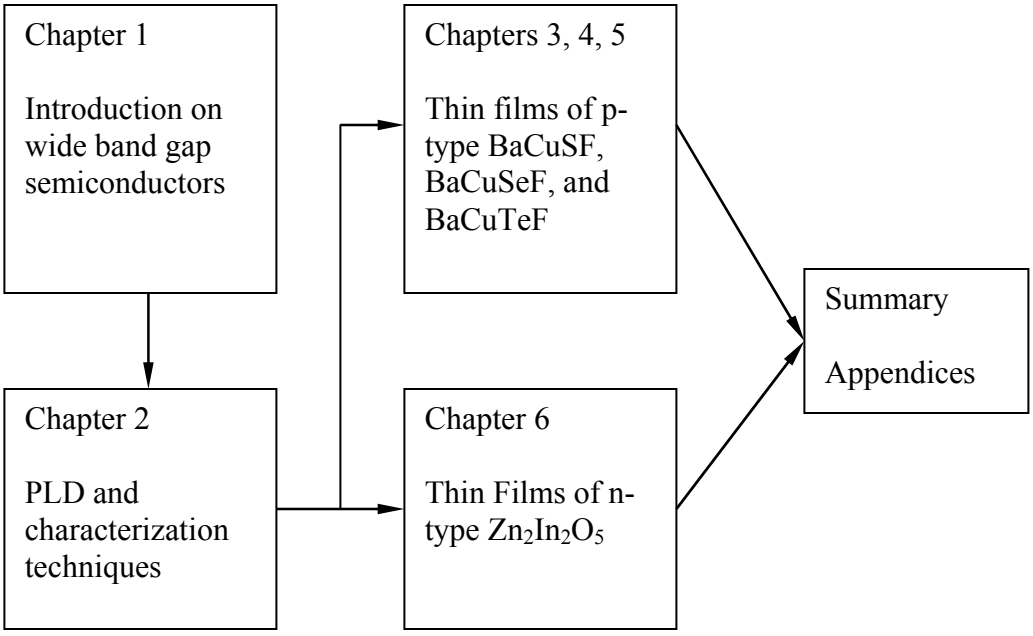

Figure 1.1. Schematic layout of the dissertation.

Semiconductors are an essential part of our everyday life found at the core of all electronics devices. These devices are Si-based structures with ~ 1eV band-gap, which can easily be doped electron or hole carrier-type. Such devices are not transparent to visible light because of the low band gap. A wide, 3.1 eV or larger, band gap semiconductor, on the other hand, is transparent to all visible light and allows for applications such as low-emissivity window coatings, electrodes in flat panel displays, window layers of solar cells, etc. The well- and long-known representatives of this class of semiconductors are In_2O_3:Sn (ITO) [1] and ZnO [2] of electron carrier-type. Because most developed transparent semiconductors are oxides, a collective name of transparent conductive oxides or TCOs has been introduced.

A new application possibility of transparent electronics [3] arose with the development of $CuAlO_2$ [4]) thin films in 1997 – the first transparent conductive oxide with hole majority carriers (*p*-TCO). Since then, many compositions of the delafossite $A^+M^{3+}O_2^{2-}$ structure have been studied with A = Cu, Ag, and M = Sc, Cr, In, Ga, *etc*. [for example 5,6,7]. Higher visible transparency AMO_2 films invariably resulted in lower conductivity, and low mobility was reported. Moreover, the preparation of films involved high temperature processing making *p*-type oxides of the delafossite structure unattractive for transparent thin film transistor (TTFT) or solar cell blocking contact applications. Transparent *p*-*n* junctions were, however, fabricated using $CuYO_2$ [8] and $CuInO_2$ [9].

Meanwhile, development of *n*-type TTFT devices had begun for higher performance flat panel displays [10]. The first TTFT of only TCO materials consisted of a ZnO-channel, ITO source/drain/gate and Al_2O_3-TiO_2 (ATO) insulator layers [11],

with performance comparable to Si-based devices. Discovery of many other TCOs for transistor applications followed with high channel mobility >10 cm^2/Vs (compared to 1 cm^2/Vs in a-Si), such as ZnO/SnO_2 [12], In_2O_3 – 10 wt.% ZnO [13], and $InGaO_3(ZnO)_5$ [14] to name a few. In particular, TTFT devices using In_2O_3/Ga_2O_3 (IGO) [15] as channel layer were used to prepare the first transparent electrical circuit (an inverter and a ring oscillator) [16].

The inability to achieve good electrical characteristics while maintaining low optical absorption in the delafossite compounds caused the search for alternative materials such as BaCuQF and LaCuOQ (Q = S, Se, Te), where wide band gaps coexist with hole conductivity. Epitaxial LaCuOS and LaCuOSe thin films are reported to possess hole mobility up to ~8 cm^2/Vs [17]. Upon doping with R^{2+} (R = Mg, Sr) cations on the La site, degenerate conductivity has been achieved [17,18], maintaining an over 60% transparency in the visible range. Although such properties are highly desirable for transparent electronics, the preparation method of these films in an evacuated sealed tube at high temperatures (~1000˚C) is unsuitable for effective implementation in devices. Other emerging *p*-type conductors are $BaCu_2Q'_2$ [19] and SrCuQ′F [19,20] (Q′ = S, Se) have so far been studied only in the powder form.

We thus study thin films of BaCuQF (Q = S, Se, Te) in an effort to produce *in-situ* high quality films at low temperatures. BaCuQF belongs to the P4/nmm space group with a tetragonal lattice structure, shown in Fig. 1.2a, isostructural to LaCuOQ. The lattice consists of alternating Cu-Q and Ba-F sheets stacked upon one another. BaF_2 is a wide band gap insulator, while CuQ_x compounds are well-known *p*-type

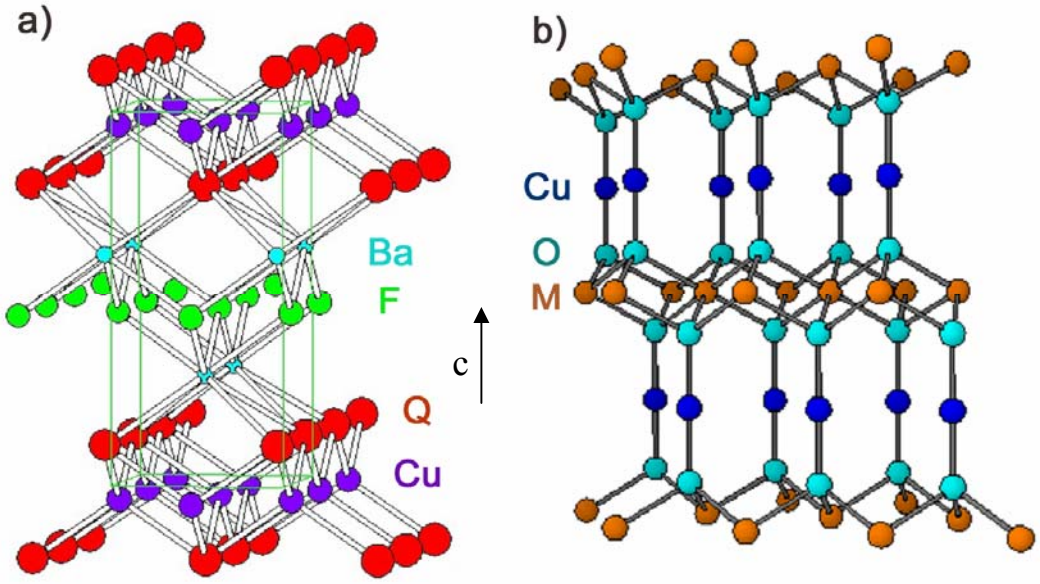

Figure 1.2. Crystal structures of a) BaCuQF and b) $CuMO_2$.

conductors. Such a layered structure is expected to exhibit anisotropic electrical and optical properties. For instance, electrical conductivity is expected to be high in the *ab*-plane due to $(Cu_2Q_2)^{2-}$ layers, but strongly suppressed along the *c*-direction. Also, improving conductivity is anticipated from changing the chalcogen anion from S to Te, due to the higher covalency of Cu-Te bonds. The larger anion, however, increases the lattice volume and a decrease in optical band gap usually occurs. For reference the crystallographic parameters of BaCuQF compounds are summarized in Table 1.1.

A higher conductivity is expected in BaCuQF, and LaCuOQ, compared to the delafossite $CuMO_2$ materials. As already noted, the conduction in BaCuQF takes place in the $(Cu_2Q_2)^{2-}$ layer, where hole transport can occur through the ...-Cu-Q-Cu-Q-... linkages. Such linkage is absent in $CuMO_2$ (Fig. 1.2b) and conduction takes place along the …-Cu-O-M-O-Cu-… bonds, strongly inhibiting carrier mobility and

Table 1.1. Lattice parameters of BaCuQF compounds. The unit cell is tetragonal of the P4/nmm space group.

Name	a (Å)	c (Å)	V (Å^3)	Ref.
BaCuSF	4.1220	9.0143	156.16	[21]
BaCuSeF	4.2391	9.1217	163.92	[22]
BaCuTeF	4.4297	9.3706	183.87	[28]

electrical conductivity anisotropy introduced by the layered crystal lattice [23]. Oxygen intercalation into the Cu-layer provides a more direct conduction path and creates additional carriers in $CuMO_2$ with M = Sc or larger cation [24], also leading to increased absorption in powder and thin film, shown for $CuScO_2$ [25]. The anisotropy of the BaCuQF structure yields high carrier mobility in epitaxial films, but is a disadvantage in case of polycrystalline films due to misalignment of the conduction planes.

Band structures of BaCuQF are shown in Fig. 1.3. The calculations are carried out using commercially available Wien2K software package [26], utilizing the linearized augmented plane wave (LAPW) method. First, we note that BaCuQF compounds are direct band gap semiconductors, where the conduction band minimum (CBM) and valance band maximum (VBM) both occur at the Γ-point. The band gap shrinks with larger chalcogen atom (S $\rightarrow$ Se $\rightarrow$ Te). Indeed, diffuse reflectance measurements on powders show a decrease in band gap from 3.1 eV for BaCuSF to 2.9 eV for BaCuSeF [27], and to 2.3 eV for BaCuTeF [28]. Such behavior is due in part to the increasing unit cell volume, and in part to higher covalency of the Cu-Q bonds with larger Q anion, strongly affecting the CBM and the VBM.

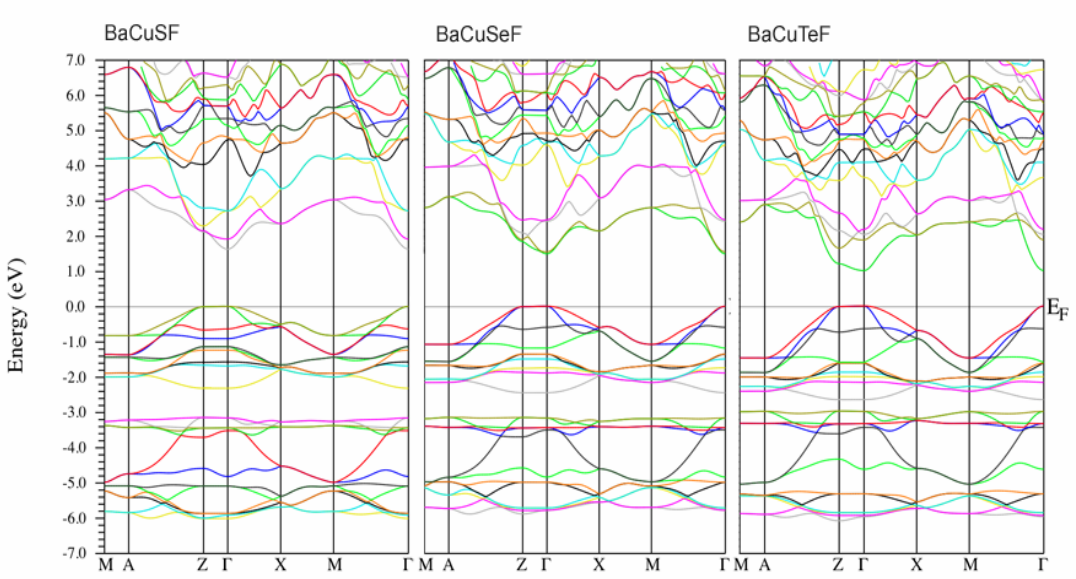

Figure 1.3. Band structures of BaCuQF, with Q = S, Se, Te from left to right, respectively [29,28]. The band gap is direct and decreases with larger chalcogen anions.

Next, we note the anisotropy in band curvature at the VBM with lattice direction. High dispersion in the density of states, indicating high carrier mobility, is seen in the Γ-M, Γ-X, X-M and A-Z directions, all corresponding to *k*-vectors pointing along the (CuQ)-planes. Additionally, the dispersion increases with larger chalcogen atom (left to right Fig. 1.3), due to increasing Cu-Q bond covalency. In the direction perpendicular to the layers, such as Γ-Z and M-A in Fig. 1.3, the bands are flat and lower mobility is expected. The CBM and the VBM are composed mainly of Cu 4*s* orbitals and of Cu 3*d* and Q n*p* orbital mixing, respectively. Based on these contributions to the VBM and CBM and their dispersion, it is concluded that carriers are confined into the $(Cu_2Q_2)^{2-}$ layer in BaCuQF. This leads to interesting properties as high hole mobility and excitons described in this work.

Electrical conductivity measurements of pressed powders show increasing conductivity from 0.07 S/cm in BaCuSF and BaCuSeF [30] to 7 S/cm in BaCuTeF [28], and a crossover from activated/hopping conduction mechanism to metal-like, respectively. The hole majority carrier-type is determined from Seebeck coefficient measurements, yielding values around +50 μV/K. Similar values of the Seebeck coefficients in BaCuQF indicate comparable carrier concentrations. The much higher conductivity in BaCuTeF could be then explained by improved hole mobility. It is believed that hole carriers in undoped BaCuQF are a result of Cu vacancies (V_{Cu}), but oxygen substitution on F-sites is also possible. Further increase in conductivity can be achieved by up to 10% K-doping on the Ba site, creating more hole carriers. This was successfully shown in BaCuSF and BaCuSeF powders [30].

Achieving high conductivity, however, is not the primary aim of this work on BaCuQF materials. The prospective applications of these materials are as active channel layers in transparent electronics and wide-band gap p^+-contacts in solar cells. In the former case a low carrier concentration and high carrier mobility are required for transistor operation. In the latter case a high carrier concentration is the critical factor. Processing conditions, such as low temperatures, cheap substrates and preparation methods are important issues for implementation in devices. Both applications require the thin film form, and that is why we study the preparation methods and properties of BaCuSF, BaCuSeF and BaCuTeF thin films, described in Chapters 3, 4, and 5.

An electron carrier transparent conductive oxide is also investigated in this thesis. Research efforts are focused on new high conductivity materials, containing

little or no indium, due to its scarcity and thus high cost. For example, such alternative materials are In_2O_3-$(ZnO)_k$ (k = 1 - 90) in the amorphous and crystalline phases [31,32], ZnO [2] and CdO [33] compounds.

Electrical properties of In_2O_3-$(ZnO)_k$ pressed powder pellets [34] with various ZnO content reveals that the highest conductivity of phase pure material is achieved in $Zn_3In_2O_6$, and decreases with higher ZnO content. A wide composition range of In_2O_3-$(ZnO)_k$ has been studied in the thin film form. Metastable crystalline phases of $ZnIn_2O_4$ and $Zn_2In_2O_5$ [31], not accessible in bulk at room temperature [34], were realized and found to be the most conductive within the In_2O_3-$(ZnO)_k$ (k = 1 - 90) family of materials. The unit cells of the compounds form a layered structure [35] with k ZnO layers between In_2O_3 layers. The unit cell structure of In_2O_3-$(ZnO)_k$ is orthorhombic or hexagonal for odd or even values of k, respectively. The full details of the structure are not available in the literature at this time.

We chose the $Zn_2In_2O_5$ (ZIO) composition for further research (see Chapter 6) because PLD-deposited ZIO film properties have not yet been studied in detail and this particular target composition was readily available. The literature indicates that the band gap of ZIO is indirect and about 2.9 eV [36]. ZIO films deposited by dc and rf sputtering methods are shown to possess high carrier concentration ($6 - 7 \times 10^{20}$ cm^{-3}) and electron mobility (20 – 30 cm^2/Vs), resulting in conductivities as high as 1400 – 3000 S/cm [36,37]. These reports include the effects of substrate temperature and oxygen partial pressure in the deposition gas on the physical properties of the ZIO films and serve as a benchmark for our research. Although a report on preparation of the $Zn_2In_2O_5$-phase film by PLD, amongst other

compositions, is available [31], the film properties are evaluated only for one set of deposition parameters: 500˚C substrate temperature and ~10^{-3} Torr oxygen pressure. In the present work the effects of laser fluence, substrate temperature and oxygen partial pressure on the physical properties of ZIO thin films are described.

References

1. Flexible Flat Panel Displays, Ch.5, Edited by G.P. Crawford, John Wiley & Sons 2005
2. R. Wang, L. L. H. King, and A. W. Sleight, J. Mater. Res. 11 (1996) 1659
3. G. Thomas, Nature 389 (1997) 907
4. H. Kawazoe, M. Yasukawa, H. Hyodo, M. Kurita, H. Yanagi, H. Hosono, Nature 389 (1997) 939
5. J. Tate, M.K. Jayaraj, A.D. Draeseke, T. Ulbrich, A.W. Sleight, K.A. Vanaja, R. Nagarajan, J.F. Wager, R.L. Hoffman, Thin Solid films 411 (2002) 119
6. H. Yanagi, T. Hase, S. Ibuki, K. Ueda, H. Hosono, Appl. Phys. Lett. 78 (2001) 1583
7. A.N. Banerjee, K.K. Chattopadhayay, Review Article, Progress in Crystal Growth and Characterization of Materials 50 (2005) 52
8. M.K. Jayaraj, A.D. Draeseke, J. Tate, A.W. Sleight, Thin Solid Films 397 (2001) 244
9. H. Yanagi, K. Ueda, H. Ohta, M. Orita, M. Hirano, H. Hosono, Solid State Commun. 121 (2001) 15
10. J. F. Wager, Science 300 (2003) 1245
11. R, L. Hoffman, B. J. Norris, and J. F. Wager, Appl. Phys. Lett. 82 (2003) 733
12. W. B. Jackson, R. L. Hoffman, G. S. Herman, Appl. Phys. Lett. 87 (2005) 193503
13. B. Yaglioglu, H. Y. Yeom, R. Beresford, and D. C. Paine, Appl. Phys. Lett. 89 (2006) 062103

14. K. Nomura, H. Ohta, K. Ueda, T. Kamiya, M. Hirano, and H. Hosono, Science 300 (2003) 1269
15. H. Q. Chiang, D. Hong, C. M. Hung, R. E. Presley, J. F. Wager, C.-H. Park, D. A. Keszler, G. S. Herman, J. Vac. Sci. Technol. B 24 (2006) 2702
16. R. E. Presley, D. Hong, H. Q. Chiang, C. M. Hung, R. L. Hoffman, J. F. Wager, Solid-State Electronics 50 (2006) 500
17. H. Hiramatsu, K. Ueda, H. Ohta, M. Hirano, T. Kamiya, and H. Hosono, Appl. Phys. Lett. 82 (2003) 1048
18. H. Hiramatsu, M. Orita, M. Hirano, K. Ueda, and H. Hosono, J. Appl. Phys. 91 (2002) 9177
19. C.-H. Park, Phd thesis, Oregon State University, 2005, Call# LD4330 2005D .P37
20. H. Kabbour, L. Cario, S. Jobic, and B. Corraze, J. Mater. Chem 16 (2006) 4165
21. C.-H. Park, Phd thesis, Oregon State University, 2005, Call# LD4330 2005D .P37
22. JCPDS #82-1492
23. A. W. Sleight, private communication
24. M. Elazhari, A. Ammar, M. Elaatmani, M. Trari, J. P. Doumerc, Eur. J. Solid State Chem. 34 (1997) 503
25. R. Kykyneshi, B. C. Nielsen, J. Tate, J. Li, A. W. Sleight, J. Appl. Phys. 96 (2004) 6188
26. P. Blaha, K. Schwarz, G. K. H. Madsen, D. Kvasnicka and J. Luitz, WIEN2k, An Augmented Plane Wave + Local Orbitals Program for Calculating Crystal Properties (Karlheinz Schwarz, Techn. Universitat Wien, Austria), 2001. ISBN 3-9501031-1-2
27. C.-H. Park, D. A. Keszler, H. Yanagi, J. Tate, Thin Solid Films 445 (2003) 288
28. C.-H. Park, R. Kykyneshi, A. Yokochi, J. Tate, and D. A. Keszler, J. Solid State Chem. 180 (2007) 1672
29. H. Yanagi, J. Tate, S. Park, C.-H. Park, D. A. Keszler, M. Hirano, and H. Hosono, J. Appl. Phys. 100 (2006) 083705
30. H. Yanagi, J. Tate, S. Park, C.-H. Park, and D. A. Keszler, Appl. Phys. Lett. 82 (2003) 2814

31. N. Naghavi, C. Marcel, L. Dupont, A. Rougier, J. Leriche and C. Guery, J. Mater. Chem. 10 (2000) 2315
32. B. Kumar, H. Gong and R. Akkipeddi, J. Appl. Phys. 98 (2005) 073703
33. T. O. Mason, G. B. Gonzalez, D. R. Kammler, N. Mansourian-Hadavi, B. J. Ingram, Thin Solid Films 411 (2002) 106
34. T. Moriga, D.D. Edwards, T.O Mason, G.B. Palmer, K.R. Poppelmeier, J.L. Schindler, C.R. Kannewurf and I. Nakabayashi, J. Am. Ceram. Soc. 81 (1998) 1310
35. P. J. Cannard and R. J. D. Tilley, J. Solid State Chem. 116 (1988) 418
36. T. Minami, H. Sonohara, T. Kakumu and S. Takata, Jpn. J. Appl. Phys. 34 (1995) L971
37. T. Minami, T. Kakumu, Y. Takeda, S. Takata, Thin Solid Films 317 (1998) 326

Chapter 2. Film deposition and characterization techniques

2.1. Introduction

Throughout this work thin films of various materials are prepared by the pulsed laser deposition (PLD) technique. The PLD method and laboratory setup are discussed in this chapter. Furthermore, the commonly used characterization methods and tools used are described.

2.2. Pulsed laser deposition

Thin films of various materials presented in this work are produced by pulsed laser deposition (PLD) in an ultra-high vacuum (UHV) custom design chamber (built by Thermionics Inc.) with a base pressure of ~2 x 10^{-9} Torr. A KrF excimer laser (Lambda Physik model Compex 205) is used to produce 20 ns duration pulses at 248 nm with a fluence of 0.5 to 2 J cm^{-2} in a beam diameter at the target of 0.04 cm^2. The number of pulses and repetition rate 1-10 Hz is controlled via a computer. The layout of the experimental setup is shown in Fig. 2.1.

Targets and substrates are introduced via a load-lock. Both target and substrate are rotated during deposition. The substrates are usually fused SiO_2 or single-crystal MgO (100). The substrate preparation procedure involves cleaning the substrate, and optically contacting it to a stainless steel platen. Films deposited at elevated substrate temperature are baked for 60 min. in vacuum at the deposition temperature prior to

deposition. Halogen lamps are used to heat the substrate above room temperature to 650 ± 10˚C.

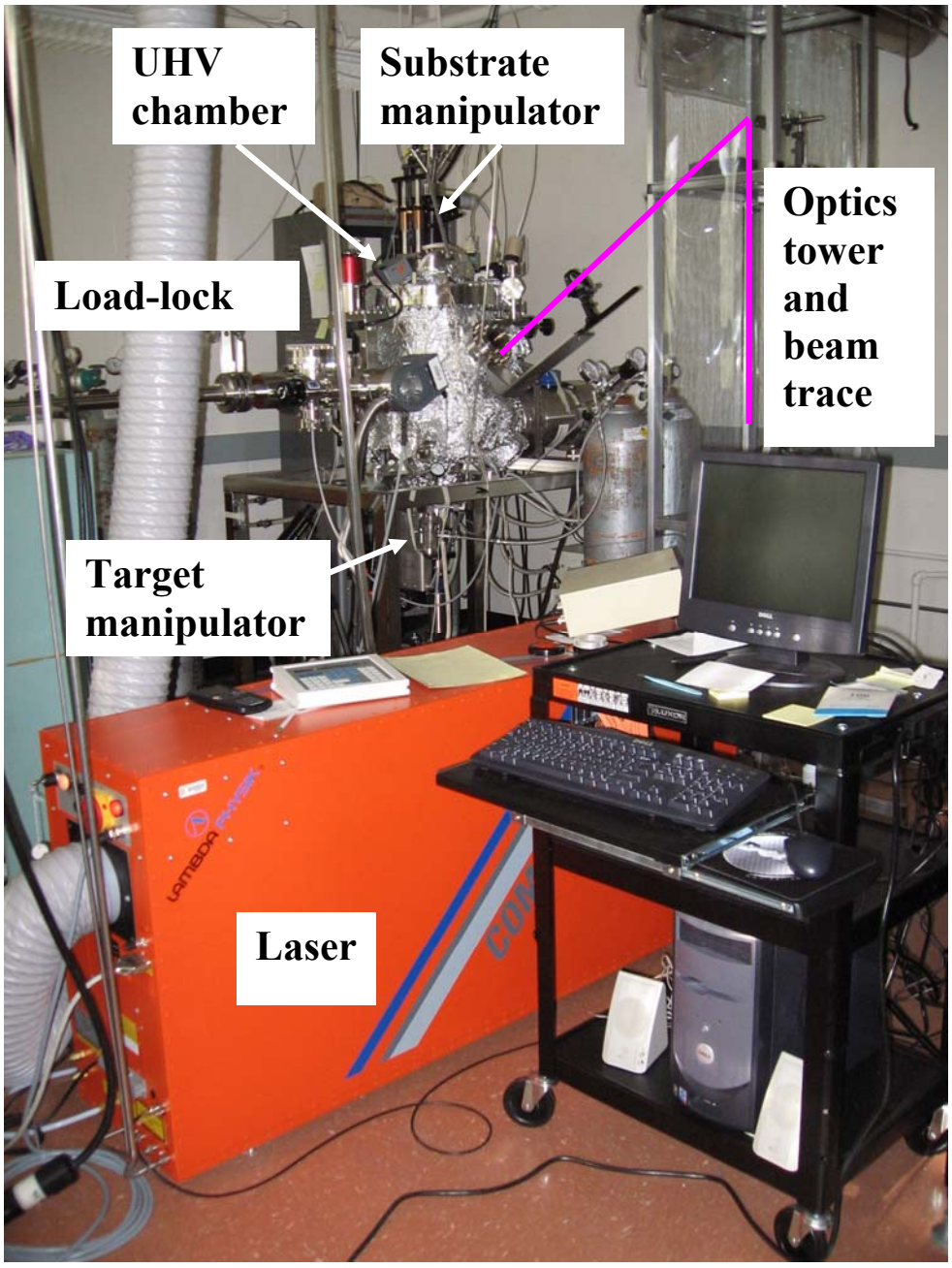

Figure 2.1. PLD system setup.

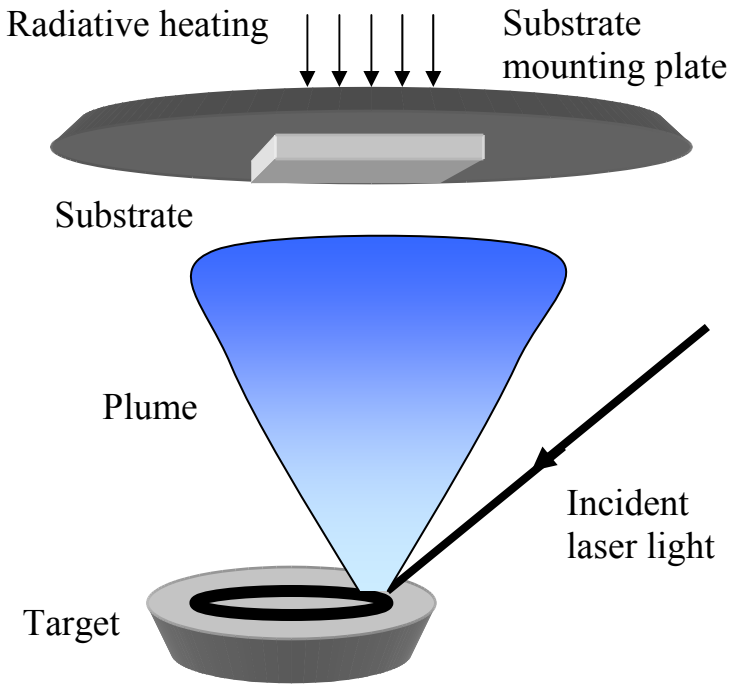

Figure 2.2. Diagram of thin film deposition process by the PLD method.

The deposition geometry is depicted in Fig. 2.2. The focused incident laser beam (45˚ incident angle) is absorbed in a thin surface layer of the target causing local melting, approximately of the same area as of the beam at the target surface and about 1 μm deep [1]. Additional energy supplied to the liquid in the duration of the pulse (~20 ns) causes evaporation and formation of the plume, which is a plasma of the target material species in the form of highly energetic ions and electrons (few 100 eV), neutrals (~10 eV) and particle clusters. The plume species have energies on the order of a few eV and arrive to the substrate surface within about 5 μs, when deposition in vacuum or up to 1 mTorr background gas pressure takes place, typical for films deposited in this work. Considerable increase in travel time occurs at background pressures above 50 mTorr.

A deposition track is formed (Fig. 2.2) on the target surface due to its rotation and repetitive laser pulses. Such deposition geometry leads to formation of cones on the exposed target surface [1]. It has been found that the cone formation is due to phase segregation of the deposited material during recrystallization of the laser-induced melt. The top of the cones consists of the material component possessing the highest melting point. The cone formation is a self-limiting process and does not influence the stoichiometry transfer. In contrast, deposition from pristine target surface is non-stoichiometric due to preferential evaporation of the more volatile components. As the cones get taller a balance of evaporation from the top of the cones and voids in-between is achieved, leading to the desired stoichiometry in the plume. It is therefore important to pre-ablate polished targets. In this work 600 - 700 pulses are used. Yet, target polishing is recommended after exposure to a large number of pulses (many thousands) due to a decreasing deposition rate.

Aside from evaporation of atoms and clusters, larger particulates are also ejected from the hot target surface and settle on the surface of the growing film. Most applications in optics and opto-electronics require smooth surfaces and thus particulates need to be eliminated. Reduction of laser fluence, high target density and high target rotation speed are plausible solutions [1]. During deposition in vacuum the ejected droplets are hot and nanometer-scale size and vaporize in flight, but in the presence of inert ambient gas they can actually grow in size from the vapor phase and reach the substrate 5 cm away.

The quality of the film strongly depends on the deposition parameters such as laser fluence, repetition rate, substrate temperature and deposition gas pressure. The

laser fluence and repetition rate are the parameters that most influence the stoichiometry and morphology, controlling the energy and amount of the saturated vapor arriving at the substrate surface. These two parameters set the deposition rate and affect the structure (polycrystalline to epitaxial) and surface morphology (voids to outgrowths) of the films. Typical growth rates are 0.1 - 2 Å/s, corresponding to 5 Hz and 10 Hz laser pulse repetition rates at 1 J/cm^2. The substrate temperature is essential in growing crystalline films at elevated temperatures.

It is further interesting to note the effect background gas pressure on film growth [1]. In case of a reactive gas, like oxygen for oxide ceramics deposition, it has a positive effect of maintaining target stoichiometry by incorporation in the vapor and film phases. In the presence of an inert gas, the atoms merely slow down the plasma particles somewhat due to collisions. This effect is small due to the low (max 10^{-2} Torr) deposition pressures used in this work. It can be seen in Chapter 5 in the case of $Zn_2In_2O_5$ films, that deposition in 1 mTorr Ar (g) leads to an increase in film quality compared to vacuum deposition under otherwise similar conditions (using heated substrates). The presence of inert gas during deposition could prevent off-stoichiometric growth in BaCuSF thin films. The volatility of the chalcogen atom decreases with larger size, thus S is expected to be the most volatile and Te the least. In fact, BaCuTeF thin films are of the highest quality when background Ar (g) is used during deposition on single crystal substrate (Chapter 4). The volatility of the F atoms can also be of concern.

2.3. Characterization techniques

Thin polycrystalline film X-ray patterns are obtained on a Rigaku Rapid diffractometer equipped with an area detector and a Cu K_α radiation source. The substrate with film on top is mounted on the sample holder and a marker dot is made on the film surface. The dot is used for aligning the sample on the stage with the beam. If the sample is not properly centered, the diffraction peaks skew and broaden. Typical settings for data collection are ϕ = rotation angle, $\omega = 50°$, $\chi = 190°$ and the X-ray shutter is open for 7 min. These settings ensure glancing incidence of X-rays onto the sample surface. A clear advantage of this XRD setup is the continuous data collection at all θ-angles by the area detector for the entire duration of exposure. A polycrystalline film is a conglomeration of randomly oriented crystallites reflecting in all directions, resulting in low intensities reflected into the detector (especially in case of θ-2θ configuration). The simultaneous counting at each 2θ angle allows for measurement of polycrystalline patterns much faster compared to diffractometers of the θ-2θ configuration. The diffraction patterns also show the occurrence of any significant second phase in the thin film samples. The low resolution of the area detector results in a large instrumental broadening of the reflection peaks.

Textured (*c*-axis oriented and epitaxial) films are measured in the θ-2θ configuration, on a Bruker AXS D8 diffractometer, also using Cu K_α radiation. Textured films are typically grown on single crystal (100) MgO substrates in this research, which provides an excellent reference peak for alignment. The measurements are conducted using a 0.02° step in 2θ and ~1 sec integration time at

each step. Thin film heteroepitaxy of a tetragonal lattice on a cubic one is explained here and sketched in Fig. 2.3. Observation of only (00*l*) reflection peaks in a θ-2θ scan suggests *c*-axis oriented thin films, also referred to as orientation in the out-of-plane direction (the plane of the substrate). The intensity of reflected peaks is much higher than in case of polycrystalline films due to the alignment of respective crystallographic planes. The single-crystal MgO substrate (002) reflection has the highest intensity at 2θ = 42.92°, and its observation together with the thin film (00*l*) only reflections prove the out-of-plane alignment of the substrate-film stack, or can be written as $(00l)_{\text{film}}//(00l')_{\text{substrate}}$. To determine epitaxial film growth, the alignment of the film and substrate *ab*-planes (also called in-plane alignment) is required. For a tetragonal lattice (as in case of BaCu(S, Se,Te)F), where the lattice parameters $a = b \neq c$, on cubic (100) MgO substrate ($a' = b' = c'$), it is sufficient to show that $[h00]_{\text{film}}$ and $[h'00]_{\text{substrate}}$ or $[0k0]_{\text{film}}$ and $[0k'0]_{\text{substrate}}$ lattice directions are parallel. Reflections of (*h*00), (0*k*0) and (*hk*0) planes are hard to measure due to the small thickness (~200 nm) of the films. Therefore, in case of BaCu(Se,Te)F films the (102) and the MgO (202) reflections are used to show in-plane alignment. The following equation can be used to find the angle between any arbitrary planes in the tetragonal lattice:

$$\chi = \arccos\left(\frac{\frac{h_1 h_2 + k_1 k_2}{a^2} + \frac{l_1 l_2}{c^2}}{\sqrt{\left(\frac{h_1^2 + k_1^2}{a^2} + \frac{l_1^2}{c^2}\right)\left(\frac{h_2^2 + k_2^2}{a^2} + \frac{l_2^2}{c^2}\right)}} \right) \tag{2.1}$$

where h_1, k_1 and l_1 are the indices of the first plane (or reference plane), h_1, k_2 and l_2 are the indices of the second plane (the sought plane), and *a*, *b* and *c* are the lattice

parameters. In case of a cubic structure the lattice parameter denominators cancel. The χ-angle (Fig. 2.3) between the (00*l*) and (102) planes in BaCuTeF is 46.6˚ (and 45˚ in the case of MgO (100) and (101) planes). Setting the X-ray source and detector to the reference θ and 2θ positions of the BaCuTeF (102) peak (or MgO (202) peak, equivalent to (101) with higher intensity) and scanning along the ϕ-angle (rotation around c-axis parallel to the (00*l*) direction, see Fig. 2.3) should reveal four reflection maxima, because in the tetragonal (and cubic) lattice the sought reflection satisfies Bragg's law only four times upon a 360˚ rotation. Rocking curves, χ- and ϕ-angle adjustment of the particular reflections

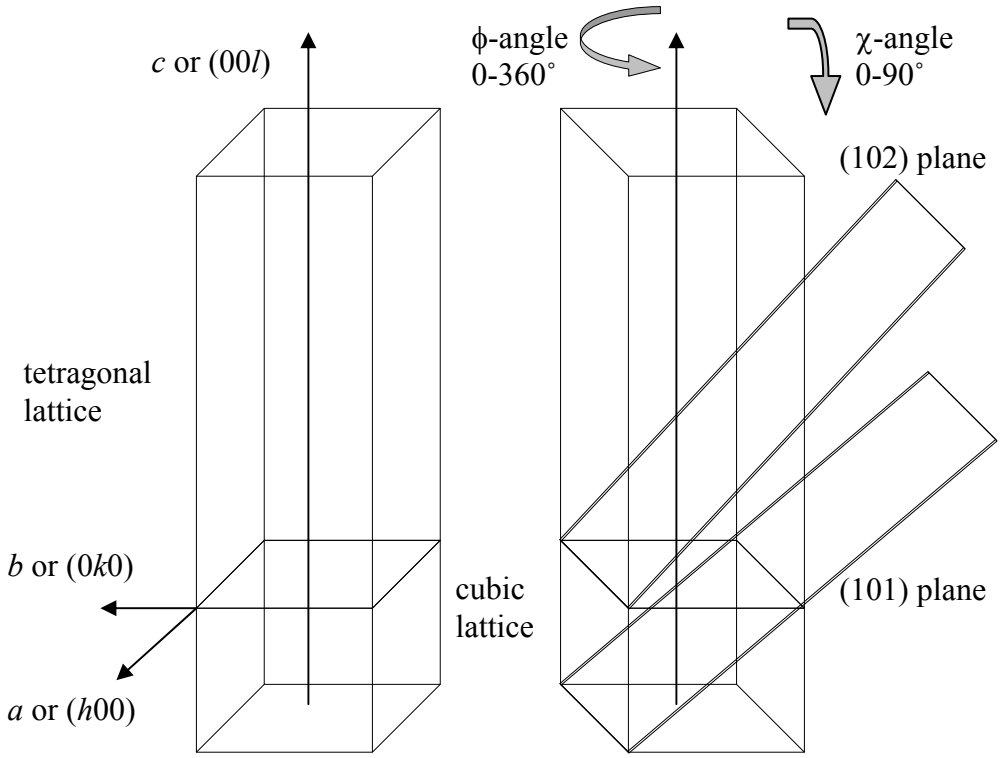

Figure 2.3. Heteroepitaxial film of a tetragonal lattice ($a = b \neq c$) structure on a cubic lattice (a = b = c).

maximizes peak intensity. The occurrence of BaCuTeF (102) and MgO (202) at the same ϕ-angles proves that the $[hk0]_{film}$ and $[hk0]_{substrate}$ directions are parallel. Thus thin film epitaxy is shown with $(00l)_{film}//(00l')_{substrate}$ and $[h00]_{film}//[h'00]_{substrate}$.

Planar and cross-sectional scanning electron microscopy (SEM) images are obtained with an FEI Quanta 200 Environmental SEM (ESEM) [2].

Room temperature thin film conductivity and carrier concentration are measured on a Lakeshore 7504 Hall system in the van der Pauw configuration. The Hall coefficient R_H is given by [3]:

$$R_H = \frac{r\left(p - b^2 n\right)}{q\left(p + bn\right)^2} \tag{2.2}$$

where $b=\mu_n/\mu_p$ is the ratio of electron and hole carrier mobilities in the semiconductor, r is the scattering factor usually set to 1, n and p are electron and hole carrier concentrations in the semiconductor, and q is the electron charge. Experimentally, R_H is calculated using:

$$R_H = \frac{tV_H}{BI} \tag{2.3}$$

where t is the sample thickness, V_H is the Hall voltage, B is the applied magnetic field and I is the applied current. A typical magnetic field range of 5 – 20 kG is used. The majority carrier concentration in the semiconductor is determined from Eq. 2.2 as:

$$p = \frac{r}{qR_H} \quad \text{or} \quad n = -\frac{r}{qR_H} \tag{2.4}$$

given that $p >> n$ in the former case and $p << n$ in the latter case, respectively. The mobility of the majority carriers is then calculated from:

$$\sigma = qN\mu \tag{2.5}$$

where N is the majority electron- or hole-carrier concentration.

Temperature-dependent conductivity measurements from 77 to 300 K are performed in a 4-collinear-probe geometry. Sample conductivity is calculated using [3,4]:

$$\sigma = \ln(2)(\pi t R F)^{-1} \tag{2.6}$$

where R is the measured resistance, t is sample thickness, and F is a product of correction factors due to sample shape and boundary conditions. The influence of the correction factors on the measured conductivity can be over a factor of 5, when the sample size approaches the probe spacing.

The Seebeck coefficient relative to Cu is measured at room temperature or in the 20 – 300 K temperature range using a 3 K temperature gradient. Details of the experimental setup are given in [4].

Optical transmission and reflection of the films and diffuse reflection from powders are obtained using a home-built grating spectrometer in the McIntyre Laboratory in the Department of Physics. The spectrometer sources are an Oriel 250W Xe lamp in the UV-visible spectral range and a tungsten halogen lamp in the near IR range. A double grating monochromator provides monochromatic light with a bandwidth of about 2 nm. A set of 0.25, 0.5, 1 and 2 μm gratings is used to measure optical transmission and reflection spectra in the 0.2 – 0.7 μm, 0.3 – 0.9 μm, 0.8 – 1.7 μm and 1.5 – 2.5 μm ranges, respectively. A Si detector is used in the UV-visible range, and a PbS detector in the IR spectral range up to 2.5 μm. The spectrometer is calibrated against a He-Ne laser and the known positions of the Xe source emission lines. From these measurements, the film thickness, refractive index, and

semiconductor band gap are determined. The analysis of the thin film interference spectra is done in a Microsoft Excel spreadsheet written by David McIntyre and Levi Kilcher [5]. The refractive index does not include corrections for thin film surface roughness and the reported values in this work are an effective refractive index of the film bulk and surface. Diffuse reflection measurements from powders are carried out using an integrating sphere and Si detector in the UV-visible optical range. $BaSO_4$ and MgO are used for reference lamp spectra. The powder band gap is evaluated using the Kubelka-Munk method [6].

The luminescence spectra measurements use a home-built spectrometer in the Keszler laboratory in the Department of Chemistry. A Xe lamp source, two monochromators and a photo-multiplier tube detector are used. Excitation and emission spectra are measured. Typically, 360 nm excitation wavelength is used to obtain the emission spectra.

References

1. Chapters 4,5 and 8; Pulsed Laser Deposition of Thin Films, edited by D.B. Chrisey and G.K. Graham, John Wiley and Sons, (1994)
2. For more information visit www.fei.com
3. D. K. Schroder, Semiconductor Material and Device Characterization, John Wiley and Sons, (2005)
4. R. Kykyneshi, MS thesis, Oregon State University (2004), Call # LD4330 2005 .K95
5. L. Kilcher, senior thesis, Oregon State University (2003), unpublished
6. P. Kubelka and F. Munk, Zh. Tekh. Fiz. 12 (1931) 593; P. Kubelka, J. Opt. Soc. Am. 38 (1948) 448

Chapter 3. Electrical and optical properties of *p*-type BaCuSF thin films

3.1. Introduction

p-Type transparent conductors (*p*-TC) have attracted much attention and research for active and passive electronics applications. Such *p*-TC candidates are $CuMO_2$ (M = Sc, Cr, etc) [1,2], LaCuOQ' (Q' = S, Se) [3,4] and BaCuQF (Q = S, Se, Te) [5,6] together with their doped and solid solution derivatives.

Previous studies of undoped and potassium-doped BaCuSF powders [5] showed relatively high conductivity with band gaps over 3.1 eV, suitable for wide band gap semiconducting materials. BaCuSF films deposited by thermal evaporation and post-annealed in an evacuated sealed tube at 450˚C – 650˚C produced insulating transparent films with an average transmission of ~70% in the visible spectrum [7]. Films prepared by this method are textured (on MgO substrates) and exhibit saturated red luminescence. However, such a sealed-tube annealing method is rather complex and MgO substrates are expensive. A similar difficulty is present in the LaCuOQ family of materials prepared by the reactive solid-phase epitaxy (R-SPE) method [8].

Thin films prepared *in-situ* at elevated substrate temperatures by PLD using BaCuSF targets, resulted in multi-phase samples, mainly consisting of $BaCu_2S_2$. But according to [9], high substrate temperature (≥600˚C) and low laser fluence of 0.5 J/cm^2 (as discussed in section 3.3.2) could possibly yield *in-situ* stoichiometric film growth in the future.

In this chapter the preparation of BaCuSF thin films on fused SiO_2 substrates by three annealing methods is discussed. First, in section 3.3.1 a flowing H_2S (g)

annealing method is employed in an attempt to obtain single-phase BaCuSF films. Next, in section 3.3.2, results of rapid thermal annealed films in Ar (g) are presented, revealing the importance of using low laser power during deposition of amorphous BaCuSF films. The third post-processing method is sealed-tube annealing, resulting in insulating and luminescent BaCuSF films, described in section 3.3.3. This section also includes a description on excitonic absorption near the band edge, and the observed red and green emission spectra of sealed-tube and rapid thermal annealed films, respectively. In an effort to utilize the hole-carrier properties of BaCuSF films, they were incorporated into a thin film transistor; this application is described in section 3.3.4.

3.2. Experiment

Thin films of BaCuSF are deposited by pulsed laser deposition (PLD) from a stoichiometric target of the same compound. A KrF 248 nm excimer laser is used for target ablation with deposition parameters of 0.5 and 2 J/cm^2 laser fluence, 10 Hz repetition rate, 5 – 6.25 cm substrate-target distance, and no substrate heating. The base pressure in the deposition chamber is near 2 x 10^{-9} Torr. Films are deposited in vacuum or 1 mTorr Ar (g). All films in this section are deposited on fused SiO_2 unless specifically stated otherwise. BaCuSF deposited at room temperature results in dark brown-gray, amorphous, insulating, and highly reflective films.

The films are annealed in flowing H_2S gas for 2 h at 240˚C, 280˚C, 325˚C, 550˚C and 650˚C in an alumina-tube furnace. Prior to the H_2S anneal, films are heated

at 6˚C/min under flowing Ar gas, and subsequent to the H_2S anneal are cooled in Ar at the same rate. The thickness of the annealed films is between 250 – 300 nm. BaCuSF films annealed H_2S (g) are discussed in section 3.3.1.

Amorphous BaCuSF films are also rapid thermal annealed (RTA) in Ar (g) at various temperatures, as discussed in section 3.3.2. First, flowing Ar (g) is allowed to displace air in the annealing chamber for 10 min. A quartz lamp heats the substrate to the set temperature in ~1 min, and maintains it for 5 min. The annealed films are then cooled to room temperature within a few minutes.

The third method of BaCuSF film preparation is by annealing the amorphous film in an evacuated tube. In this case, the amorphous films of BaCuSF on SiO_2 substrates are covered with another SiO_2 slide and sealed in an evacuated silica tube with sacrificial BaCuSF powder of equivalent stoichiometry. Films are then annealed for 15h at 650˚C using a 6˚C/min heating/cooling rate. The resulting films exhibit red luminescence and are discussed in section 3.3.3.

3.3. Results

3.3.1. BaCuSF films by H_2S anneal

Hole carriers are believed to be the result of Cu vacancies (V_{Cu}) in the otherwise stoichiometric lattice of BaCuQF (Q = S, Se, Te) materials. In the presence of a V_{Cu}, the Q^{2-} anion attracts an electron from the nearby Cu^{+} atom to complete its *p*-band due to its higher electronegativity. This creates a net positive charge in the

crystal strructure via Cu^{2+} ions. The excess positive charge is mobile and responsible for the *p*-type carriers in these materials. The number of V_{Cu} can be increased by elimination of sulfur vacancies V_S achieved by annealing in H_2S (g). To further increase the carrier concentration, monovalent alkali-metal cations can be substituted on the Ba site. K-doping has proved as a successful dopant in powders [5], but only limited success is achieved in the thin film form, as described below.

To obtain crystalline and V_{Cu} rich BaCuSF thin films, an *ex-situ* annealing in flowing H_2S (g) is employed on amorphous films deposited at room temperature. The relatively high pressure (compared to that in a vacuum chamber) during such annealing inhibits evaporation of volatile components and phase separation.

BaCuSF thin films prepared by PLD at room temperature are amorphous and insulating. Annealing of these amorphous films *ex-situ* in H_2S gas between 280˚C - 650˚C results in crystallization, as indicated by the observation of XRD diffraction peaks in Fig. 3.1, matching those of the BaCuSF powder. Peaks not corresponding to the reference powder BaCuSF pattern are those of BaF_2 and $BaCu_2S_2$. Although primarily polycrystalline BaCuSF phase is observed after a 650˚C anneal, both of these secondary phases are present in the film, probably due to dissociation of BaCuSF especially at high temperatures. The observation of BaF_2 in the films annealed at temperatures lower than 650˚C is related to the high laser fluence of 2 J/cm^2 used for the deposition of the amorphous films, further discussed in the next section. The crystallized surfaces have a high root-mean-square (RMS) roughness of 10 – 25 nm, compared to the smooth ~ 1 nm roughness of the amorphous precursors, measured by AFM.

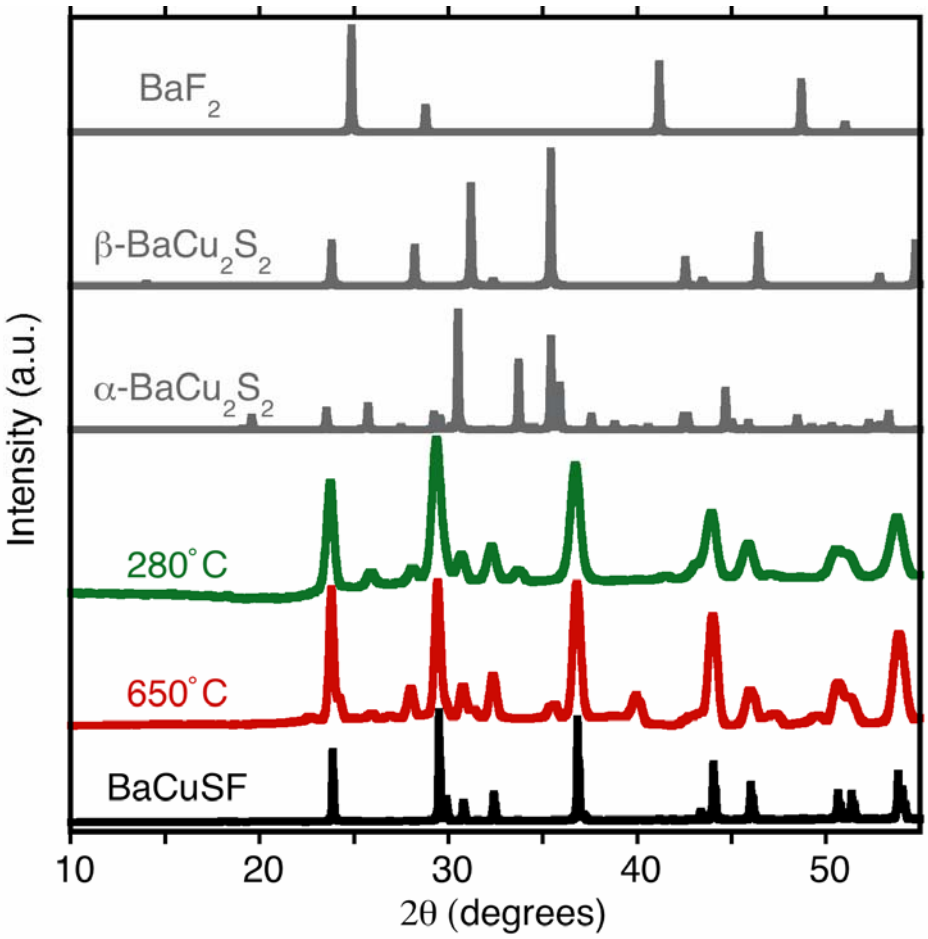

Figure 3.1. XRD patterns of BaCuSF films annealed at 280˚C and 650˚C. The SiO_2 substrate background has been removed. Film reflections are in good agreement with the reference BaCuSF powder pattern (black line). Reference XRD patterns of observed secondary phases are also shown (gray lines).

Annealing at 550˚C and 650˚C results in low conductivities, on the order of ~10^{-5} S/cm. The conductivity of the films is increased by 3 orders of magnitude by lowering the annealing temperature, as depicted in Fig. 3.2. For instance, a 280˚C annealed film has a high conductivity of 5 x 10^{-3} S/cm in undoped BaCuSF thin films. Hall coefficients are not reliably measurable.

The positive sign of the carriers is established by Seebeck coefficient (also called thermopower) measurement of values greater than +200 μV/K, commonly

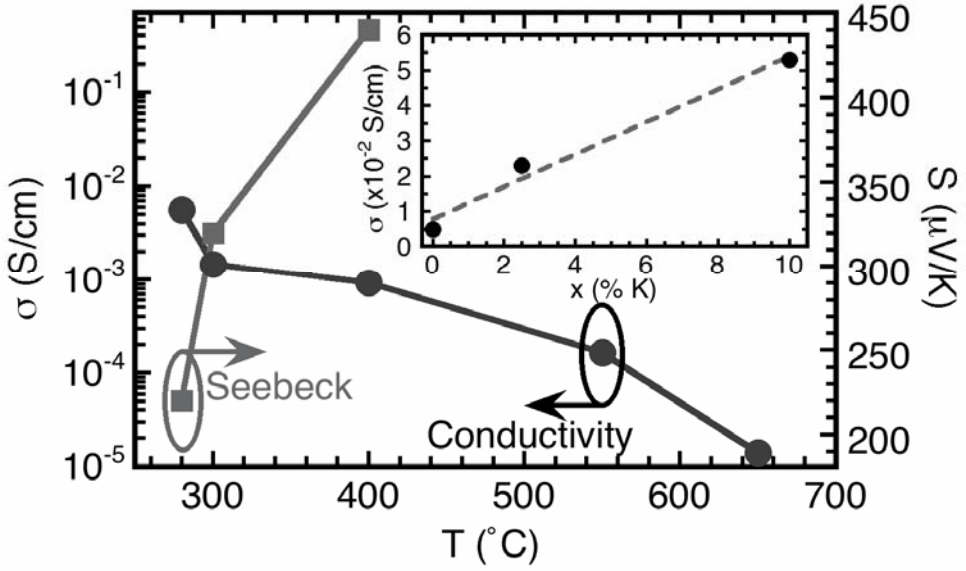

Figure 3.2. BaCuSF thin film conductivity (circles, left scale) and Seebeck coefficient (squares, right scale) as a function of H_2S annealing temperature. Inset: BaCuSF film conductivity increases with larger x in $Ba_{1-x}K_xCuSF$, shown for films annealed at 280˚C.

observed for semiconducting materials. High annealing temperatures > 400˚C produce films of low conductivities, such that thermovoltage measurements are not measurable due high noise levels. Assuming that the small polaron carrier transport mechanism applies, thermopower values Q can be converted to hole concentrations [10] using:

$$Q = +\frac{k_B}{e}\ln\left(\frac{\beta(1-c)}{c}\right) \tag{3.1}$$

where c is the fraction of Cu-sites occupied by holes, β is the degeneracy factor set equal to 2, and k_B and e are the Boltzmann constant and the elemental charge. The theoretical density of Cu sites is $N = 1.51 \times 10^{22}$ cm^{-3}, and the product cN is the carrier concentration estimate. The annealing temperature dependence of the Seebeck coefficient in BaCuSF films is shown in Fig. 3.2. The measured +220 μV/K of the

280˚C annealed film corresponds to a carrier concentration as high as 5.9 x 10^{20} cm^{-3}, according to Eq. 3.1. As the annealing temperature is increased to 300˚C and 400˚C the corresponding carrier concentrations decrease to 1.9 x 10^{20} cm^{-3} and 5 x 10^{19} cm^{-3}, respectively. The reduction in carrier concentration with higher temperature can be explained by the reducing properties of the H_2S (g). On the basis of these carrier concentrations, the carrier mobility μ is estimated at a low 5 x 10^{-5} cm^2/Vs, using Eq. 2.5. It is concluded that the measured 5 x 10^{-3} S/cm conductivity in H_2S (g) annealed polycrystalline BaCuSF films arises from a high carrier concentration, but is limited by carrier mobility.

An increase in conductivity up to 5.3 x 10^{-2} S/cm is obtained in $Ba_{1-x}K_xCuSF$ films from nominally x = 0.025 and 0.10 targets. The conductivity of the films increases linearly with the doping concentration, as shown on the inset of Fig. 3.2 for 280˚C annealing temperature. The modest increase may be due carrier generation in films of already high carrier concentration as estimated above for the undoped film. The presence of K in the films is observed in annealing experiments at temperatures above 400˚C, resulting in reaction of K with the SiO_2 substrate turning it opaque. Quantitative analysis on potassium levels has not been carried out in BaCuSF films or powders. We can conclude that: i) the dopant is transferred from the target to the film during PLD, and ii) K-doping only moderately improves thin film conductivity by introduction of carriers, presumably by substitution of K for Ba.

The high average optical transmission of 72% in the visible range of the spectrum (Fig. 3.3) extends into the infrared region up to 2500 nm. Absorption

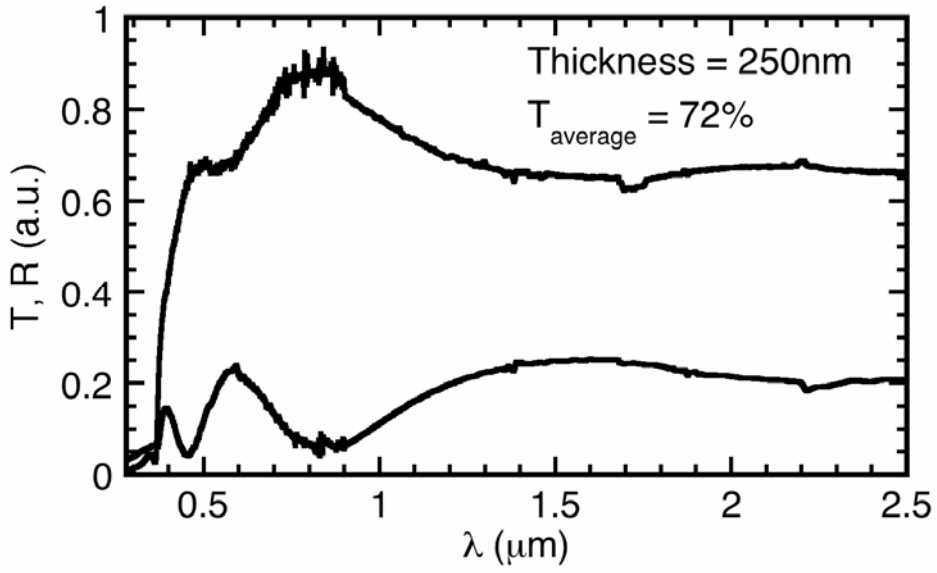

Figure 3.3. Typical transmission and reflection spectra of BaCuSF thin films annealed in H_2S gas at 280˚C – 650˚C (data for 280˚C annealed film shown). The average transparency is calculated in the 400-800 nm range.

coefficients as low as 6200 cm^{-1} are calculated (at 520 nm), and further decrease at longer wavelengths. This value of absorption coefficient is comparable to the delafossite *p*-TCOs of similar conductivity, such as $CuInO_2$ [11] and $CuGaO_2$ [12]. Higher conductivity in acceptor-doped thin films of $CuScO_2$ and $CuCrO_2$ [1,2] have been reported, but a considerable increase in absorption with the higher conductivity is a trait of these materials.

Orders of magnitude increase in conductivity is measured when the annealing temperature of amorphous BaCuSF films in H_2S (g) is further decreased to about 240˚C. The XRD pattern of this low temperature annealed film, shown in Fig. 3.4a, corresponds to hexagonal CuS [JCPDS # 06-0464]. We believe BaCuSF remains amorphous and the CuS crystallizes to due to the reaction of Cu atoms diffusing to the surface of the film in the sulfur-rich atmosphere. Surface analysis by SEM reveals

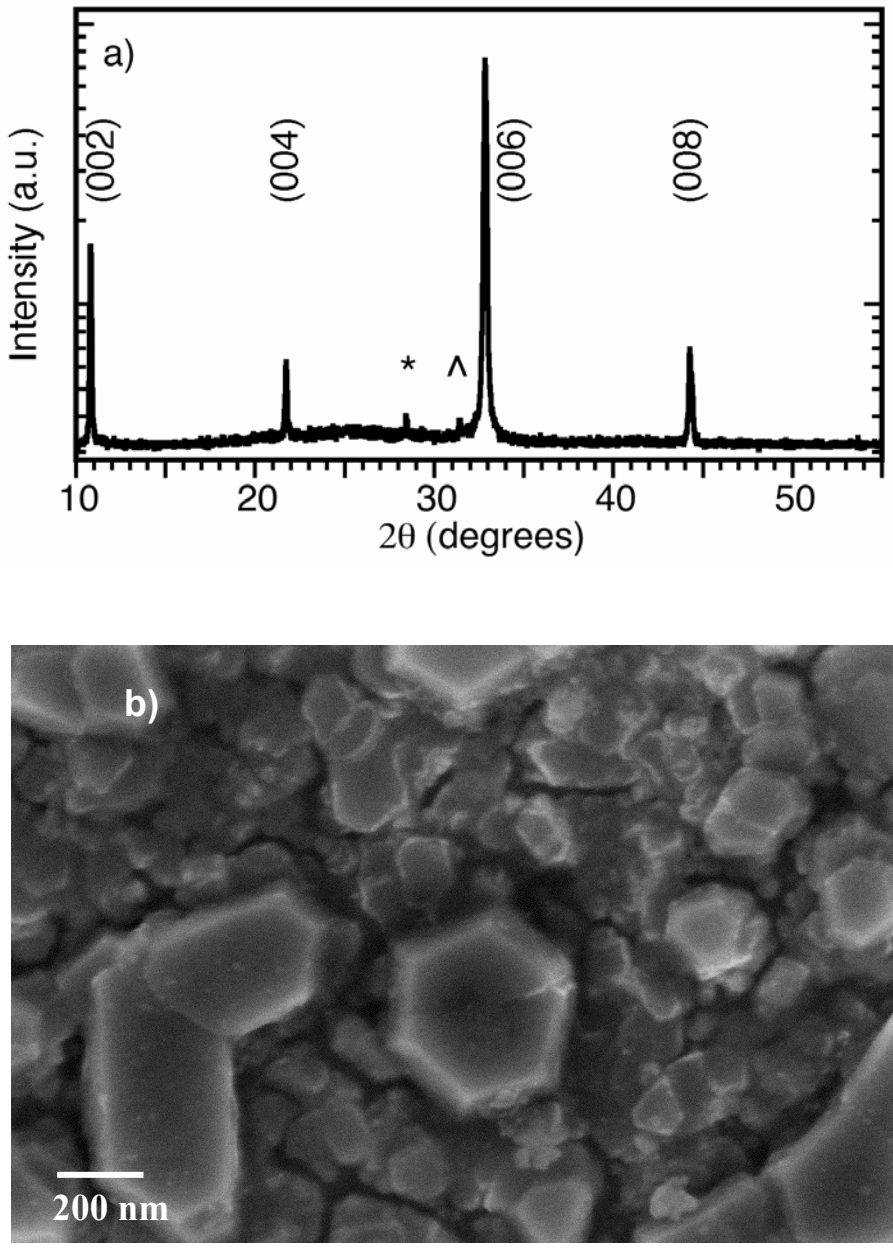

Figure 3.4. a) XRD pattern of 240˚C annealed thin film in H_2S (g) matches the 00*l* reflections of CuS; a Si reference peak is marked with * and the W L_α source peak is marked by ^. b) SEM images of the film surface show hexagonal crystallites consistent with CuS structure.

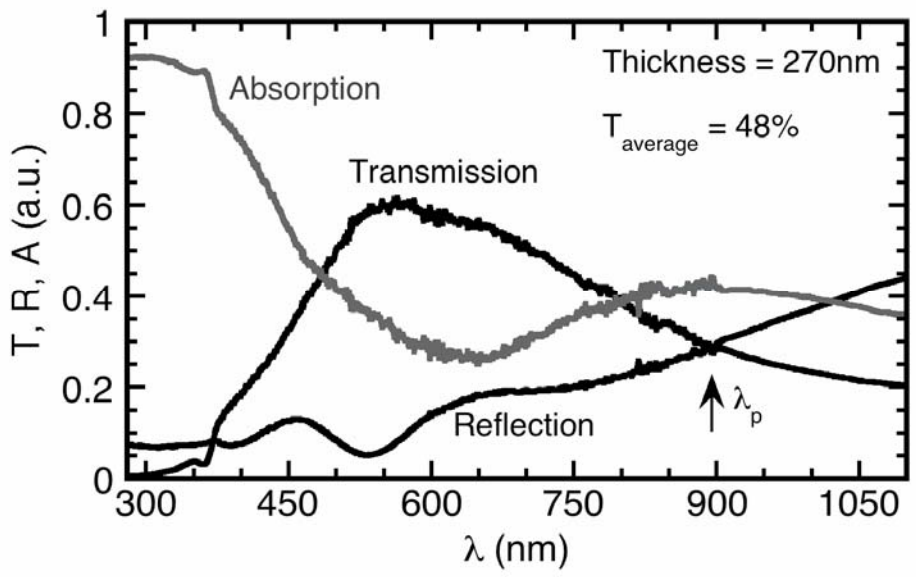

Figure 3.5. Optical transmission and reflection of $Ba_{1-x}K_xCuSF$ (x=0.025) film annealed at 240˚C with CuS separated out on film surface. The position of λ_p = 900 nm for the film shown.

growth of hexagonal crystallites (Fig. 3.4 b), consistent with the structure of CuS. AFM surface imaging indicates a high >50 nm RMS roughness over a 5 x 5 μm^2 area, due to the perpendicular growth of the crystallites in reference to the substrate. Conductivities of 400-3000 S/cm are obtained for the CuS layers. K-doping, laser fluence and annealing temperature all influence the measured conductivity. A high carrier concentration of 3-6 x 10^{21} cm^{-3} and mobility 1 - 4 cm^2/Vs are obtained by Hall measurements. Seebeck coefficients of less then +10 μV/K are typical for metals. The temperature dependent Seebeck coefficient exhibits a positive slope with increasing temperature, commonly observed for degenerate semiconductors.

CuS is a known *p*-type conductor with an ~ 2.5 eV direct band gap and high conductivity [13], varying with stoichiometry in Cu_xS_y films. Transmission and reflection measurements on the obtained films annealed at 240˚C show optical properties similar to that of CuS. The films appear green due to a maximum in

transmission near 550 nm. The average optical transparency of the highly conductive films is ~48 % between 400 – 800 nm. The high surface roughness causes scattering of the incoming light, hence the low average 10% reflectivity below 600 nm (Fig. 3.5). Film transparency on the long wavelength side is limited by the plasma wavelength near 900 nm. The free carrier Drude model is used to extract hole effective mass [14]:

$$m^* = \frac{Pe^2\lambda_p^2}{4\pi^2\varepsilon_0\varepsilon_\infty c^2} \tag{3.3}$$

where λ_p is the plasma wavelength, P is the hole carrier concentration, $\varepsilon_\infty = n^2$ is the dielectric constant, and e, ε_0, c are the electron charge, dielectric constant of vacuum and speed of light, respectively. The absorption ($A = 1 - T - R$) above the band gap is the highest at the plasma wavelength (shown in Fig. 3.5). Inserting this value (900 nm) into Eq. 3.3, we obtain an effective mass of 0.55 m_0. The electro-optical properties of the CuS thin films strongly depend on the copper stoichiometry as described in Ref. [13], and the wide range of conductivities and plasma wavelengths observed in phase-separated BaCuSF films suggests the formation of CuS and sub-sulfides.

In summary, annealing in H_2S (g) allows the preparation of BaCuSF thin films. The secondary phases present in the films are attributed to the high laser power, used for the deposition of the amorphous films. The conductivity of the undoped polycrystalline BaCuSF films is the highest, 5 x 10^{-3} S/cm, using a 280˚C anneal. High carrier concentration is calculated from thermopower measurements, but the estimated low carrier mobility limits the conductivity. Film conductivity is improved by K-doping in films at low annealing temperatures. Above 280˚C the films are less

conductive. High conductivity CuS forms on the film surface when films are annealed below 240˚C.

3.3.2. BaCuSF by Rapid Thermal Annealing

The Rapid Thermal Annealing (RTA) method of semiconductor crystallization is a well-established process in the semiconductor industry. We apply this simple method to produce crystalline BaCuSF thin films in an inert Ar (g) atmosphere.

Phase purity of the crystallized BaCuSF films is strongly dependent on the laser fluence during the amorphous film deposition. Laser energies of 0.5 and 2 J/cm^2 and 1 mTorr Ar (g) deposition pressure are used to prepare amorphous BaCuSF films. The RTA process produces polycrystalline films at temperatures between 300˚C and 600˚C, with typical XRD patterns shown in Fig. 3.6a. It can be clearly observed that films deposited at the higher fluence of 2 J/cm^2 and crystallized in the RTA process exhibit BaF_2 XRD peaks near 25˚, 42˚ and 48˚, curve (i) in Fig. 3.6a. The BaF_2 impurity is also present in films deposited at the same fluence and annealed below 500˚C (not shown). A peak at $2\theta = 26^\circ$ is indicative of α-phase $BaCu_2S_2$ in the resulting films. Lowering the laser fluence results in lower intensity BaF_2 peaks, which completely disappear when amorphous films are deposited at 0.5 J/cm^2. The crystallization product of the amorphous films deposited at 0.5 J/cm^2 is single-phase BaCuSF, as shown in Fig 3.6a curves (ii) and (iii), after RTA in the 300˚C – 500˚C temperature range. Thus the laser fluence appears to be the key parameter for preparation of phase-pure BaCuSF films. The lower fluence of 0.5 J/cm^2 may produce

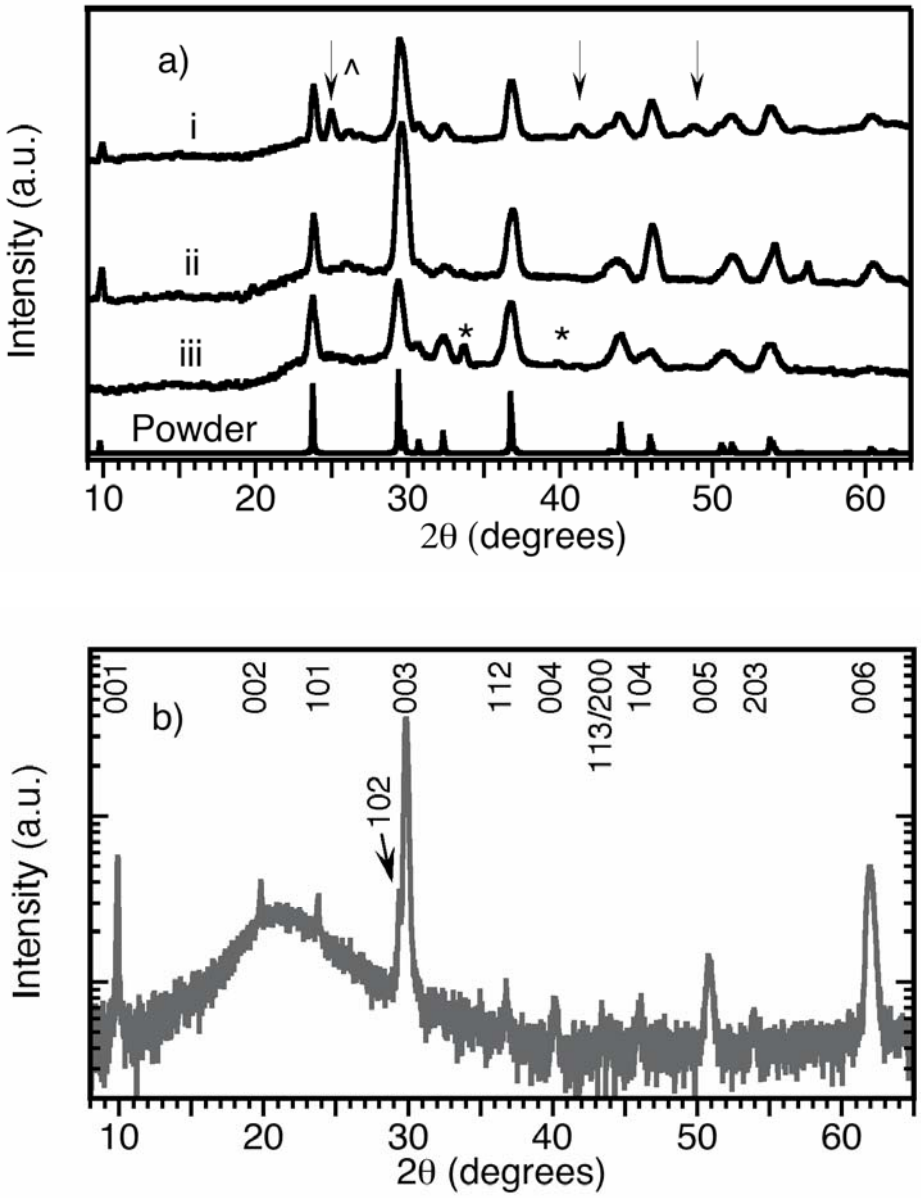

Figure 3.6. a) XRD patterns (glancing incidence) of i) 2 J/cm^2, 500˚C, ii) 0.5 J/cm^2, 500˚C and iii) 0.5 J/cm^2, 300˚C BaCuSF films post-annealed by Ar (g) RTA method. Use of 0.5 J/cm^2 for deposition results in single-phase films. Arrows and ^ indicate peak positions of BaF_2 and α-$BaCu_2S_2$ impurities, respectively. Peaks marked with * are due to In contacts. b) XRD pattern (θ-2θ configuration) of 0.5 J/cm^2 deposited and 500˚C RTA BaCuSF film (same as ii) shows strong *c*-axis orientation. The pattern contains the broad reflection of the SiO_2 substrate.

a highly stoichiometric plume, and/or prevent the loss of Cu–S complexes from the growing film surface due to the lower energy of particles bombarding it. Remarkably, *c*-axis orientation is observed upon 500˚C RTA of this BaCuSF film, Fig. 3.6b. Such texture on amorphous SiO_2 substrates is unusual; generally it is observed only on single crystal substrates, as in the case of BaCuSeF [see Chapter 5] and BaCuTeF [see Chapter 4].

Amorphous films of BaCuSF, and of the BaCuQF (Q = S, Se, Te) in general, deposited at room temperature are unstable when exposed to air with observable clouding of the films on the order of hours. An especially fast degradation within a few minutes to an hour is observed when films are brought in contact with water or high humidity atmosphere. Amorphous BaCuSF films appear to be more stable in lab conditions after a low <300˚C temperature RTA.

Phase separation occurs when annealing temperatures above 600 – 650˚C are used and BaCuSF films become unstable. This is observed in RTA, sealed-tube annealed and H_2S annealed films with appearance of strong $BaCu_2S_2$ and BaF_2 reflections.

As mentioned in section 3.3.1, the as-deposited amorphous films are smooth, typically of RMS roughness below 1 nm (Fig. 3.7a), with ~100 nm particles on the surface – a known problem of the PLD technique. Larger particles can occur on film surfaces, especially near the edges of a 2.5 x 2.5 cm substrate. After annealing at 300˚C – 600˚C, BaCuSF films crystallize and various size grains, on the scale of 10 – 1000 nm, are formed depending on the annealing temperature, shown in Fig. 3.7. Annealing at low temperature, 300˚C, results in a film consisting of small grains on

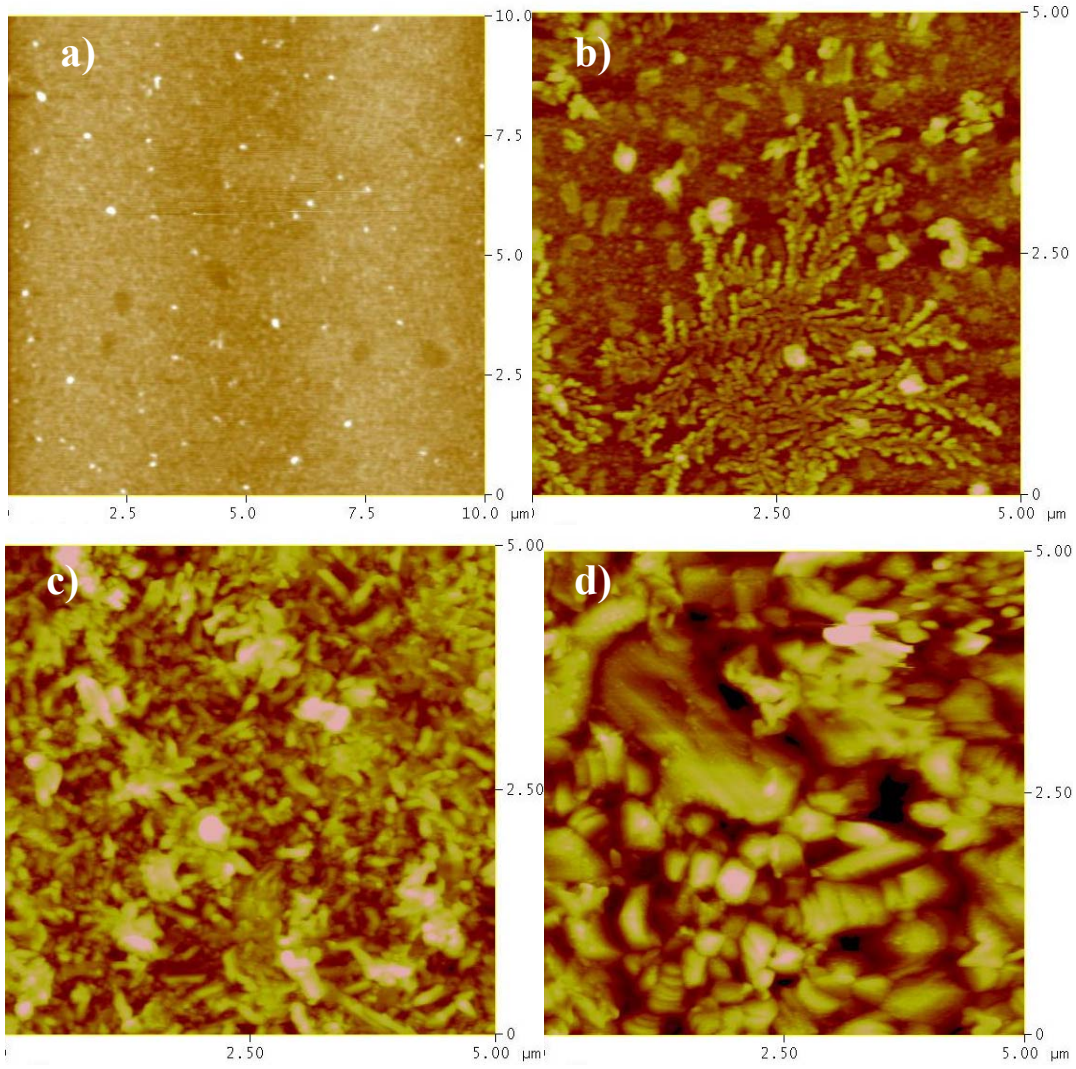

Figure 3.7. AFM surface images of BaCuSF films: (a) amorphous (10 x 10 µm scale) and post-annealed by Ar (g) RTA at (b) 300˚C, (c) 400˚C and (d) 500˚C (5 x 5 µm scale). The grain size increases with higher annealing temperature.

the order of 50 nm (Fig 3.7b). Dendritic growth structure is also noticed. By increasing the annealing temperature to 400˚C, grain sizes increase to ~100 nm in size (Fig 3.7c), and the film surface looks like a bowl of rice. Lastly, 500˚C annealing produces large grains of 500 nm up to few-micrometer-size plates (Fig. 3.7d). The various grain sizes can affect the electrical properties of the films, due to scattering of carriers at the grain boundaries. The surfaces of the 400˚C and 500˚C annealed films

also contain larger features of ~2 μm in width and height with an approximate density of 0.03 μm^{-2}, and are usually avoided in AFM scans. Because these particles are not present on the 300˚C film surface, it can be assumed that their growth takes place during the RTA process. The possibility of composition variation between these particles and the surrounding film has not been studied. The calculated RMS surface roughness increases from 6 to 17 nm with increasing annealing temperature.

Amorphous, as-deposited BaCuSF films are insulating. The crystallization induces carriers, due to slight off-stoichiometry defects in a film such as Cu deficiency. The measured conductivities of the 300˚C, 400˚C and 500˚C RTA films are 8 x 10^{-3} S/cm, 4 x 10^{-2} S/cm and 0.2 S/cm respectively. As before, measurements of the Hall coefficient do not yield reliable results, thus Hall carrier concentrations and mobility data are not available. This suggest mobility values less than 0.1 cm^2/Vs even in the strongly *c*-axis oriented BaCuSF film. Seebeck coefficient measurement yields positive values indicating hole majority carriers. The measured +280 μV/K for 300˚C, and around +90 μV/K for higher temperature annealed films result in calculated carrier concentrations of 3 x 10^{20} and ~10^{21} cm^{-3}, respectively, employing Eq. 3.1. The carrier concentrations in the 400˚C and 500˚C prepared films are similar, so the notable increase in film conductivity indicates improving carrier mobility. The improved mobility is expected from the larger crystallite sizes (Fig. 3.7d) causing less carrier scattering on grain boundaries. The high carrier concentration could be a result of the V_{Cu} defect activation at higher temperatures and low V_S in the films deposited at optimal laser fluence. This is opposite to polycrystalline BaCuSF films prepared by H_2S (g) annealing, where the highest conductivity of 5 x 10^{-3} S/cm is achieved at

280˚C and decreases at higher annealing temperatures, probably due to the reducing nature of H_2S (g).

K-doping is an effective method of carrier generation in BaCusF powders and polycrystalline thin films prepared by H_2S (g) annealing. In case of Ar (g) RTA prepared BaCuSF films, the electrical conductivity does not improve in films deposited from $Ba_{1-x}K_xCuS$ (x = 0.025, 0.1) targets. The reason may lie in an already high carrier concentration (3.2 x 10^{21} cm^{-3}) present in the film, such that the effect of the doping is diminished. The K-dopant is found to strongly interact with the SiO_2 substrate at temperatures above 400˚C as also pointed out in the previous section.

BaCuSF films prepared by RTA are highly transparent, with band gaps estimated above 3.2 eV and excitons observed near the absorption edge. Details about excitons are given in the next section. Over 90% total corrected transmission,

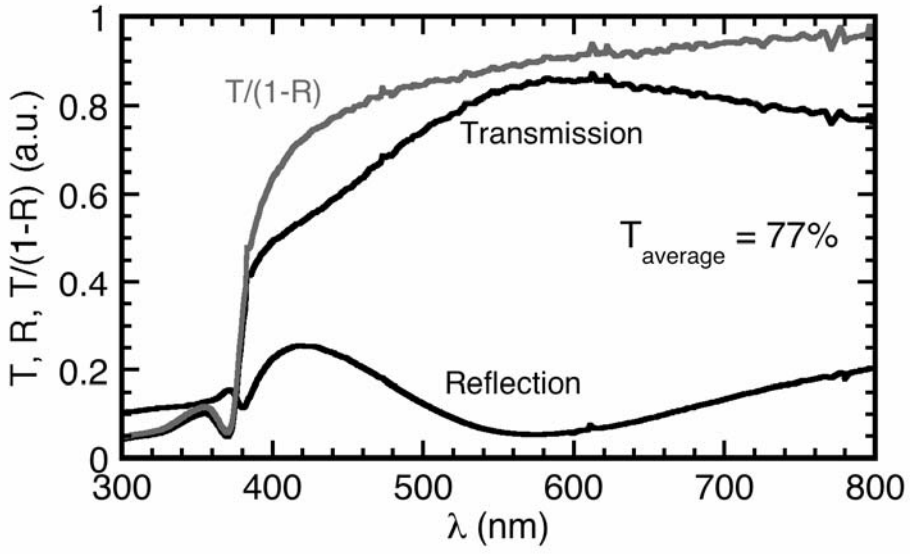

Fig. 3.8. Optical transmission, reflection and T/(1-R) of a 140 nm BaCuSF film annealed at 400˚C by Ar (g) RTA.

calculated as $T/(1-R)$, is present in the 140 nm films, shown in Fig. 3.8. The absorption coefficient (at 520 nm) is near 10000 cm^{-1}, only somewhat higher then for BaCuSF films processed in H_2S (g).

In summary, we have achieved preparation of single-phase BaCuSF thin films by Ar (g) RTA, employing 0.5 J/cm^2 laser fluence for the amorphous film deposition. A maximum conductivity of 0.2 S/cm is observed, over an order of magnitude higher than in H_2S (g) annealed films. High hole-carrier generation is predicted from low Seebeck coefficients at RTA temperatures above 300˚C. The higher conductivity is achieved with minimal loss in transparency of the films in the visible range.

3.3.3. Excitons and photoluminescence of BaCuSF films prepared by sealed tube annealing and RTA processes

In this section the presence of excitons and photoluminescence in BaCuSF films on amorphous SiO_2 substrates is shown. Excitons are bound states of an electron and a hole just below the band gap energy. Red photoluminescence has been reported in BaCuSF films and powders [7]. The emission is believed to arise from the recombination of electrons at S-vacancies and holes on Cu sites.

Amorphous BaCuSF films prepared on SiO_2 substrates by PLD are annealed in evacuated silica tubes at 650˚C. The resulting films are polycrystalline and contain some BaF_2. The second phase is present possibly due to the high laser fluence of 2 J/cm^2 used for deposition, as shown in section 3.3.2. The absorption coefficient and

film thickness are calculated from measured transmission and reflection spectra. The 320 nm thick film has an average 60% transparency in the visible range.

Absorption spectra of BaCuSF films prepared by various post-processing methods are shown in Fig. 3.9. Exciton structure is evident near the band edge. The film obtained by sealed tube annealing (STA) presents 3 absorption peaks at 3.29 eV, 3.38 eV and 3.78 eV at room temperature. Temperature dependent measurements and the observation of similar properties in BaCuSeF, strongly suggest the exciton nature of the absorption features. Lowering the measurement temperature to 80 K, as shown Fig. 3.10, does not sharpen these peaks considerably, as it does for the peaks in BaCuSeF [Chapter 5]. The broadness of peaks is attributed to the polycrystalline nature of the film. In high quality materials exciton peaks become narrower at lower temperatures, due to less thermal smearing. In the present case, the disorder in the

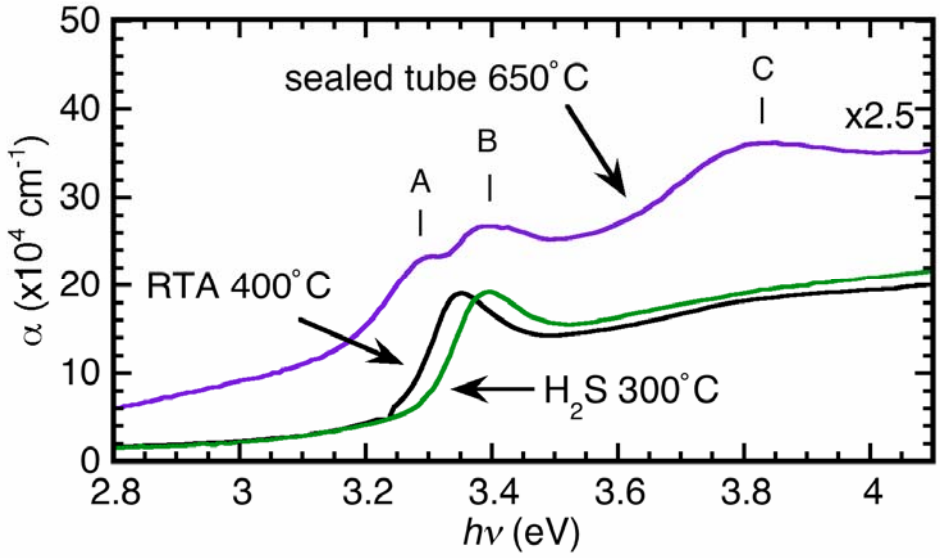

Figure 3.9. Room temperature absorption spectra of BaCuSF thin films exhibiting excitons prepared by various post-processing methods.

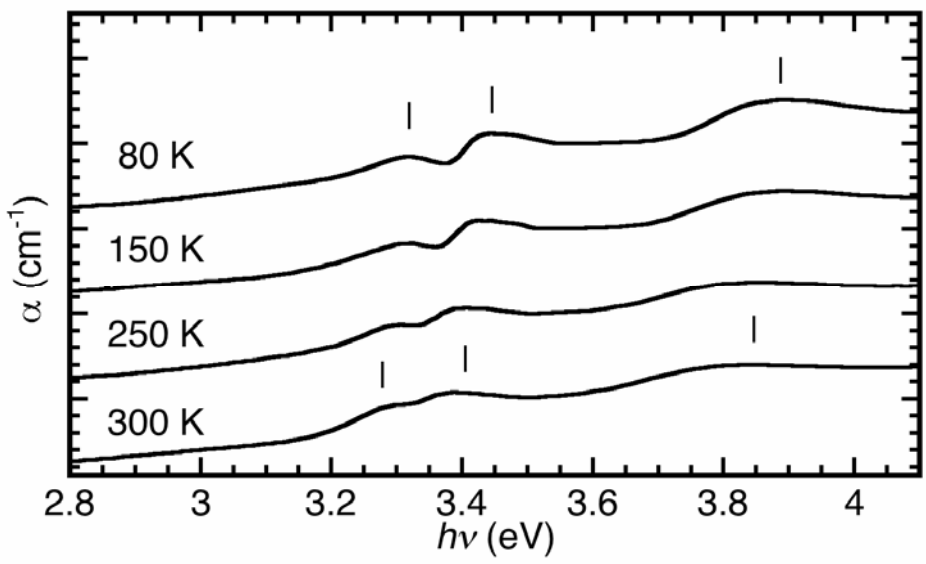

Figure 3.10. Temperature dependence of the excitonic absorption peaks in the 650˚C STA BaCuSF thin film [measured by J. Kinney].

polycrystalline BaCuSF films must dominate the thermal effects to keep the exciton peaks broad even at low temperature. Peak shift towards higher energy with lower temperature is consistent with the temperature dependence of the band gap [15].

Similar exciton structure is observed in thin films of the related material LaCuOS [16]. Following the argument applied to LaCuOS by Hosono *et al*., in Ref. 16, we consider *A* and *B* absorption peaks belong to a series of bound excitons corresponding to transitions from discrete quantum states at the valence band maximum (VBM) to the continuum of conduction band minimum (CBM) states in BaCuSF. The quantum states are composed of Cu 3*d* – S 3*p* orbital contributions, while the CBM is mainly due to Cu 4*s* contribution. Peak *C* is not part of this series due to the large energy separation from the *A* and *B* peaks, whereas the higher energy states should come closer together within a series of excitons. We conclude that this

transition takes place to a higher energy level near the CBM, possibly to a Ba 5*d* or Ba 5*s* – F 1*s* mixed state.

Exciton confinement in the 2 dimensional Cu-S layer can be assumed because of the layered structure of BaCuSF, and the exclusively Cu and S contributions to CBM and VBM. Due to the confinement effects, the energy level spacing of weakly bound, or Wannier, excitons [15] can be modeled as a 2D hydrogen atom [17]:

$$E(n) = E_g - \frac{R^*}{\left(n - 1/2\right)^2},\ n = 1, 2, \ldots \tag{3.4}$$

where E_g is the band gap, and the effective Rydberg constant

$$R^* = \frac{\mu e^4}{2\hbar^2 \left(4\pi\varepsilon_0\right)^2 \varepsilon_r^2} = \left(\frac{\mu}{m_0 \varepsilon_r^2}\right) \times 13.6, \tag{3.5}$$

$$\frac{1}{\mu} = \frac{1}{m_e^*} + \frac{1}{m_h^*} \tag{3.6}$$

where μ is the reduced effective mass of electrons m_e* and holes m_h*, e is electron charge, $\hbar$ is Planck's constant, m_0 is the free electron mass, ε_0 is the permittivity of vacuum, and ε_r is the dielectric constant of the material.

The effective Rydberg constant is the binding energy of the exciton. Assuming that the *A* and *B* peaks belong to the same series with n = 1 and n = 2, solving Eq. 3.4 yields a reasonable binding energy of 36 meV, in agreement with the observation of excitons at room temperature implying $R^* > 25$ meV. The binding energy of BaCuSF excitons is expected to be comparable to that (> 42 meV) of LaCuOS [16] thin films. To unambiguously determine this quantity the sample should be heated to temperatures where the exciton peaks disappear.

Films prepared in H_2S (g) and Ar (g) exhibit only one relatively strong absorption peak (Fig. 3.9) at 3.38 eV and 3.35 eV, respectively, which could be broadened versions of the *A*/*B* peaks seen in the sealed-tube-annealed film. The number of observed peaks and their position strongly depends on the crystalline quality of the resulting films. This is especially the case for weakly bound excitons, where the correlation length between the electron-hole pair is as large as a few lattice constants. Then, BaCuSF films by sealed tube anneal must be of the highest quality (despite the presence of the BaF_2 second phase), showing three excitonic absorption peaks, although high *c*-axis orientation is present in films by RTA. Preparation of higher quality BaCuSF and BaCu(S,Se)F solid solution thin films, possibly by *an in-situ* deposition, is needed to better understanding of excitons in BaCuQF.

Photoluminescence in the visible range is observed in BaCuSF films annealed by the RTA and STA methods, when exposed to UV radiation. The excitation and emission spectra of BaCuSF films prepared with various post-deposition treatments are shown in Fig. 3.11. Films annealed in sealed tube exhibit red luminescence, with peak intensity at 625 nm. A luminescence shoulder extends into the green wavelength range. The position of the red emission agrees well with the previously reported BaCuSF powder and textured film spectra [7], but the broad shoulder was not observed, possibly due to the higher film quality on MgO substrate in the earlier report. It is believed that the emission mechanism of the red (625 nm) photons is due to an electron decaying from a V_S to a hole-defect (another state in the gap, possibly V_{Cu}). The proposed diagram of light emission involving mid-gap S- and Cu-vacancy states is shown in Fig. 3.12.

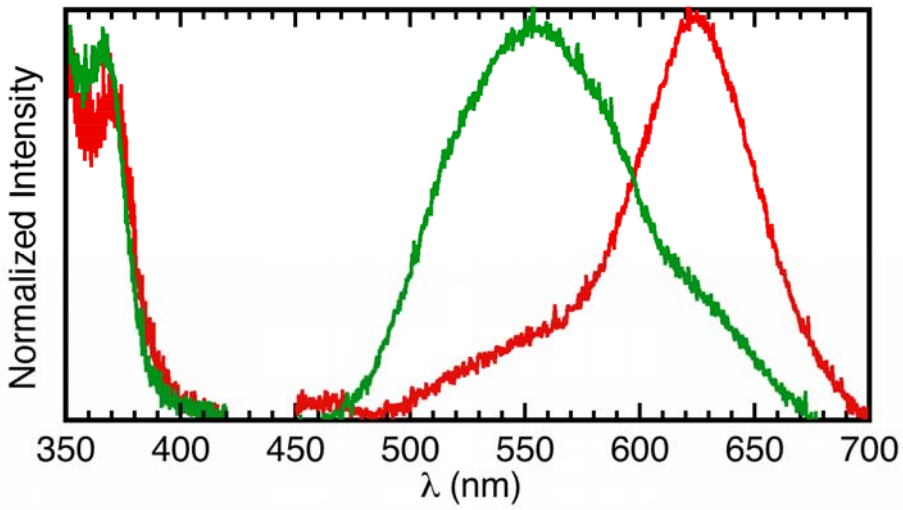

Figure 3.11. Photoluminescence and excitation spectra of BaCuSF films annealed at 400˚C RTA (emission maximum at 555 nm), and 650˚C STA (emission maximum at 625 nm). Excitation spectra overlap for the two films, indicating similar absorption edge structure. Emission at 625 nm coincides with that of BaCuSF film on MgO substrate also annealed by STA [7]. The luminescence intensities are normalized to 1.

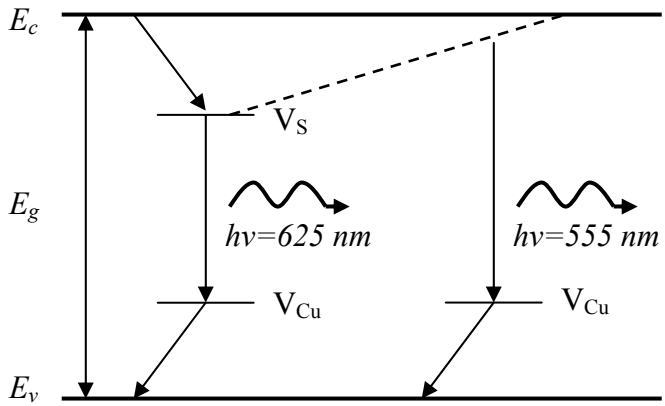

Figure 3.12. Schematic diagram of emission in BaCuSF due to S-vacancy (V_S) and Cu-vacancy (V_{Cu}) gap-states. The dashed line represents the possible change of the donor level V_S energy.

BaCuSF films prepared by 400 – 500˚C Ar (g) RTA show an emission maximum near 555 nm, corresponding to green photons, and a shoulder tailing into the red portion of the spectrum. BaCuSF films with green emission have not been prepared before. The agreement in relative positions of the emission maxima and shoulders indicates that there are two radiative decay processes in polycrystalline BaCuSF that can be selectively controlled by *ex-situ* processing. The overlapping excitation spectra of BaCuSF films with 555 nm and 625 nm luminescence indicate the same absorption mechanism of UV photons. Thus, the origin of the green luminescence may be connected with a high stoichiometry and phase purity achieved in the film deposited at 0.5 J/cm^2 fluence. It is believed that the number of V_S is suppressed and the luminescence takes place from a higher energy level, possibly from the bottom of the conduction band, as also shown in Fig. 3.12. A similar change in photoluminescence color is produced when substitution of Cu by Ag takes place in BaCuSF [18]. No excitonic emission is observed in BaCuSF films, possibly due to non-radiative relaxation of electron-hole pairs to deeper gap-states.

In summary, excitonic absorption is observed in polycrystalline BaCuSF films regardless of annealing method used in preparation, but the absorption is sharpest for STA films. Only films prepared by sealed tube annealing at 650˚C and Ar (g) RTA at 400 – 500˚C exhibit red and green light emission, respectively. The green light emission is shown for the first time. Currently, the value of the exciton binding energy in BaCuSF is unknown, but its observation at room temperature implies an energy over 25 meV. High binding energy is essential for solid-state light emission.

3.3.4. Device application

BaCuSF films prepared by the H_2S (g) annealing method in the 400 – 650˚C temperature range are highly transparent, low conductivity *p*-type semiconductors, which are necessary qualities for transparent thin film transistor (TTFT) application. Such TTFT devices with electron majority carriers have successfully been fabricated [19]. An inverted staggered TTFT structure is used in an attempt to build a device depicted in Fig. 3.13(a). A 5 - 50 nm thick BaCuSF channel layer is deposited by PLD at room temperature onto a pre-manufactured Corning 1737 glass substrate/ITO/ATO stack (supplied by Planar Systems), where ITO is the gate and ATO (AlO_x+TiO_x superlattice) is the gate insulator. Next, H_2S (g) annealing at 500 –

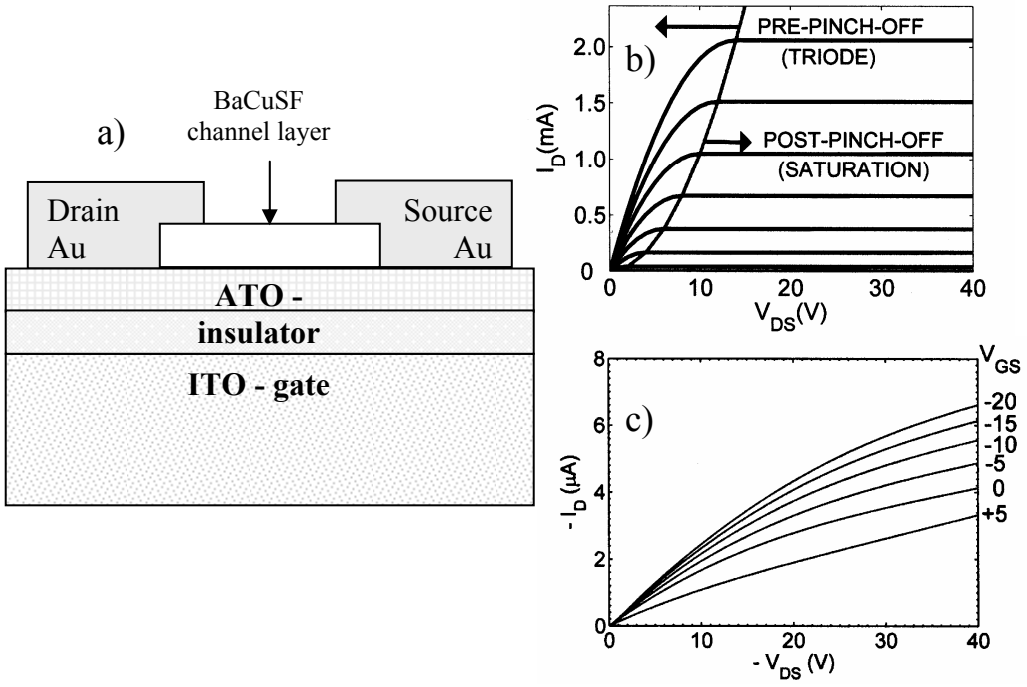

Fig. 3.13. a) Schematic device structure of the proposed transparent transistor. b) Ideal transistor behavior (*n*-type). c) Best result TTFT using BaCuSF channel.

650˚C takes place. The device is then completed with source/drain gold electrodes by thermal evaporation. The fabricated devices of various channel thickness and anneal temperatures do not exhibit transistor-like behavior, although gate-modulated resistance has been observed, as shown in Fig. 3.13c. No hard saturation and turn-off voltages are present in TTFTs using a BaCuSF channel, presumably due to low carrier mobility and high carrier concentration. For more details on BaCuSF TTFTs and their modeling, the reader is referred to Matthew Spiegelberg's MS thesis [20].

High carrier concentrations are estimated from Seebeck coefficient measurements in BaCuSF films prepared by H_2S (g) anneal and Ar (g) RTA, as shown in sections 3.3.1 and 3.3.2. An 8 x 10^{19} cm^{-3} carrier concentration is calculated for the 400˚C H_2S (g) annealed film, and possibly further decreasing with higher annealing temperature. Modeling of the gate-modulated-resistor behavior of a BaCuSF channel layer prepared at 650˚C in H_2S (g) results in a carrier concentration of ~10^{19} cm^{-3}, when a 0.01 cm^2/Vs hole mobility is assumed. This high carrier concentration inhibits turn-off and saturation of the transistor. It is possible that the higher annealing temperatures (> 400˚C) do not significantly decrease the carrier concentration, in spite of the reducing properties of H_2S (g). Donor doping of BaCuSF, e.g. substitution of Zn on Cu sites, or reducing the Cu deficiency in the films should result in the reduction of the carrier concentration. Although the lower carrier concentration would ultimately lead to better transistor behavior, the low carrier mobility could result in small saturation currents through the channel. Thus, alternate materials with high hole mobility should be sought for the realization of p-TTFT, such as BaCuTeF.

3.4. Conclusions

Amorphous BaCuSF thin films are prepared by PLD and crystallized by various post-deposition annealing methods. The effect of laser fluence during deposition of the amorphous BaCuSF films impacts the quality of the crystallized films. The optimal laser fluence is 0.5 J/cm^2 for deposition of amorphous, yielding single phase polycrystalline BaCuSF films following an Ar (g) RTA post-annealing process. Conductive films of 5 x 10^{-3} S/cm and 0.2 S/cm are obtained when post-annealing takes place by flowing H_2S (g) and Ar (g) RTA methods, respectively. Based on Seebeck coefficient measurements the presence of a high carrier concentration (up to 10^{21} cm^{-3}) is probable in the films, and the conductivity is restricted by the low carrier mobility. These factors are responsible for the application failure of BaCuSF channel layers as transparent transistors.

Polycrystalline BaCuSF films exhibit room temperature exciton absorption. Red and green photoluminescence emission is observed, believed to result from electron-hole pair recombination between mid-gap states.

References

1. R. Kykyneshi, B. C. Nielsen, J. Tate, J. Li, A. W. Sleight. J. Appl. Phys. 96 (2004) 6188
2. H. Yanagi, S. Park, A. D. Draeseke, D. A. Keszler, and J. Tate, Sol. St. Chem. 175 (2003) 34
3. K. Ueda, S. Inoue, S. Hirose, H. Kawazoe, and H. Hosono, Appl. Phys. Lett. 77 (2000) 2701

4. H. Hiramatsu, K. Ueda, H. Ohta, M. Hirano, T. Kamiya, H. Hosono, Thin Solid Films 445 (2003) 304
5. H. Yanagi, J. Tate, S. Park, C.-H. Park and D. A. Keszler, Appl. Phys. Lett. 82 (2003) 2814
6. R. Kykyneshi, D. H. McIntyre, J. Tate, C.-H. Park, D. A. Keszler, J. Solid State Sci. (2007) in print
7. C.-H. Park, D. A. Keszler, H. Yanagi, J. Tate. Thin Solid Films 445 (2003) 288
8. H. Hiramatsu, H. Ohta, T. Suzuki, C. Honjo, Y. Ikuhara, K. Ueda, T. Kamiya, M. Hirano, and H. Hosno, Crystal Growth and Design 4 (2004) 301
9. Pulsed Laser Deposition of Thin Films, edited by D. B. Chrisey and G. K. Graham, John Wiley and Sons,New York, Chichester, Brisbane, Toronto, Singapore (1994)
10. H. L. Tuller and A. S. Nowick, J. Phys. Chem. Solids 38 (1977) 859
11. H. Yanagi, T. Hase, S. Ibuki, K. Ueda, H. Hosono. Appl. Phys. Lett. 78 (2001) 1583
12. J. Tate, M.K. Jayaraj, A. D. Draeseke, T. Ulbrich, A. W. Sleight, K. A. Vanaja, R. Nagarajan, J. F. Wager, R. L. Hoffman. Thin Solid Films 411 (2002) 119
13. I. Grozdanov and M. Najdoski. J. Solid State Chem. 114 (1995) 469
14. C. R. Pidgeon, Handbook on semiconductors, North Holland, Amsterdam 1980 vol.2, p.231
15. P. Yu and M. Cardona. Fundamentals of Semiconductors, 3rd edition. Springer Berlin, Heidelberg, New York, 2005
16. K. Ueda, H. Hiramatsu, H. Ohta, M. Hirano, T. Kamiya, and H. Hosono, Phys. Rev. B 69 (2004) 155305
17. X. L. Yang, S. H. Guo, F. T. Chan, K. W. Wong, and W. Y. Ching. Phys. Rev. A 43 (1991) 1186
18. C.-H. Park PhD thesis, Oregon State University, 2005, Call# LD4330 2005D .P37
19. R. L. Hoffman, B. J. Norris and J. F. Wager. Appl. Phys. Lett. 82 (2003) 733
20. M. C. Spiegelberg MS thesis, Oregon State University, 2006, Call #LD4330 2006 .S66

Chapter 4. Electrical and optical properties of conductive bulk and epitaxial thin films of BaCuTeF deposited by pulsed laser deposition

R. Kykyneshi, D. H. McIntyre, J. Tate

Department of Physics, Oregon State University, Corvallis, OR 97331

A. Yokochi

Department of Chemical Engineering, Oregon State University, Corvallis OR 97331

C.-H. Park, D. A. Keszler

Department of Chemistry, Oregon State University, Corvallis, OR 97331

Parts of this work on BaCuTeF powders are published in J. Solid State Chem. 180 (2007) 1672, and on BaCuTeF thin films in press at Solid State Sciences (2007).

4.1. Introduction

BaCuTeF [1] belongs to a family of *p*-type semiconductors BaCuQF (Q = S, Se, Te) with band gaps of 3.1, 2.9, and 2.3 eV, respectively, in powder form [1,2]. The Q = S, Se members have been more widely studied. K-doped pressed pellets of BaCuSF and BaCuSeF exhibit *p*-type conductivity of order 100 S/cm [3], providing a potential to produce high conductivity *p*-type films that are transparent in much of the visible and near infrared range. High quality transparent and insulating thin films of BaCuSF have been made via an *ex-situ* process involving a sealed-tube anneal at 650˚C, also exhibiting red luminescence [2]. Conducting films have proven more

difficult to prepare, because of loss of the K-dopant during the sealed-tube anneal. Although we can produce conducting films (10^{-2} S/cm) via a flowing H_2S (g) anneal of undoped BaCuSF, the average visible transparency is about 68%.

BaCuQF, all members of the P4/nmm space group, are isostructural to LaCuOQ, a related family of *p*-type materials. Thin films of each member of the LaCuOQ family as well as selected solid solutions have been produced; heteroepitaxy has been reported in all, with the notable exception of LaCuOTe. The epitaxial films were produced by a reactive solid-phase reaction method that requires an *ex-situ* sealed-tube anneal for 24 h at 1000˚C [4,5,6].

In this chapter, we demonstrate the bulk and single-phase thin film properties of BaCuTeF, that can be produced *in-situ* by pulsed laser deposition (PLD) at temperatures as low as 250˚C with heteroepitaxial growth above 500˚C on single crystal MgO (100). Native dopants induce *p*-type conductivity in the as-deposited films, and mobilities of order 4 - 8 cm^2/Vs are similar to those of epitaxial thin films of the related chalcogenide LaCuOSe [5], and much higher than the 0.2 cm^2/Vs reported for $LaCuOSe_{0.6}Te_{0.4}$ [6]. Further, BaCuTeF films exhibit a larger band gap than would be expected from the diffuse reflection measurements of the bulk powder. The films may therefore be useful as components of transparent electronic and optoelectronic devices, which are at present exclusively based on *n*-type transparent semiconductors [7]. Incorporation of BaCuTeF as p^+-contact into photovoltaic cells is proposed.

4.2. Experiment

Reagents for synthesis of BaCuTeF were BaTe (synthetic details given below), Cu_2Te (Cerac, 99.5%), and BaF_2 (Cerac, 99.9%). The constituent materials were intimately mixed in stoichiometric proportions and heated in an evacuated silica tube at 500˚C for 12 h. Product characterization by powder X-ray diffraction analysis revealed a mixture of the desired phase and BaF_2. The sample was subsequently annealed with a 5 wt% excess of Te (Alfa, 99.9%) at 500˚C under flowing H_2(5%)/N_2(95%).

BaTe was prepared by using Ba metal (Alfa, 99.2% in oil) and Te. After carefully washing the Ba several times with *n*-hexane, while preventing exposure to air, it was introduced into an Ar-filled glove box. The white oxide surface on the metal was removed with a scalpel, and the resulting material was placed in a silica tube with a stoichiometric amount of Te. The silica tube was evacuated, sealed, and heated at 575˚C for 5h. The powder X-ray diffraction pattern of the product matched that reported for BaTe [JCPDS # 39-1475].

The target is made from BaCuTeF powder produced by the synthesis procedure described above, and pressed into a 3.2-cm-diameter disk at 1.6 tons. The pressed pellet is placed between two graphite plates, heated at 250 ˚C/h to 835˚C, and annealed for 150 min in flowing Ar. The disk shrinks to a diameter of 2.6 cm, and the final target is 92% of theoretical density. The target is polished, pre-ablated prior to each deposition by PLD, and placed 7.5 cm from the substrate during UHV depositions or 6.25 cm for depositions in the presence of Ar(g) (99.999%) gas. The

substrate is just within the laser plume. Fused SiO_2 or single-crystal MgO (100) are used as substrates. The films are deposited at a rate of approximately 6 – 8 nm/min to total thicknesses of approximately 130 - 330 nm and then cooled to room temperature at 10˚C/min.

4.3. Results and Discussion

4.3.1. Bulk properties

BaCuTeF powder is synthesized for the first time. The tetragonal crystal structure belongs to the P4/nmm, and the unit cell contains $Z = 2$ chemical formula units of BaCuTeF. The lattice parameters are $a = 4.4297(1)$ Å and $c = 9.3706(1)$ Å.

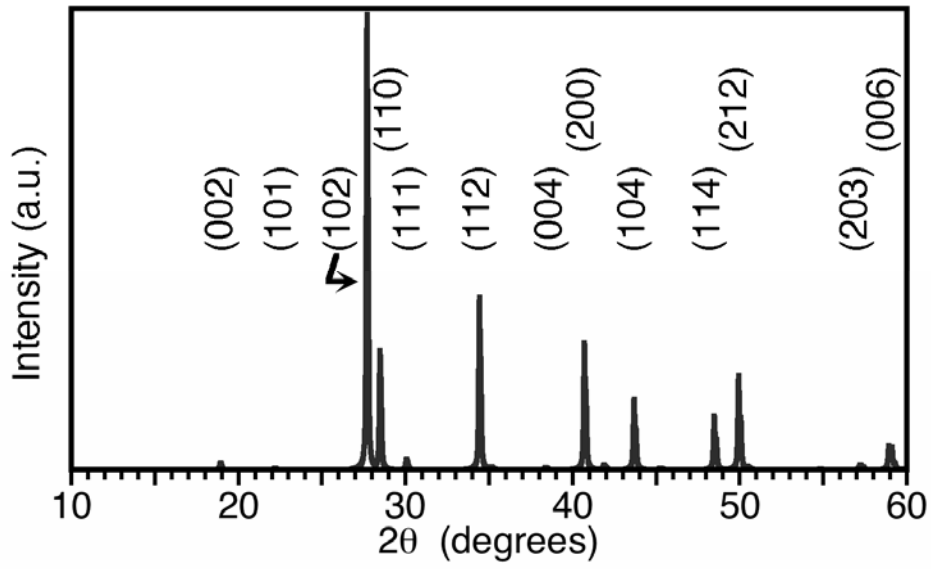

Figure 4.1. BaCuTeF reference XRD pattern [calculated by C.-H. Park].

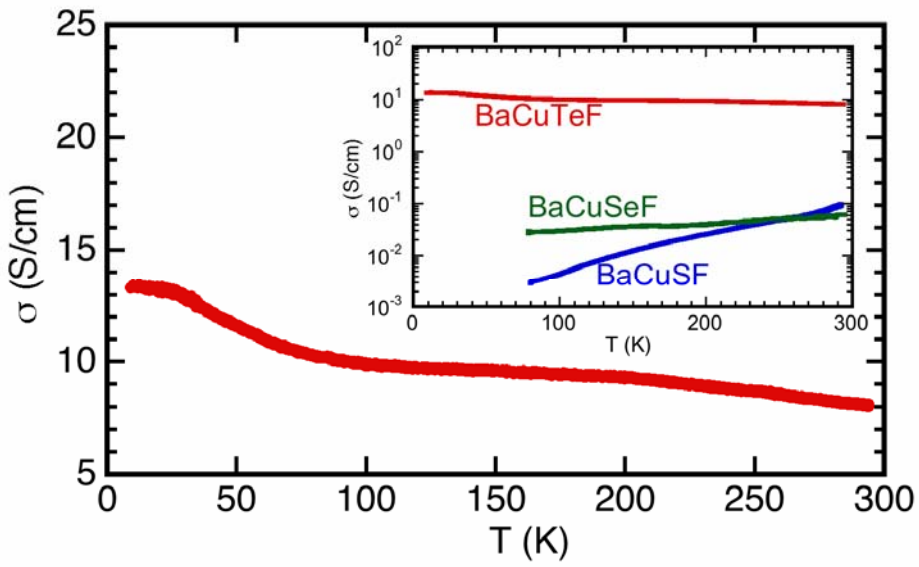

Figure 4.2. Temperature dependence of BaCuTeF pressed pellet. Inset: comparison of BaCuQF (Q = S, Se, Te) powder conductivities.

Details on structural properties and their determination are reported [1]. The calculated XRD reflection pattern from the refined parameters is shown in Fig. 4.1, where the main observable reflections are indexed.

Diffuse-reflectance measurements on BaCuTeF yield a band gap of 2.3 eV, much lower then the desired 3.1 eV for transparent conductors. It is shown in the following sections that thin films of BaCuTeF exhibit a higher ~3 eV band gap. BaCuTeF pressed pellets measure a room temperature conductivity of about 8 S/cm. The conductivity is found to decrease with temperature as shown in Fig. 4.2, indicating metallic behavior. On the contrary, activated behavior is observed in BaCuSF and BaCuSeF, inset Fig. 4.2, with a two orders of magnitude lower room temperature conductivity of ~0.09 S/cm. A similar trend is observed in the orthorhombic $BaCu_2Q_2$ (Q = S, Se, Te) materials [8,9].

Seebeck coefficient measurements on BaCuTeF pellets yield values of +25 to +55 μV/K at room temperature. The coefficient decreases linearly as the temperature is lowered, a characteristic of degenerate semiconductors, also observed in conductivity measurements. Below 100 K the thermovoltage measured against Cu blocks could not be resolved. The high carrier concentration is a result of unintentional doping, likely due to a high Cu-vacancy concentration. Stronger mixing of Cu 3*d* and Te 5*p* orbitals promotes hole carrier formation and may lead to higher mobilities in the thin film form, compared to BaCuSeF and BaCuSF. Thus, the electrical properties of BaCuTeF powders are promising for achieving high *p*-type conductivity thin films and realizing materials complementary to n-type TCO's.

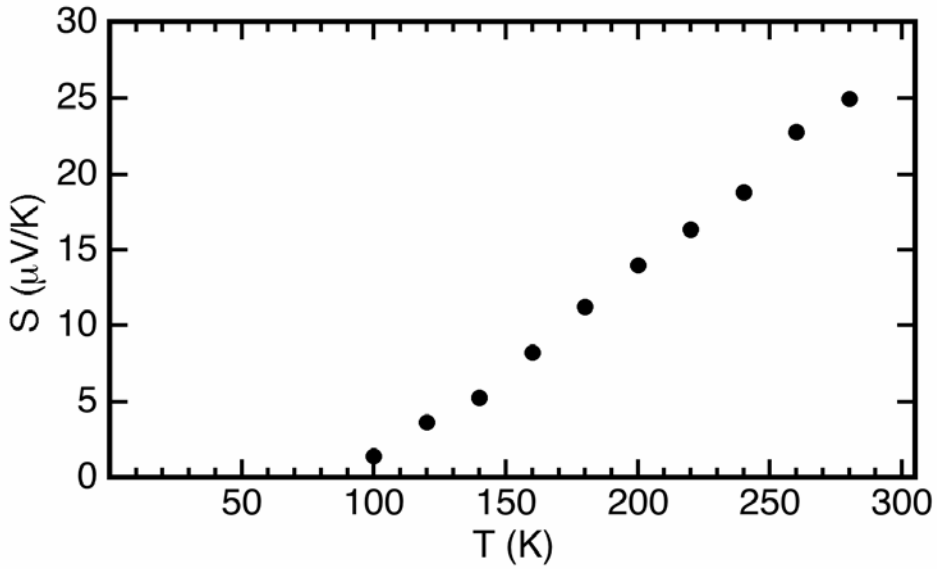

Figure 4.3. The positive Seebeck coefficient decreases with decreasing measurement temperature and vanishes below 100 K.

4.3.2. Epitaxial films

BaCuTeF films are deposited on MgO (100) substrates in the temperature range between 350˚C and 650˚C at 50˚C intervals. MgO provides a reasonable template for epitaxial growth of BaCuTeF films, since it is cubic and its lattice parameter of 4.213 Å is only 5% smaller than the *a*-lattice parameter of tetragonal BaCuTeF. All films deposited on MgO in UHV exhibit significant preferred *c*-axis orientation. Films deposited in the temperature window of 500 to 600˚C exhibit only (00*l*) X-ray reflections. Deposition at 650˚C and below 500˚C, however, leads to the appearance of a small (102) peak in otherwise strongly *c*-axis oriented films, while at 350˚C, the preferred orientation diminishes significantly. For UHV deposition, the strongest texture and narrowest rocking curve (1.65˚ for the (003) peak) are achieved for films deposited on substrates at 600˚C. Relative to UHV compounds, films deposited at 600˚C in Ar at 50 μTorr and 1 mTorr exhibit more intense and narrower diffraction profiles. The moderation of the kinetic energy of the impinging species by the Ar gas may be sufficient to prevent film damage but not so severe as to cause low surface mobility during growth. The best result is seen in Fig. 4.4 for a film deposited at 600˚C and 1 mTorr Ar. Only the (00*l*) reflections are observable, well aligned with the MgO substrate (200) peak. From the BaCuTeF (00*l*) positions we find a *c*-lattice parameter of 9.335(4) Å, about 0.4% lower than the value of 9.3706(1) Å obtained from a refinement of BaCuTeF powder XRD data [1]. The *a*-lattice parameter calculated from the position of the (102) peak of a film deposited at 650˚C is also slightly smaller than the value from powder refinement. The Williamson-Hall method

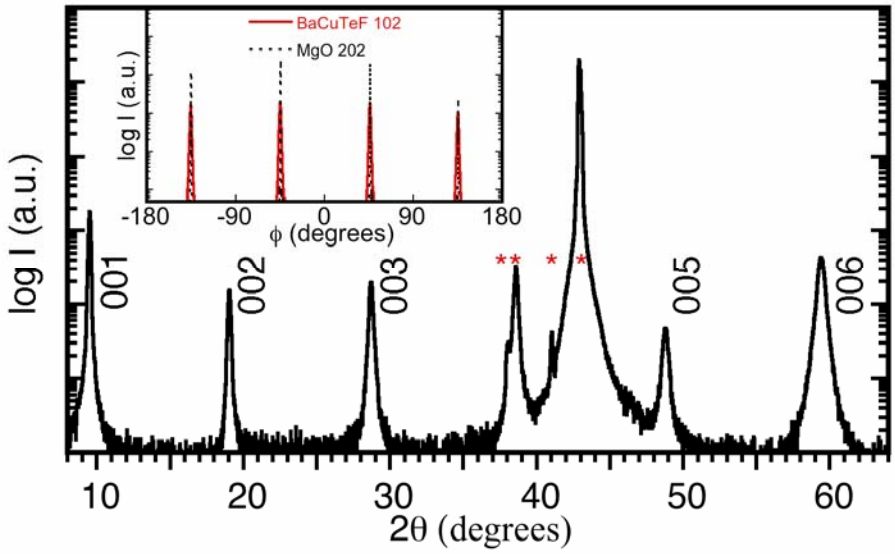

Figure 4.4. XRD pattern of a fully *c*-axis oriented BaCuTeF thin film deposited on single crystal MgO (100) at 600˚C in the presence of 1 mTorr Ar. The BaCuTeF (004) reflection at 39˚ 2θ coincides with MgO (200) reflections, marked by asterisks, from X-ray source lines. Inset: ϕ-scan of BCTF (102) and MgO (202) reflections showing in-plane alignment of the film and substrate.

[10] is used to obtain the film thickness (or grain size if that is smaller) and lattice strain from peak broadening. The film thickness is consistent with 170 nm, the value determined more precisely by optical interference measurements and scanning electron microscopy (SEM). The estimated strain calculated from peak broadening is 0.67%. A Gaussian fit to the rocking curve of the (003) peak yields a FWHM of 1.0˚. This spread of angles in out-of-plane crystallite growth is large compared to LaCuOS epitaxial films [4], but the relatively low temperature process and *in-situ* production of the film are a clear advantage. An increase in the *c* parameter, as well as in lattice strain, is found for the films deposited at lower pressures at the same temperature.

In-plane alignment of the film and substrate is also observed as shown in the inset of Fig. 4.4. The maxima of the (102) peak of the BaCuTeF film and the (202) peak of the single-crystal MgO occur at the same ϕ angles indicating that the *ab*-planes of the film and substrate coincide. Thus BaCuTeF films grow epitaxially on MgO (100) substrates at 600˚C with out-of-plane $(00l)_{BCTF}//(001)_{MgO}$ and in-plane $[100]_{BCTF}//[100]_{MgO}$ alignment. The window for complete epitaxy is 500 to 600˚C, being optimal for deposition in 1 mTorr Ar. The high crystalline quality translates into superior transport properties as described below.

Surface and cross-sectional micrographs of epitaxial films deposited at 600˚C, 1 mTorr Ar on MgO exhibit no evidence of grains, supporting a heteroepitaxial growth mode consistent with the XRD data. Cross-sectional SEM images indicate film thicknesses that are consistent with the optically measured values; the film shown in the lower panel of Fig. 4.5 is 170 nm thick. As indicated in the cross-sectional SEM image in the upper panel of Fig. 4.5, about 1% of the film surface contains submicron-sized particles, but in the areas between these, the film surface is smooth, confirmed by atomic force microscopy images, which indicate a root-mean-square surface roughness of 2.8 nm. The roughness increases to an average of 8 nm for the film deposited in UHV.

Room temperature conductivity and Hall measurements on BaCuTeF films on (100)-oriented MgO are shown in Fig. 4.6a. The conductivity of UHV-deposited films peaks at 88 S/cm for a deposition temperature of 600˚C. Further improvement is observed with the introduction of Ar into the chamber during deposition, with the conductivity reaching 167 S/cm for films deposited at 600˚C in 1 mTorr Ar. The

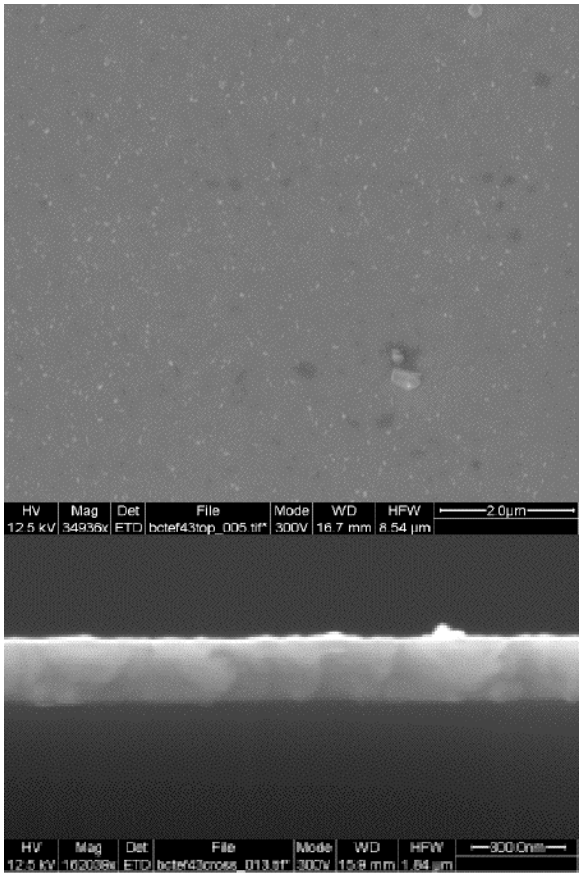

Figure 4.5. SEM images of a fully *c*-axis oriented BaCuTeF thin film deposited on single crystal MgO (100) at 600˚C in the presence of 1 mTorr Ar. The top panel shows a surface image, while the bottom panel is a cross-sectional image.

carrier concentrations in the films are almost constant at 1.0 - 1.3 x 10^{20} cm^{-3}, and it is the carrier mobility improvement of almost a factor of two (from 4 - 8 cm^2/Vs as shown in the inset to Fig. 4.6a that accounts for the higher conductivity. The improved mobility is to be expected from the superior crystal quality of the film deposited in 1 mTorr Ar. Epitaxy not only reduces the number of grain boundaries, but also, in this anisotropic material, ensures that the Cu-Te planes associated with high hole conductivity now line up, providing a much improved conduction pathway, and hence higher mobility. Hall measurements show that the carriers are holes, and

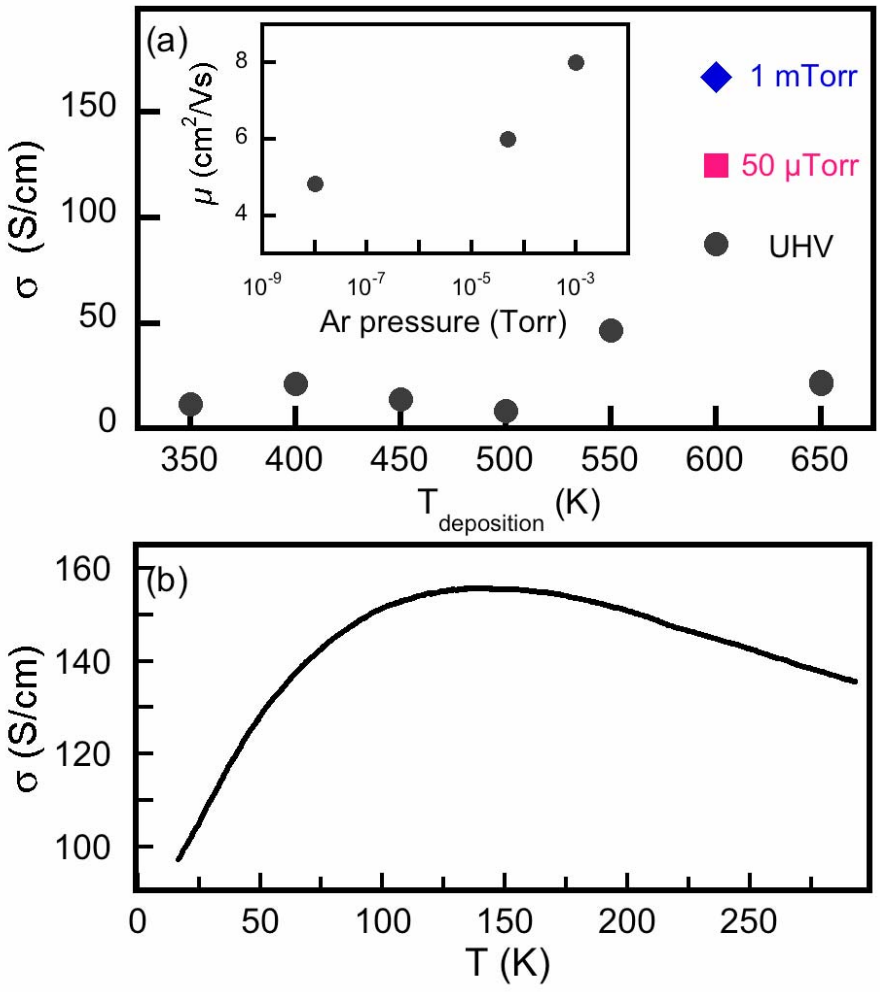

Figure 4.6. (a) Electrical conductivity of BaCuTeF films on (100) MgO substrates at various deposition temperatures. Circles are UHV deposition, square is 50 μTorr, and diamond is 1 mTorr. Inset: Mobility of films deposited at 600˚C at various Ar gas pressures. (b) Temperature-dependent conductivity of the BaCuTeF film deposited at 1 mTorr Ar.

this is confirmed by Seebeck measurements, which yield coefficients near +90 μV/K in the epitaxial films at room temperature. A power factor $P = S^2 \sigma = 1.4 \times 10^{-4}$ $Wm^{-1}K^{-2}$ is calculated for the epitaxial film deposited at 600˚C and 1mTorr Ar, approaching the useful range ($\sim 1 \cdot 10^{-3}$ $Wm^{-1}K^{-2}$) for application in thermoelectric devices.

The temperature-dependent conductivity of the epitaxial film demonstrates competing metallic and activated transport mechanisms (Fig. 4.6b). The conductivity of the film increases from room temperature to 150 K, displaying the weakly metallic behavior that is characteristic of degenerate semiconductors (also shown above in case pressed powders of BaCuTeF). Further cooling to about 16 K produces a decrease in conductivity reminiscent of the activated processes common in non-degenerate semiconductors. Both effects are small; the variation of conductivity is less than a factor of 2 in the measured temperature range. This would be an advantage in applications requiring stable conductivity over a large temperature range.

Care must be taken to protect the films from condensation. They increase in conductivity and decrease in transparency once they absorb water, which is a problem generic to most barium-chalcogenide materials. In ambient conditions, changes from moisture absorption from the air occur on a time scale of months.

The transport measurements show that nominally undoped BaCuTeF is a *p*-type semiconductor. We have no direct evidence to identify the defects that produce conductivity in nominally undoped BaCuTeF, but we speculate that Cu vacancies may be the source. Control of the defects and hence the conductivity in nominally undoped materials is notoriously difficult, but the deposition temperature seems to provide one means to control the conductivity, primarily by changing carrier mobility. BaCuTeF has a relatively large Hall mobility of 8 cm^2/Vs when considered within the framework of *p*-type transparent conductors. For comparison, Cu-based transparent conducting oxides like $CuMO_2$ have mobilities less than 0.5 cm^2/Vs, and other nominally undoped chalcogenide based *p*-type transparent conductors like $BaCu_2S_2$

[11], BaCuSF and LaCuOSe [12] have mobilities similar to, or smaller than BaCuTeF. This is to be expected from the crystal structure where there are direct Te-Cu-Te linkages in the sheets perpendicular to the c-axis, which translates to strong Cu *d* – Te *p* mixing in the valence band. In (undoped) delafossites, there are no O-Cu-O linkages perpendicular to the c-axis.

Optical reflection and transmission data are shown in Fig. 4.7a for an epitaxial film on MgO deposited at 600˚C and 1 mTorr Ar. The inset to Fig. 4.7b shows that the film is transparent with a yellow tinge resulting from slightly higher absorption in the blue region near the band edge. Fitting of the interference fringe positions yields a refractive index of 2.3 - 3 in the visible range, and a film thickness of about 170 nm, in good agreement with the microscopy thickness measurement. The average transmission and average reflection for the film-substrate stack are about 63% and 24% respectively, in the visible range, and these are maintained through the infrared spectrum up to 2.5 μm. Transparency is affected both by reflectivity (which is quite large relative to lower-index materials like SiO_2 or In_2O_3) and by the combination of absorption coefficient and thickness. We calculate a reflection-corrected transmission $T/(1-R) \approx e^{-\alpha d}$ [13] to eliminate the effect of interference fringes and use the film thickness value obtained from the fitting procedure to find the absorption coefficient α. The absorption coefficient changes significantly between 400 and 440 nm, with a smaller, but distinct change near 510 nm. The high-energy feature is the strongest, sharpest and most reproducible feature of the absorption spectrum. Assuming this to be the signature of a direct gap (LDA calculations without spin-orbit coupling [1] indicate a direct gap at the Γ point), we plot $(\alpha E)^2$ against E, where E is the photon

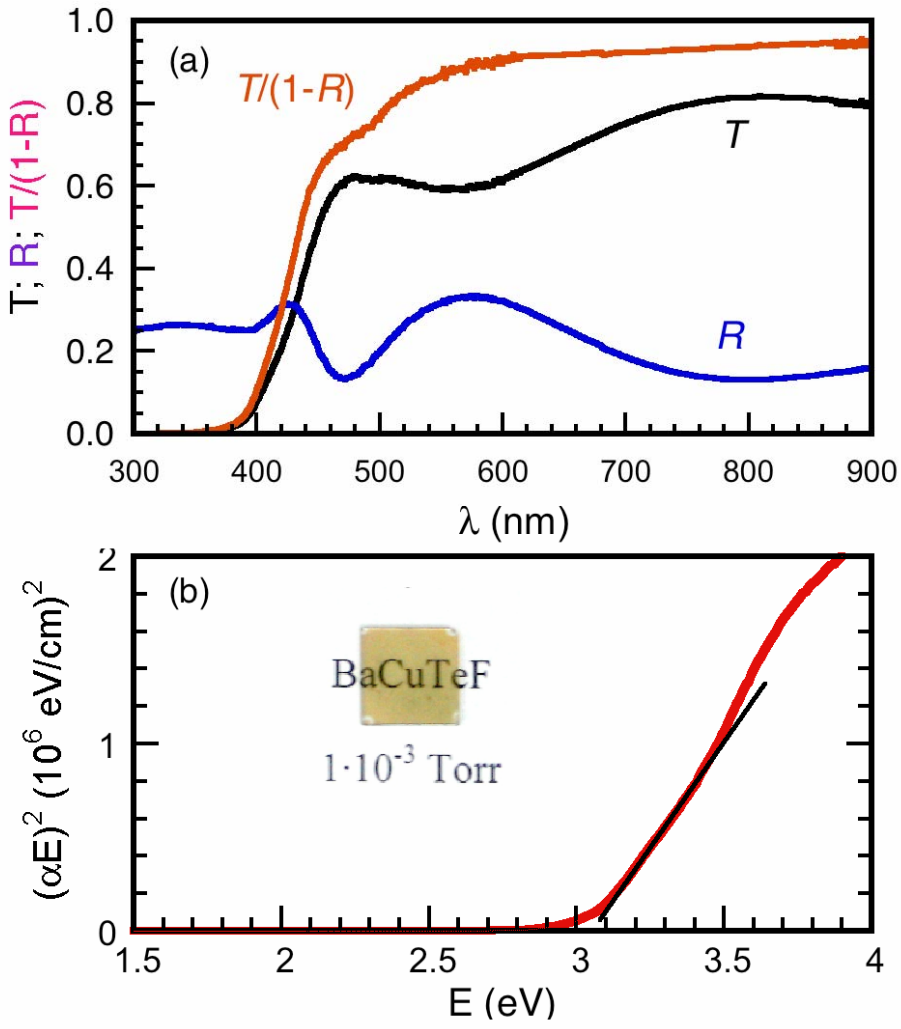

Figure 4.7. Optical characteristics of a 170-nm BaCuTeF film on MgO (100). (a), Transmission T, reflection R, $T/(1\text{-}R) \approx e^{-\alpha d}$. (b) Direct band gap analysis. Inset: photograph of the film.

energy, and obtain the gap from the extrapolation of the straight-line portion of the graph to the energy axis [14]. This procedure, shown in Fig. 4.7b, yields E_g = 3.04 eV for the film shown. The band gap associated with the high energy feature is independent of the film thickness, is reproducible within about 0.1 eV from film to film and within a particular film over a long time. It occurs both in highly oriented and polycrystalline films. The lower energy feature is much weaker (transmission

changes gradually from 90% to 70%), and corresponds roughly to the 2.3 eV energy gap measured in BaCuTeF powders [1]. We hesitate to identify this feature as the true band gap because it is not as reproducible between samples, although it is most distinct in the samples that show the sharpest X-ray diffraction and the strongest orientation. If it is due to an impurity phase, that phase is not discernible in the diffractograms. The feature also occurs in a region of the spectrum where thin film interference is important, though we believe we have properly corrected for this.

The BaCuTeF band gap is only slightly smaller than the band gap of 3.1-3.2 eV measured in BaCuSF films [2], whereas it would be expected to be much smaller based on anion change. (ZnQ and $CuInQ_2$, for example, exhibit decreasing gaps in the direction Q = S $\rightarrow$ Se $\rightarrow$ Te [15]). In this regard, the band gaps of BaCuQF films (Q = S $\rightarrow$ Te) exhibit behavior reminiscent of that of the $CuMO_2$ family where there is a slight *increase* of the band gap as measured by optical absorption with M = Al $\rightarrow$ Ga $\rightarrow$ In. In this case, the explanation for the anomalous behavior is that symmetry considerations suppress the transitions between states separated by the smallest band gap, and that the main optical absorption occurs between states separated by a larger gap [16]. However, in the case of BaCuQF powders (Q = S, Se, Te), band gap data from diffuse reflection appear to follow the expectation of a gap decreasing with increasing anion size [2]. It is not clear why films would behave differently. Powder absorption spectra tend to be much broader than film spectra, and the film spectra should be more representative of the definitive experiments - absorption from well-characterized single crystals. Experiments on well-characterized epitaxial BaCuSeF

films, as well as more refined calculations of optical properties will help to address this issue, as will single crystal studies.

4.3.3. Polycrystalline Films

It is of interest to investigate polycrystalline films, which can be formed at lower temperatures and on amorphous substrates. If their properties are useful, such films are more likely to find commercial application because they are cheaper and easier to make than their high-end epitaxial counterparts. BaCuTeF is a good candidate in this regard, being easier to produce than either BaCuSF or LaCuOTe. Both BaCuTeF and BaCuSF films can be deposited by PLD from a target of the appropriate composition. We find significant loss of S and the appearance of BaF_2 in the XRD patterns when BaCuSF films are deposited above room temperature. Thus BaCuSF films must be deposited at room temperature and the resulting amorphous films annealed *ex-situ* at 650˚C in a sealed tube with excess BaCuSF powder to prevent S loss. In contrast, BaCuTeF begins to form at ~250˚C and withstands deposition temperatures up to 650˚C without second phase formation.

Polycrystalline BaCuTeF films are readily formed *in-situ* during PLD deposition, and useful optical and electrical properties can be obtained. It is somewhat more difficult to reproduce desired properties in polycrystalline films because of a strong effect of the film microstructure on these properties, and the large sensitivity of microstructure to deposition conditions, particularly deposition temperature. Here we describe a series of films deposited at substrate temperatures between 300 and 550˚C on fused SiO_2 substrates. The structural and optical properties fall broadly into two

categories, according to whether film deposition occurs below or above 450˚C, which we refer to as "LT" (low temperature) and "HT" (high temperature) films respectively. Films deposited at room temperature are amorphous according to XRD and they form a separate category.

XRD patterns of BaCuTeF films (Fig. 4.8) show no evidence of a second phase at any deposition temperature. The films are amorphous when deposited between room temperature and 150˚C and polycrystalline at higher deposition temperatures. They remain polycrystalline even when deposited at temperatures that

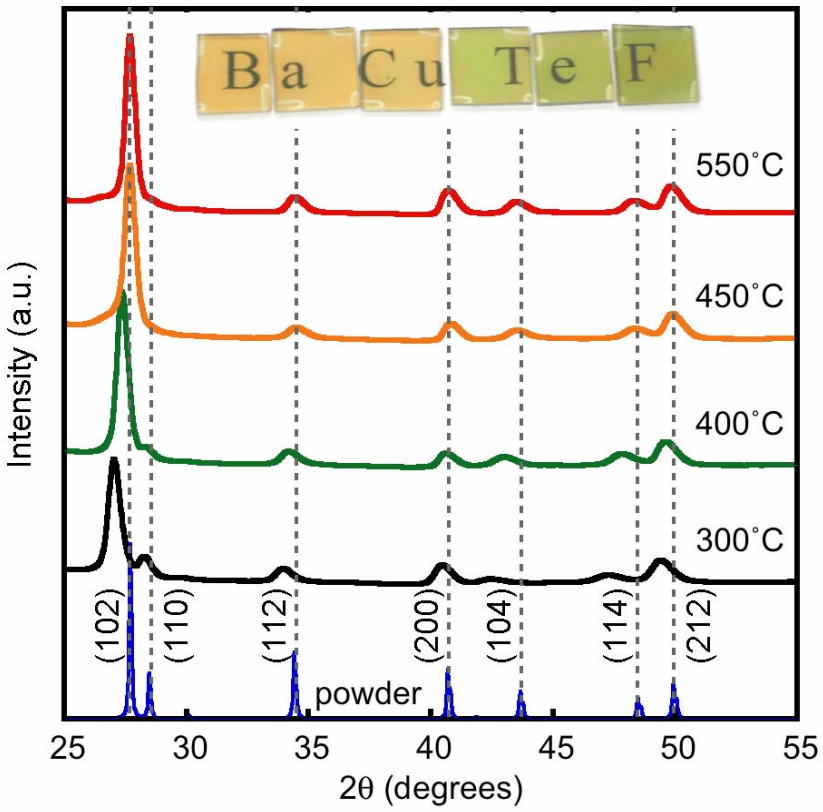

Figure 4.8. X-ray diffraction patterns from polycrystalline BaCuTeF thin films deposited at various temperatures on fused SiO_2 (spectra are offset on the abscissa for clarity). Inset: BaCuTeF films deposited in the 300 - 550˚C range in 50˚C steps.

produce strong texture and heteroepitaxy in films on single-crystal MgO. The polycrystalline nature of the films is evident from the XRD pattern in Fig. 4.8. These diffractograms were calibrated and aligned by using the diffraction peaks from a thin Au dot painted onto the films. (The Au peaks are not shown in Fig. 4.8.) The HT films exhibit XRD peaks that closely match each other and the powder peak positions calculated for tetragonal BaCuTeF. LT films, on the other hand, have peak shifts towards lower 2θ angles. This translates into an increase of the lattice parameters of up to 0.005*a* and 0.044*c* relative to powders for films deposited at 300˚C. This observation is opposite to the epitaxial film results, where a decrease in *a*- and *c*-lattice parameters occurs. Also, the appearance of the (110) peak in LT films indicates higher disorder in grain orientations in the LT films. SEM imaging reveals a decrease of grain size with lower deposition temperature. Grain sizes are about 250 nm for the film deposited at 550˚C, 150 nm at 450˚C, 100 nm at 400˚C, and decrease further at lower deposition temperature.

The polycrystalline films exhibit much lower *p*-type conductivity and mobility than the epitaxial films deposited under identical conditions. Amorphous BaCuTeF films deposited at room temperature are slightly conductive at about 0.5 S/cm. The LT films, rather surprisingly, show the higher values of conductivity, carrier concentration, and mobility (6.6 S/cm, 1.7 x 10^{20} cm^{-3}, and 0.25 cm^2/Vs for the 300˚C film). For the HT films, representative values are 1.1 S/cm, 0.5 x 10^{20} cm^{-3}, and 0.15 cm^2/Vs for the 450˚C deposition. We had expected that the properties of the larger-grained HT films would be more similar to the epitaxial films, but we note that in this and other materials systems, optimal deposition conditions for epitaxial and

polycrystalline films can be quite different, and here we are comparing identical deposition conditions, optimized for epitaxial growth.

HT polycrystalline thin films have similar values of the Seebeck coefficient to the epitaxial films, close to +90 μV/K. An increase to 130 μV/K for films deposited at 300˚C is found for LT films, which is surprising because of the higher conductivity of the LT films. This may be linked to structural changes in the films observed by XRD and SEM.

The optical properties of the polycrystalline BaCuTeF films also exhibit some variations with deposition temperature. The films are all characterized by an average reflectivity of 20% in the range 400-800 nm, very similar to the epitaxial films. The difference in average transparency of 63% for the LT films and 50-55% for the HT films is in part due to thickness differences (290 nm for LT and 330-350 nm for HT), but the absorption coefficients are in fact different at all wavelengths. For example, α is ~8000 cm^{-1} at 520 nm for the LT films, and about a factor of 2 larger for the HT films. We determine band gaps of 3.0 eV for HT films and 3.2 eV for LT films. A photograph of the polycrystalline BaCuTeF films against a white background appears in the inset of Fig. 4.8. The yellow tinge results from blue absorption near the band gap, and the green in the HT films is a result of strong transmission in the green due to interference effects.

The LT BaCuTeF polycrystalline film process may be useful to produce a *p*-type wide band-gap semiconductor for applications in electronics and photovoltaics where transparency in most of the visible range is required and moderate conductivity suffices.

4.3.4. Rapid Thermal Annealing

Solar energy is an abundant resource and can be used for power generation via photovoltaic (PV) conversion. Various types of solar cells have been developed such as *p*-*n*-junction, heterojunction, thin film, *etc* [17]. Recently thin film solar cells have attracted much attention due to high conversion efficiencies achieved in $Cu(In,Ga)(S,Se)_2$ and CdTe [18]. A substantial effort has been made in band engineering at the *n*-contact of the devices, such as inclusion of intrinsic CdS and ZnO buffer layers between the degenerate transparent conductor and the absorber CdTe layers [18]. A notable limitation of such thin film PV cells is the lack of a wide band gap, p-type, degenerate semiconductor for effective hole carrier extraction. BaCuTeF possess all of these properties, and is therefore a suitable candidate for p^+-contact. A simplified cartoon of the proposed photovoltaic cell structure is shown in Fig. 4.9. Such a structure will allow illumination of the cell from both sides, due to the transparency of BaCuTeF in the visible range. The top n^--contact is needed to minimize losses, due to the moderate conductivity of BaCuTeF. Details of a thin film PV cells operation and solar cells in general are beyond the scope of this discussion and the readers are referred to [19] for further information.

Polycrystalline thin films of BaCuTeF can be prepared by an *in-situ* deposition process at elevated temperature as described in the previous section. Films have hole carrier concentrations in excess of 10^{20} cm^{-3}, and together with the high band gap of ~3 eV is a good candidate for Ohmic p-type contact in PV cells.

For added flexibility in preparation methods, amorphous BaCuTeF films are

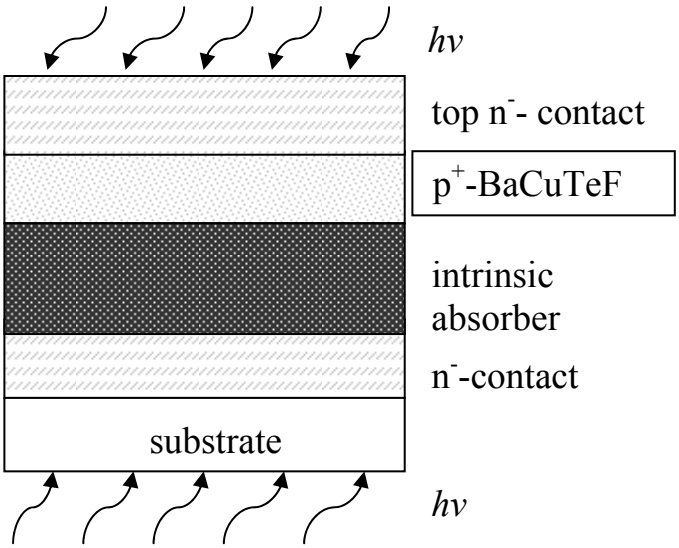

Figure 4.9. A proposed photovoltaic cell structure using BaCuTeF *p*-type contact. The generated electron and hole carriers are extracted from the cell in the respective n^- - and p^+-contacts. The n^--contacts are high conductivity transparent conductors (for example ITO). The details of band engineering are not considered here for simplicity.

deposited at room temperature on a-SiO_2 substrates and post-annealed by rapid thermal annealing (RTA) method in Ar (g). This annealing technique is widely used in industry for semiconductor processing. Typical film thickness is 150 nm of the as deposited and annealed films up to 500˚C. Amorphous films are crystallized at annealing temperatures above 300˚C and phase separated above 500˚C indicated by XRD patterns, and also observable in the electrical and optical properties of the resulting films. The phase separation products are $BaCu_2Te_2$, BaF_2 and various compositions of Cu_xTe_y. Below 300˚C films remain amorphous, but the stability of the films in laboratory conditions seems to increase compared to as prepared films. Precautions must be taken for transportation of as-deposited amorphous BaCuTeF films, especially in high humidity conditions.

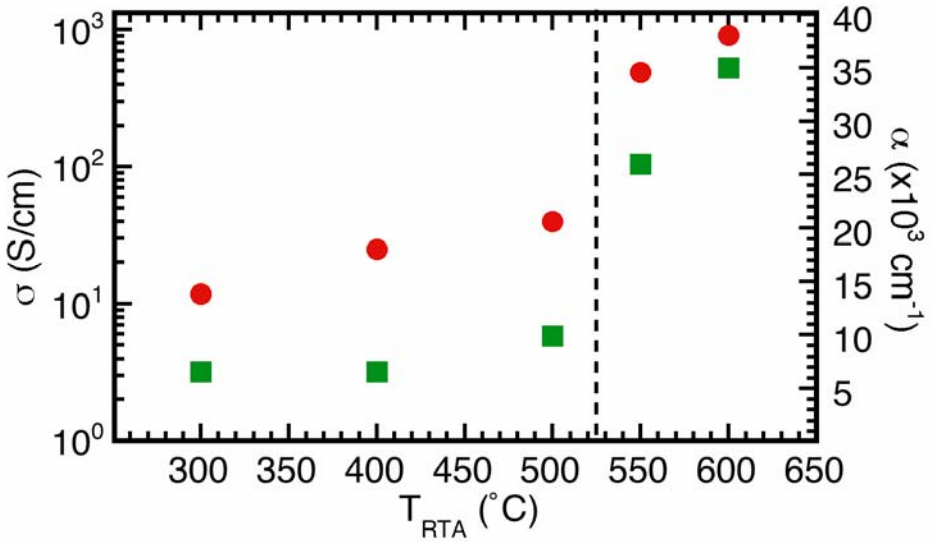

Figure 4.10. Conductivity (circles, left scale) and absorption coefficient at 800 nm (squares, right scale) of crystalline BaCuTeF films by RTA in Ar (g). Phase separation occurs above 500˚C.

The electrical conductivity as a function of RTA temperature of BaCuTeF films is shown in Fig. 4.10. Film conductivity increases with higher annealing temperature from about 10 to 40 S/cm. Like BaCuSF films subjected to RTA (see Chapter 3), the increase in conductivity of BaCuTeF films with higher temperature is due in part to an increasing carrier concentration (up to ~1 x 10^{21} cm^{-3}) via creation of Cu-vacancies, and in part to improving carrier mobility (up to 0.2 cm^2/Vs) of higher crystallinity films. Seebeck and Hall coefficients are positive, identifying the hole conduction mechanism. Low Seebeck coefficients around 50 μV/K are expected from materials with high carrier concentration.

The variation of the absorption coefficient with the RTA temperature is also depicted in Fig. 4.10. Crystalline BaCuTeF films annealed in the 300 – 500˚C temperature range exhibit similar absorption coefficients around 8000 cm^{-1} at 800 nm and longer wavelengths (800 nm corresponds to 1.55 eV). The absorption coefficient

increases towards shorter wavelengths. Although direct band gaps are estimated near 3 eV, the slow onset of absorption near the band edge considerably decreases optical transparency to 55 % in the 400-800 nm range. Films prepared *in-situ* at elevated substrate temperatures exhibit sharper absorption edges, and higher transparency as discussed in section 4.3.3.

An increase in conductivity, as well as in absorption (Fig. 4.10 a and b) at RTA temperatures above 500˚C, marks the presence of highly conductive Cu_xTe_y and $BaCu_2Te_2$ [9] phases in the resulting films. A significant decrease of film thickness, from 150 nm of the lower temperature annealed films, to ~90 nm is observed, indicating the volatility of some components.

In summary, it is shown that crystalline BaCuTeF can be prepared by RTA in Ar (g) up to 500˚C. The obtained films are more conductive (~30 S/cm) than the *in-situ* prepared counterparts. The high hole carrier concentration and wide band gap of RTA prepared BaCuTeF films are good candidates for solar cell applications.

4.4. Conclusions

Epitaxial thin films of BaCuTeF are deposited *in-situ* by PLD on single crystal MgO (100) substrates between 500 and 600 ˚C. The highest conductivity, 167 S/cm, and mobility, 8 cm^2/Vs, are obtained for deposition in the presence of 1 mTorr Ar. BaCuTeF films are transparent in the visible range with a 3-eV direct band gap. This optical gap is much higher than 2.3 eV measured in bulk samples. Single-phase polycrystalline BaCuTeF films are produced by PLD deposition on fused SiO_2

substrates in the temperature range 300 to 550 ˚C. These polycrystalline films have lower carrier mobility and conductivity, but lower absorption coefficients than their epitaxial counterparts. Furthermore, films can be prepared by an *ex-situ* Ar (g) RTA process, and a moderate ~40 S/cm conductivity is achieved.

This work is supported by the National Science Foundation under DMR 0245386. We thank Kurt Langworthy at CAMCOR for assistance with the SEM micrographs, Prof. David Johnson for the use of the Bruker X-ray diffractometer, and Prof. Guenter Schneider for useful discussion.

References

1. C.-H. Park, R. Kykyneshi, A. Yokochi, J. Tate, and D. A. Keszler, J. Solid State Chem., 180 (2007) 1672
2. C.-H. Park, D. A. Keszler, H. Yanagi, and J. Tate, Thin Solid Films 445 (2003) 288
3. H. Yanagi, J. Tate, S. Park, C.-H. Park, and D. A. Keszler, Appl. Phys. Lett. 82 (2003) 2814
4. H. Hiramatsu, K. Ueda, H. Ohta, M. Orita, M. Hirano, and H. Hosono, Appl. Phys. Lett. 81 (2002) 598
5. H. Hiramatsu, K. Ueda, H. Ohta, M. Hirano, T. Kamiya, and H. Hosono, Appl. Phys. Lett. 82 (2003) 1048
6. H. Hiramatsu, K. Ueda, K. Takafuji, H. Ohta, M. Hirano, T. Kamiya, and H. Hosono, J. Mater. Res. 19 (2004) 2137
7. R. E. Presley, D. Hong, H. Q. Chiang, C. M. Hung, R. L. Hoffman, and J. F. Wager, Solid-State Electronics 50 (2006) 500
8. C.-H. Park, PhD dissertation, Oregon State University, 2005, Call # LD4330 2005D .P37.

9. Y. C. Wang, F. J. DiSalvo, J. Solid State Chem. 156 (2001) 44.
10. G. K. Williamson and W. H. Hall, Acta Metallurgica 1 (1953) 22
11. S. Park, D. A. Keszler, M. M. Valencia, R. L. Hoffman, and J. F. Wager, Appl. Phys. Lett. 80 (2002) 4393
12. H. Hiramatsu, K. Ueda, K. Takafuji, H. Ohta, M. Hirano, T. Kamiya, H. Hosono, Appl. Phys. A 79 (2004) 1521
13. Y. Hishikawa, N. Nakamura, S. Tsuda, S. Nakano, Y. Kishi, and Y. Kuwano, Jap. J. Appl. Phys. 30 (1991) 1008
14. P. Y. Yu and M. Cardona, Fundamentals of Semiconductors: Physics and Materials Properties, 3rd edition, Springer, 2001 p. 269.
15. S.B.Zhang, S.-H. Wei, and A. Zunger, Jour. Appl. Phys. 83 (1998) 3192
16. X. Nie, S.-H. Wei, and S. B. Zhang, Phys. Rev. Lett. 88 (2002) 066405
17. S. M. Sze, Physics of Semiconductor Devices, 2nd edition, John Wiley and Sons, New York , Chichester, Brisbane, Toronto (1981), p. 828
18. A. Romeo, M. Terheggen, D. Abou-Ras, D.L. Batzner, F.-J. Haug, M. Kalin, D. Rudmann and A.N. Tiwari, Progr. Photovolt. 12 (2004) 93
19. Handbook of Photovoltaic Science and Engineering, edited by A. Luque and S. Hegedus, John Wiley and Sons, Ltd (2003)

Chapter 5. BaCuSeF p-type, semiconducting thin films

Parts of this chapter are published in
J. Tate, R. Kykyneshi, P. F. Newhouse, J. Kinney, D. H. McIntyre, D. A. Keszler, P. A. Hersh, Thin Solid Films (2007) in press

5.1. Introduction

The physical properties of BaCuSF and BaCuTeF semiconductors are described in earlier chapters. In this chapter, I discuss the preparation, characterization and properties of thin films of BaCuSeF – the last member of the layered chalcogenide-fluoride materials of the P4/nmm space group. In the periodic table Se lies in between the group VI elements of S and Te, thus intermediate properties are to be expected. Based on band structure calculations [1, and Chapter 1], BaCuSeF is expected to have a band-gap between those of BaCuSF and BaCuTeF. Indeed, diffuse-reflectance measurements on BaCuSeF powders [2] reveal a band gap of 2.9 eV, which is below that of BaCuSF at 3.1 eV. Furthermore, the conductivity and mobility are expected to improve compared to BaCuSF due to the higher mixing of Cu-3*d* and Se-4*p* states near the top of the valance band. Conductivity measurements on a BaCuSeF pressed pellet [3] yield 0.06 S/cm, similar to the S-containing compound, but its temperature dependence is only slightly activated. For comparison, undoped BaCuTeF powders [4, Chapter 4] have a band gap of 2.3 eV and are degenerate with a room temperature conductivity of 7 S/cm.

So far, hole-carrier, transparent, semiconducting films of BaCuSF and BaCuTeF have been presented. In Chapter 2 it is shown that BaCuSF thin films are

hard to prepare and thus the material properties are difficult to control. BaCuTeF thin films have high conductivity (167 S/cm) due to a large inherent carrier concentration (~ 10^{20} cm^{-3}) and high hole mobility, as described in Chapter 3. In this Chapter, BaCuSeF thin films are deposited on fused SiO_2 and single crystal MgO substrates by PLD. The electrical and optical properties of textured and polycrystalline BaCuSeF thin films are presented and compared to those of BaCuSF and BaCuTeF.

5.2. Experiment

The preparation of the BaCuSeF target by solid state synthesis from BaSe, Cu_2Se and BaF_2 is described in an earlier publication from our group [3].

Thin films are deposited using the experimental setup described in section 2.2. Typical deposition parameters are 1 and 1.5 J/cm^2 fluence, repetition rate 10 Hz and substrate-target distances of 5 – 6 cm. The changes in film quality in this chapter are attributed to the variation of laser fluence, and thus compositional changes in the plume and ultimately in the grown film. The target-substrate distance does not contribute to film quality due to the much longer mean free path of the plasma particles in background pressures below 10 mTorr, and influences only the thickness uniformity.

Standard characterization techniques introduced in section 2.3 are employed.

5.3. Results and Discussion

5.3.1. Textured films

Single-phase, high quality films of BaCuSeF are obtainable *in-situ* by PLD from ceramic targets onto substrates held at 600˚C. BaCuSeF films are deposited on a single crystal MgO (100), at 600˚C, 1 mTorr Ar (g) and 1 J/cm^2 laser fluence. The MgO (100) substrate provides an excellent growth template for BaCuSeF with a lattice mismatch of only 0.6%. The *a*-lattice parameters are 4.239 Å for BaCuSeF and 4.213 Å for MgO. Strong (00*l*) peaks are observed in the XRD pattern in Fig. 5.1, from predominantly *c*-axis oriented film growth. Presence of the (102) and (204) peaks indicates grain growth in 45˚ misalignment with respect to the *c*-axis direction. The in-plane ϕ-scan also shows the non-epitaxial film growth. The occurrence of the BaCuSeF (102) reflection at ϕ-angles other than those where MgO (202) peaks are observed, indicates in-plane misalignment, as shown in the inset of Fig. 5.1. In particular, BaCuSeF (110) planes grow in alignment and at a 45˚ rotation with respect to the MgO (110) plane. We conclude that the current deposition parameters result in textured (highly *c*-axis oriented) BaCuSeF films. The optimal deposition parameters for epitaxial films growth are yet to be found. Similar deposition parameters produce epitaxial films in BaCuTeF [5].

The lattice parameters of the textured BaCuSeF film are determined from the XRD peak positions from the pattern shown in Fig. 5.1. The single crystal MgO (100) substrate provides an excellent reference for alignment. A 0.3% decrease of the

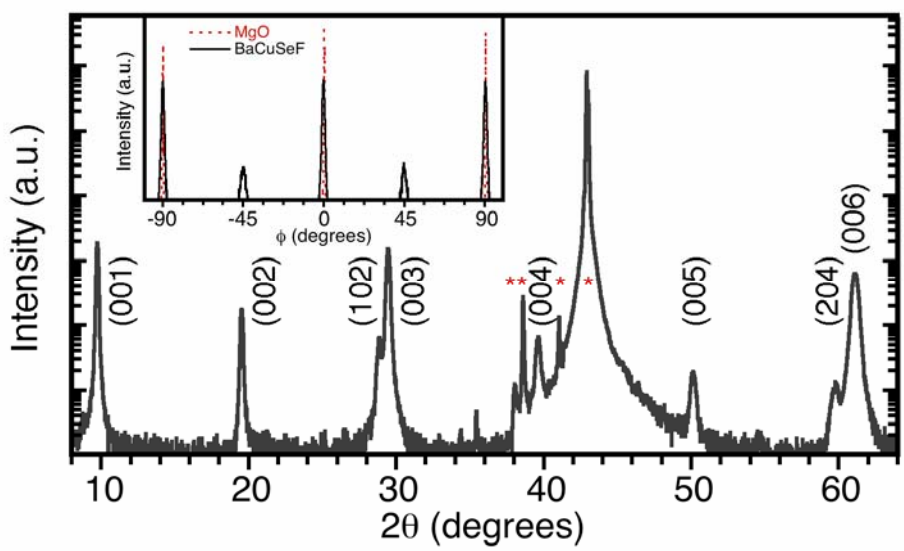

Figure 5.1. XRD pattern of textured BaCuSeF film on MgO (100) substrate. Peaks other then (00*l*) reflections are present. Inset: in-plane orientation of BaCuSeF film on MgO indicating non-epitaxial growth. Film is deposited at 1 J/cm^2 laser power.

c-lattice parameter is found, from 9.1217 nm in BaCuSeF reference [JCPDS # 82-1492] to 9.09(2) nm in the film determined from the (00*l*) peaks. The *a*-lattice constant also decreases by about 0.4% from the referenced 4.2391 nm to 4.22(1) nm calculated using the (102) peak of the BaCuSeF film. A Gaussian fit to the rocking curve of the (003) peak yields a FWHM of 0.7˚. The Williamson-Hall method [6] is used to determine the strain of 0.5% along the c-axis from the broadening of the (00*l*) reflections. The calculated film thickness of 170 nm is in good agreement with the value determined from optical thin film interference measurement. A similar decrease of the lattice parameters and FWHM of the (003) peak is observed in textured BaCuTeF films [see Chapter 4 or Ref. 5].

A surface SEM image of the textured film is shown in Fig. 5.2. Cracking or void formation is evident. The latter can occur due to thermal expansion mismatch between the film and substrate materials. As for the former case, similar surfaces

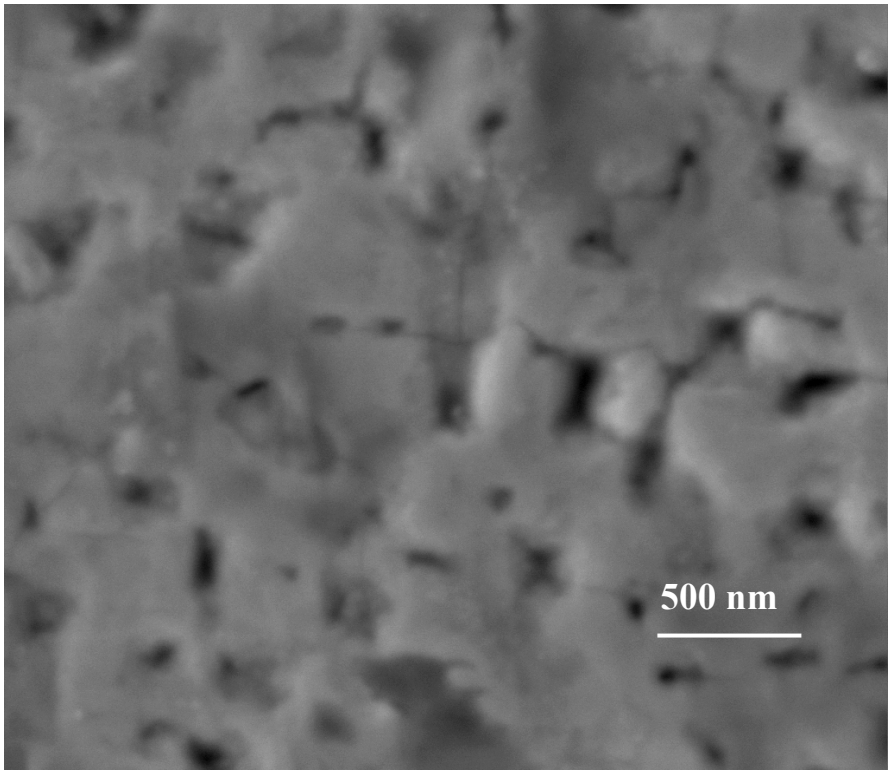

Figure 5.2. SEM micrograph of textured BaCuSeF thin film exhibiting voids.

were observed for $YBa_2Cu_3O_7$ films by PLD, deposited at a low deposition rate [7]. The authors [7] conclude that adjusting the deposition rate and substrate temperature is necessary to obtain film coalescence (smooth films) at a given film thickness. Increasing the deposition rate by increasing the laser fluence is not viable, because, as discussed below, phase separation occurs in polycrystalline BaCuSeF films at 1.5 J/cm^2 fluence. Other means of increasing the deposition rate are higher repetition rate or possibly higher deposition gas pressure for fully epitaxial film growth. On a larger scale micrograph, few-micrometer-size features are seen on the film surface with a density of 0.4 μm^{-2}, due to splattering from the target during PLD.

The room-temperature conductivity of the textured, undoped BaCuSeF film is 0.4 S/cm. Hall measurements performed in the van der Pauw geometry give carrier

concentration 1.7 x 10^{18} cm^{-3} and mobility 1.5 cm^2/Vs. A much higher carrier concentration, 1.3 x 10^{20} cm^{-3}, and mobility, 8 cm^2/Vs, are obtained in the epitaxial BaCuTeF films. Textured BaCuSF films produced by 500˚C Ar (g) RTA exhibit similar conductivity of 0.2 S/cm, but the mobility is not measurable. The carriers are presumably produced by Cu vacancies in these nominally undoped compounds. Seebeck and Hall coefficient measurements confirm the *p*-type nature of the carriers in BaCuSeF film. The high Seebeck coefficient of +310 μV/K is in good agreement with the low carrier concentration in the film.

Optical transmission and reflection measurements (Fig. 5.3) performed for the highly oriented BaCuSeF yield a 2.9 eV band gap, and about 65% average transmission in the visible optical range. When reflection losses are accounted for, we obtain over 90% corrected transmission, $T/(1-R)$, in BaCuTeF at wavelengths longer than 600 nm. Fitting of the thin film fringes results in a film thickness of 170 nm and refractive index change from 2.54 to 2.01 in the 400 – 800 nm wavelength range.

BaCuQF thin films exhibit band gaps of 3 eV (BaCuTeF), 2.9 eV (BaCuSeF), and over 3.2 eV in BaCuSF. The measured band gaps are consistent with those observed in powder studies [2,4], except that BaCuTeF films are far more transparent than would be expected from the 2.3 eV optical gap observed in the in powder form, addressed in Chapter 4. The refractive index increases with increasing anion size in BaCuQF: for example, at 800 nm n = 1.8, 2.0, 2.2 for Q = S, Se, Te, respectively.

Absorption coefficients are calculated from the reflection corrected transmission, $T/(1-R)$, with the results shown in Fig. 5.4, bottom line. The large absorption change indicating the band gap also includes excitonic absorption in

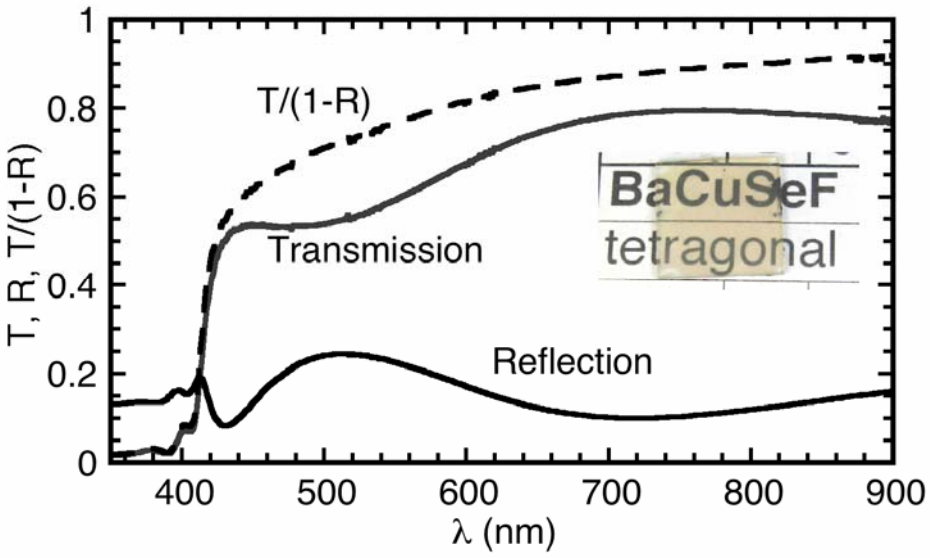

Figure 5.3. Optical transmission and reflection of BaCuSeF film on MgO (100) substrate. Sharp exciton features are observed near 400 nm and an onset of transmission above 400 nm. The slightly yellow appearance of the film is shown in the inset.

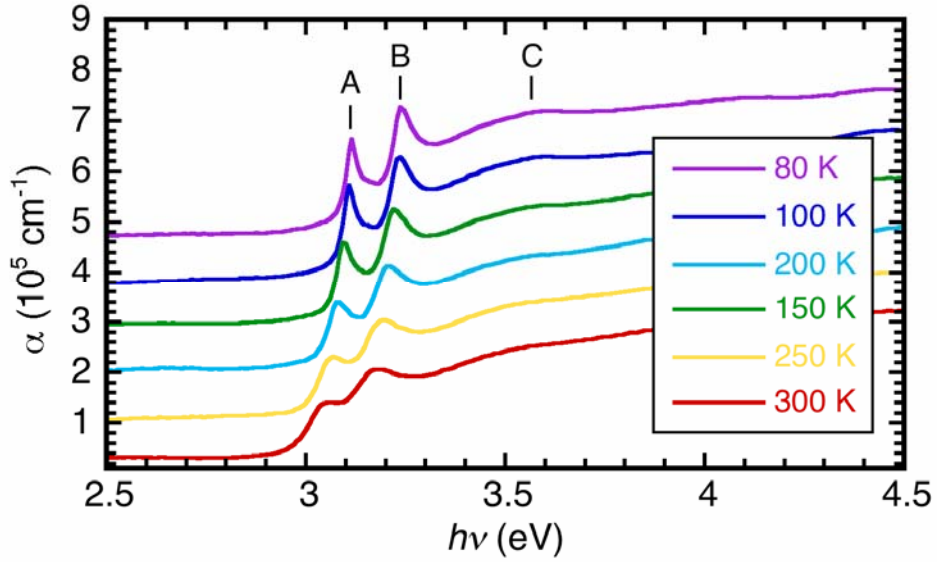

Figure 5.4. Absorption spectra of BaCuSeF textured thin film. The measurement temperature is decreased from bottom up in the 300 K to 80 K range. The room temperature line is to scale and the upper lines are offset by a constant value for clarity. [measured by J. Kinney]

BaCuSeF marked by letters *A*, *B* and *C*. Similar excitonic structure has been observed in BaCuSF films, as discussed in section 3.3.3, but not in BaCuTeF epitaxial films (Chapter 4). In BaCuSF, the polycrystalline nature of the film is believed to broaden the excitonic lines, while in BaCuTeF the large number of carriers and higher carrier mobility may suppress the exciton.

The three excitonic absorption peaks observed sharpen with lower measurement temperature (Fig. 5.4) as expected, due to lower thermal smearing and high film quality. The peak positions at room temperature are 3.04 eV, 3.17 eV and 3.42 eV for the *A*, *B* and *C* absorptions, respectively. The exciton structure is very similar to the case of BaCuSF films [see Chapter 3]. The peak energies are red-shifted due to the lower band gap of BaCuSeF, but the energy separations of the absorption maxima are comparable. The excitons are confined in 2 dimensions due to the layered structure of the crystal lattice and the contributions of only Cu and Se atomic states to the valence band maximum and conduction band minimum, as described in Chapter 1 and section 3.3.3. Assuming that peak *A* and peak *B* of Fig. 5.4 correspond to $n = 1$ and $n = 2$ exciton series, applying the 2D hydrogen model (Chapter 3, Eq. 3.4) results in a binding energy of ~34 meV. This value is yet to be verified experimentally. In this case, peak *C* presumably corresponds to a transition from an exciton state near the VBM to a higher state in the CBM, possibly to Ba 5*p* states. On the other hand, a similar exciton structure is reported in thin films of the isostructural LaCuOSe [8], according to which the *A* and *B* absorptions are attributed to peak splitting due to spin-orbit interactions of the chalcogen ions. The splitting is observed from the dynamics of the exciton structure in LaCuO(S,Se) solid solutions and its limiting members. In

this case peak *C* in BaCuSeF corresponds to the $n = 2$ excitonic absorption, but the splitting of the peak is not resolved and lower temperature absorption measurements are necessary. High quality solid solution BaCu(S,Se)F thin film are needed to resolve this issue.

Excitonic emission has not been observed to date in the textured BaCuSeF film, although orange photoluminescence is observed by eye at 77 K under 270 nm UV-irradiation. It is hence possible, that a non-radiative pathway exists for relaxation of excited electrons to lower energy states in the gap.

The BaCuQF family exhibits a relatively low absorption for a given conductivity (Fig. 5.5). High quality thin films of these materials have been prepared. While their absolute absorption coefficients do not rival the best *n*-type transparent conductors, it appears that the absorption price for *p*-type conductivity is not so great

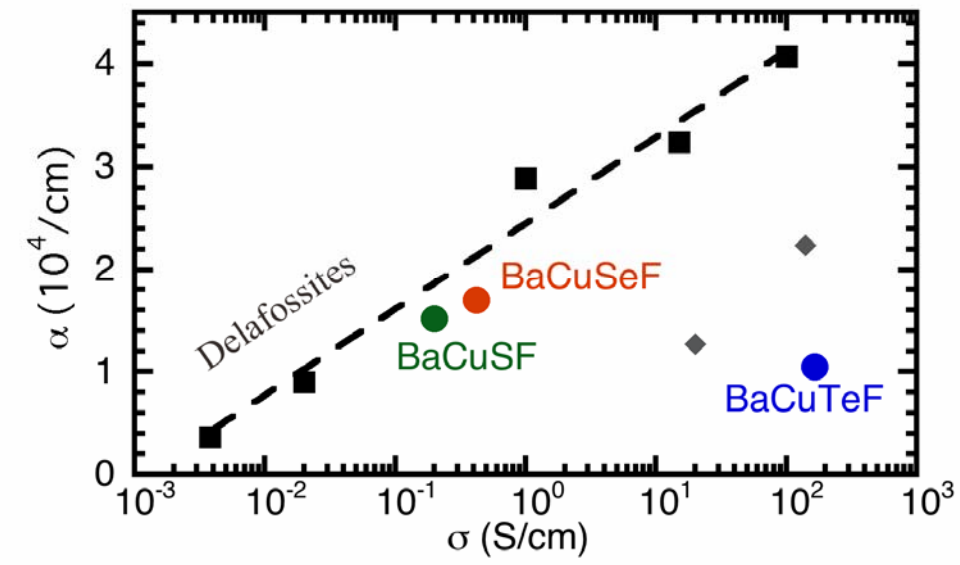

Figure 5.5. Absorption coefficient versus conductivity of *p*-type transparent conductors (see text for explanation of symbols).

in the chalcogenide-fluorides and oxy-chalogenides as in the *p*-type Cu-based oxides. Example oxides from the literature, $CuInO_2$:Sn [9], $CuGaO_2$ [10], $CuScO_{2+y}$ [11], $CuYO_2$:Ca [12], $CuCrO_2$:Mg [13], are represented by squares in Fig. 5.5, while LaCuOS:Sr [14] and LaCuOSe:Mg [15] are represented by diamonds.

5.3.2. Polycrystalline films

Although high quality BaCuSeF thin films can be deposited on expensive MgO (100) substrates, it is of importance to research the properties of polycrystalline films, growing on lattice mismatched or amorphous substrates. Such polycrystalline BaCuSeF films are prepared on amorphous SiO_2 substrates in the 300 – 500˚C temperature range. The lower temperature is the crystallization temperature of the deposited film, below which the resulting films are amorphous, while 500˚C is about the highest substrate surface temperature we can achieve in the deposition system for a 1.2 mm thick SiO_2 substrate.

XRD patterns of BaCuSeF thin films deposited at various temperatures on SiO_2 and laser fluence of 1.5 J/cm^2 and 1 J/cm^2 are shown in Fig. 5.6. The presence of various crystallographic plane reflections indicates the polycrystalline nature of the films. BaCuSeF films are polycrystalline when deposited at 300˚C onto SiO_2 substrates in vacuum (Fig. 5.6a). A preferential *c*-axis orientation is observed with increasing substrate temperature (Fig. 5.6b), and the strength of the orientation also increases when 10^{-3} Torr Ar (g) (Fig. 5.6c) is introduced. The preferred orientation is manifested in increasing intensity of (00*l*) peaks, such as (001) at θ = 9.4˚, and

decreasing intensity of (*hk*0) peaks, *eg.* (200) at θ = 42.6˚, in the diffraction patterns of Fig. 5.6. Such preferential orientation film growth is observed in BaCuTeF films with increasing substrate temperature, and in BaCuSF with increasing rapid thermal annealing temperature in Ar (g).

A small amount of BaF_2 phase is also present, with a characteristic peak near 25˚. The appearance of the secondary phase is attributed to the laser fluence used during PLD of polycrystalline films. Although single-phase textured films are prepared at 1.0 J/cm^2 laser fluence on single crystal MgO substrates, as described in the previous section, this laser power value could be too high for film deposition on amorphous SiO_2 substrates, due to a dissimilar film growth mechanism. A film deposited at 0.5 J/cm^2 laser power shows no BaF_2 peak, but a $BaCu_2Se_2$ impurity peak appears. Thus, optimal laser fluence lies between 0.5 and 1 J/cm^2 for single-phase

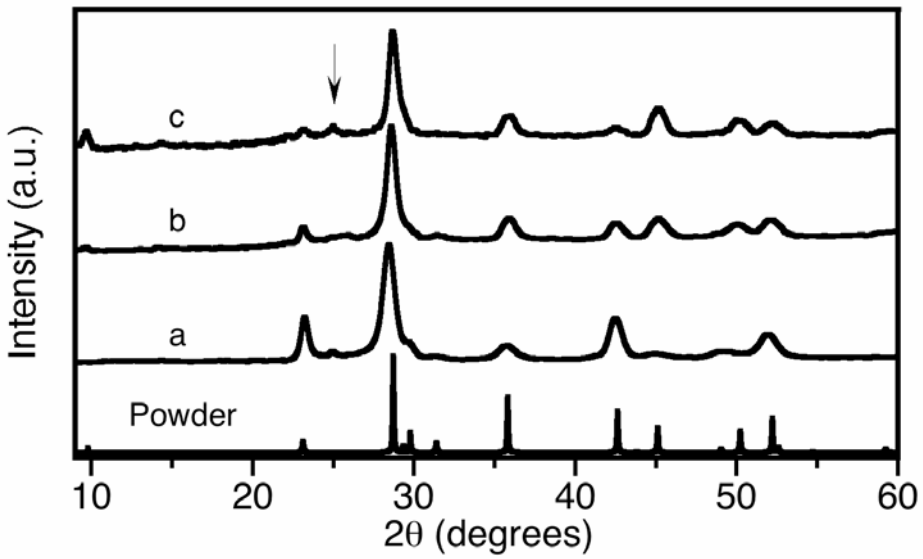

Figure 5.6. Polycrystalline XRD patterns of BaCuSeF films deposited at a) 10^{-3} Torr Ar, 450˚C and 1 J/cm^2, b) vacuum, 450˚C and 1 J/cm^2, and c) vacuum, 300˚C and 1.5 J/cm^2. The position of BaF_2 impurity phase is marked by the arrow.

BaCuSeF film deposition onto SiO_2 substrates, and for epitaxial film growth on MgO (100) substrates.

To obtain high quality BaCuSeF films the use of 1 J/cm^2 laser fluence or below is necessary. As described in section 3.3.2, BaCuSF films have to be deposited at a low 0.5 J/cm^2 laser power to obtain good film stoichiometry. As described in Chapter 4, BaCuTeF films are deposited at laser fluence between 1 – 2 J/cm^2 resulting in single-phase films, probably due to higher stability of $CuTe_x$ complexes. Thus, we find that in order to obtain phase-impurity free films of BaCuQF materials the use of decreasing laser fluence from ~1.0 to 0.5 J/cm^2 with smaller chalcogen atom size (in order Te, Se and S) is required.

The electrical conductivity of BaCuSeF films on SiO_2 substrates is at least an order of magnitude lower than of its textured counterpart. The dependence of film conductivity on deposition parameters is summarized in Fig. 5.7. The conductivity of 1.5 J/cm^2 deposited films increases at higher substrate temperatures, owing to the preferential *c*-axis growth. Lowering the laser fluence to 1 J/cm^2 increases conductivity at a set substrate temperature. The electrical properties of the film are further enhanced by introduction of 10^{-3} Torr Ar (g) during deposition. The improved structure of the film allows the reliable measurement of a positive Hall coefficient. The carrier concentration of 3 x 10^{18} cm^{-3} is in good agreement with the high positive Seebeck coefficient of +230 μV/K, similarly to the textured film on MgO substrate. Using the conductivity of the film 7.5 x 10^{-2} S/cm and carrier concentration, the carrier mobility of 0.15 cm^2/Vs is calculated.

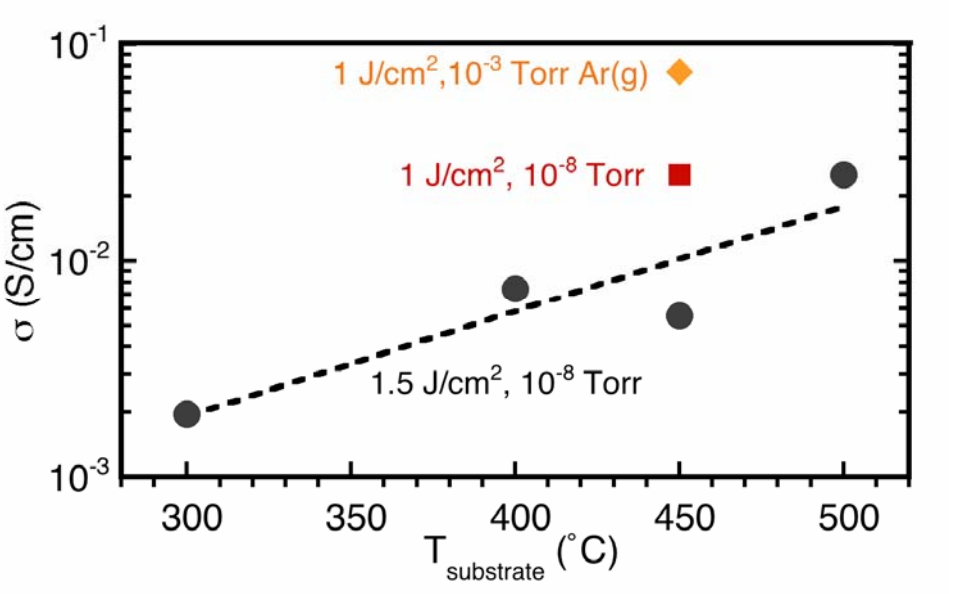

Figure 5.7. Electrical conductivity of BaCuSeF films deposited in vacuum at 1.5 J/cm^2 (circles, line is guide for the eye), in vacuum at 1 J/cm^2 (square) and in 10^{-3} Torr Ar (g) and 1 J/cm^2 (diamond).

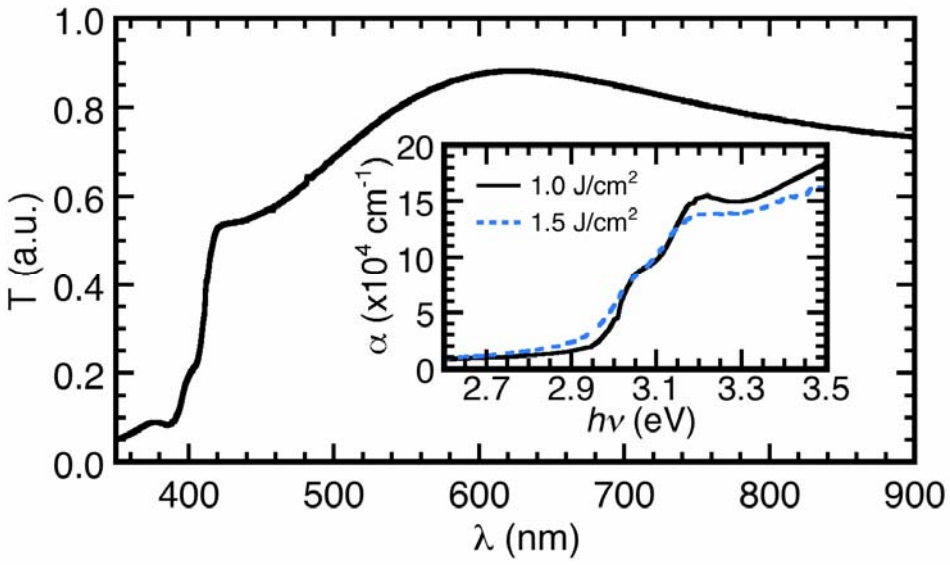

Figure 5.8. Optical transmission of a 140 nm thick BaCuSeF deposited at 1 J/cm^2 laser fluence, with excitonic absorption features near 400 nm. Inset: Absorption coefficients of films deposited at 1 J/cm^2 and 1.5 J/cm^2. The excitons decrease in intensity at higher laser fluence.

High optical transmission is characteristic to polycrystalline BaCuSeF. The average transparency of the film 140nm thick film, shown in Fig. 5.8, is 77 % in the 410 – 800 nm visible wavelength range. Below 410 nm, some of the blue light is absorbed due to the onset of the absorption edge indicating the band gap, resulting in the yellow tinge of the films. The high transmission in most of the visible range translates into low absorption coefficients of ~ 5300 cm^{-1}, near 520 nm, and further decreases at higher wavelengths. The absorption below the absorption edge in BaCuSeF is the lowest amongst the polycrystalline BaCuQF thin films.

Excitons are observed in polycrystalline films as well as in the highly textured BaCuSeF film, probably due to a better film structure even on SiO_2 substrates at lower laser fluence. The exciton absorptions weaken with higher laser fluence, as shown in the inset of Fig.5.8, and blurring of the absorption edge onset is also present.

BaCuSeF films are moderately conductive and the carrier mobility is measurable. For comparison, Hall coefficients are not measurable in BaCuSF films of similar conductivity, indicating low carrier mobility and high carrier concentration. Polycrystalline BaCuTeF films do exhibit mobility of ~ 0.2 cm^2/Vs and a high carrier concentration of 10^{20} cm^{-3}. The electrical and optical properties of the polycrystalline films suggest that BaCuSeF is a good candidate for transparent thin film transistor (TTFT) application. In addition, the low work function of 3.6 eV [16] of BaCuSeF allows the use of common metals as Al and Cu for contact preparation. Good carrier mobility and low carrier concentration and absorption are key features of a successful TTFT material candidate.

5.4. Conclusions

Highly textured BaCuSeF thin film is deposited *in-situ* by PLD on a single crystal MgO substrate at a moderate 600˚C substrate temperature and 1 J/cm^2 laser fluence. The hole carrier mobility of 1.5 cm^2/Vs and low carrier concentration of 1.7 x 10^{18} cm^{-3} are measured in the textured film. Strong excitonic absorption in the ultra-violet is present in the film, but only orange light emission is observed so far at low temperatures. Polycrystalline BaCuSeF films exhibit *c*-axis orientation with increasing substrate temperature and laser fluence of ~ 1 J/cm^2. The better structural properties lead to improving hole-carrier mobility (0.15 cm^2/Vs) and lower absorption in the polycrystalline films. The ability to prepare high quality BaCuSeF on an amorphous substrate, makes BaCuSeF a good candidate for transparent electronics applications.

References

1. H. Yanagi, J. Tate, S. Park, C.-H. Park and D.A. Keszler, J. Appl. Phys. 100 (2006) 083705
2. C.-H. Park, D. A. Keszler, H. Yanagi, and J. Tate, Thin Solid Films 445 (2003) 288
3. H. Yanagi, J. Tate, S. Park, C.-H. Park, and D. A. Keszler, Appl. Phys. Lett. 82 (2003) 2814
4. C.-H. Park, R. Kykyneshi, A. Yokochi, J. Tate, and D. A. Keszler, J. Solid State Chem. 180 (2007) 1672

5. R. Kykyneshi, D. H. McIntyre, J. Tate, C.-H. Park, D. A. Keszler, J. Solid State Sci. (2007) in print
6. G. K. Williamson and W. H. Hall, Acta Metallurgica 1, 22 (1953).
7. C. C. Chang, X. D. Wu, R. Ramesh, X. X. Xi, T. S. Ravi, T. Venkatesan, D. M. Hwang, R. E. Muenchausen, S. Foltyn, and N. S. Nogar, Appl. Phys. Lett. 57 (1990) 1814
8. K. Ueda, H. Hiramatsu, H. Ohta, M. Hirano, T. Kamiya, and H. Hosono, Phys. Rev. B 69 (2004) 155305
9. H. Yanagi, T. Hase, S. Ibuki, K. Ueda, and H. Hosono, Appl. Phys. Lett. 78 (2001) 1583
10. J. Tate, M. K. Jayaraj, A. D. Draeseke, T. Ulbrich, A. W. Sleight, K. A. Vanaja, R. Nagarajan, J. F. Wager, and R. L. Hoffman, Thin Solid Films 411 (2002) 119
11. R. Kykyneshi, B. C. Nielsen, J. Tate, J. Li, and A. W. Sleight, J. Appl. Phys. 96 (2004) 6188
12. M.K. Jayaraj, A. D. Draeseke, J. Tate, and A. W. Sleight, Thin Solid Films 397 (2001) 244
13. R. Nagarajan, A. Draeseke, A. W. Sleight, and J. Tate, J. Appl. Phys. 89 (2001) 8022
14. H. Hiramatsu, M. Orita, M. Hirano, K. Ueda, and H. Hosono, J. Appl. Phys. 91 (2002) 9177
15. H. Hiramatsu, K. Ueda, H. Ohta, M. Hirano, T. Kamiya, H. Hosono, Thin Solid Films 445 (2003) 304
16. H. Yanagi, J. Tate, S. Park, C.-H. Park, D. A. Keszler, M. Hirano, and H. Hosono, J. Appl. Phys. 100 (2006) 083705

Chapter 6. High conductivity in amorphous and crystalline $Zn_2In_2O_5$ thin films.

6.1. Introduction

Transparent conductive oxides (TCO) are heavily researched due to high industrial demand in flat panel display, solar cell and glass coating technologies, for use as conductive leads and shielding, where transparency in the visible optical spectrum is required. The most commonly used TCOs are tin-doped indium oxide or ITO (In_2O_3:Sn) and amorphous indium-zinc-oxide, usually In_2O_3 with 10 wt. % ZnO [1]. Electrical properties of In_2O_3-$(ZnO)_k$ pressed powder pellets [2] with various ZnO content reveals that the highest conductivity of phase pure material is achieved in $Zn_3In_2O_6$, and decreases with higher ZnO content.

$Zn_2In_2O_5$ (ZIO) thin films deposited by sputtering methods exhibit conductivity up to 3000 S/cm [3,4], competing with Al-doped ZnO [5]. The reported optical band gap of ZIO extends over a large range of values between 2.9 and 3.5 eV [4,6], but high optical transparency >80% below the gap energy is common to all.

Al and Ga are well-known donor dopants in ZnO and Sn is the most common dopant in In_2O_3. There exist studies of Al [7], Sn [8,9], Mg and Ga [10] doping in $Zn_2In_2O_5$ thin films. In all cases, the dopants act as scattering centers in ZIO and do not contribute significantly to conductivity by carrier generation. Thus, donor doping of these materials has proved to be ineffective as of now.

In this work we focus on a In_2O_3-$(ZnO)_k$ TCO material with $k = 2$ ($Zn_2In_2O_5$). Thin films are deposited from targets of $Zn_2In_2O_5$ composition. The deposition

conditions, such as laser power and target substrate distance, are optimized at room temperature for ZIO. The electrical and optical properties of undoped and W doped thin films at elevated substrate temperatures and in various process gases are investigated. The choice of the dopant is motivated by a recent report of high mobility in In_2O_3:W thin films [11].

6.2. Experiment

$Zn_2In_2O_5$ (ZIO) and $Zn_2In_2O_5$:W (ZIOW) thin films are prepared by the pulsed laser deposition (PLD) technique. The undoped ZIO is prepared from a 2:1 molar mixture of ZnO and In_2O_3. The tungsten doped target is obtained by replacing 5 at. % of In_2O_3 by WO_3. The intimately mixed powders are pressed into 2.5 cm targets and sintered at 1350˚C. Corning 1737 substrates with Hall-cross shadow masks are mounted across from the target in the deposition chamber. The base pressure in chamber is 2 x 10^{-9} Torr, and films are deposited in vacuum and 1 and 10 mTorr gas pressures of grade 4 or higher purity Ar, Ar – 20% O_2 and O_2. A 248 nm LP Compex 203 excimer laser is used for target ablation at 10 Hz repetition rate. The laser beam is focused onto the target and the resulting spot size is 0.028 cm^2 (at 1.5 J/cm^2 fluence), with ±0.04 cm^2 shifts when increase (larger spot) or decrease (smaller spot) in laser power are made. The deposition gas, target-substrate distance, laser fluence and substrate temperature are varied from film to film during depositions to find optimal deposition parameters. Standard characterization techniques described in Chapter 2 are used for physical property determination of the films.

6.3. Results and Discussion

6.3.1. Optimization of room temperature deposited $Zn_2In_2O_5$ films.

Thin films are deposited at room temperature and UHV from a $Zn_2In_2O_5$ composition target to study the influence of laser power and deposition geometry on film properties in the amorphous phase. First, we consider the dependence of electrical and optical properties on the laser fluence, while keeping a constant substrate target distance of 5 cm. All films deposited at room temperature are amorphous as determined by XRD. Atomic force microscopy images of the ZIO film surfaces are featureless with a root-mean-square (RMS) roughness around 0.5 nm, although small (~100 nm) particulates of 0.15 μm^{-2} density do appear towards the low end of laser energies around 1 J/cm^2 used in depositions.

The dependence of electrical and optical properties on laser fluence is depicted in Fig. 6.1 and Fig. 6.2 respectively. The conductivity of amorphous $Zn_2In_2O_5$ (a-ZIO) films decreases with higher laser fluence due to lower carrier concentration and impaired mobility compared to films deposited at 1 - 1.5 J/cm^2. Such decrease in mobility with lower carrier concentration as shown on Fig. 6.1 is observed in other In_2O_3 – ZnO compounds [12,13]. The mobility is maximal for a carrier concentration of 2 - 4 x 10^{20} cm^{-3}. Below this value, potential barriers in the amorphous material cause carrier percolation instead of ballistic transport [13]. Above this value, scattering from defects (oxygen vacancies) [14] increases. Both phenomena likely contribute to the drop in mobility in the present case.

The average optical transmission (Fig. 6.2) is the highest for the films deposited at a laser fluence of 1.5 - 1.8 J/cm^2 and falls off rather rapidly for higher and lower energy densities. All samples have a similar thickness of ~190 ± 10 nm and therefore can be compared directly. An indirect band gap evaluation is used due to the amorphous nature of the films, where $(\alpha h\nu)^{1/2}$ is plotted against the incident light energy $h\nu$, and α is the absorption coefficient. The value of the band gap E_g is determined from the extrapolation of the linear part of the plot to the incident photon

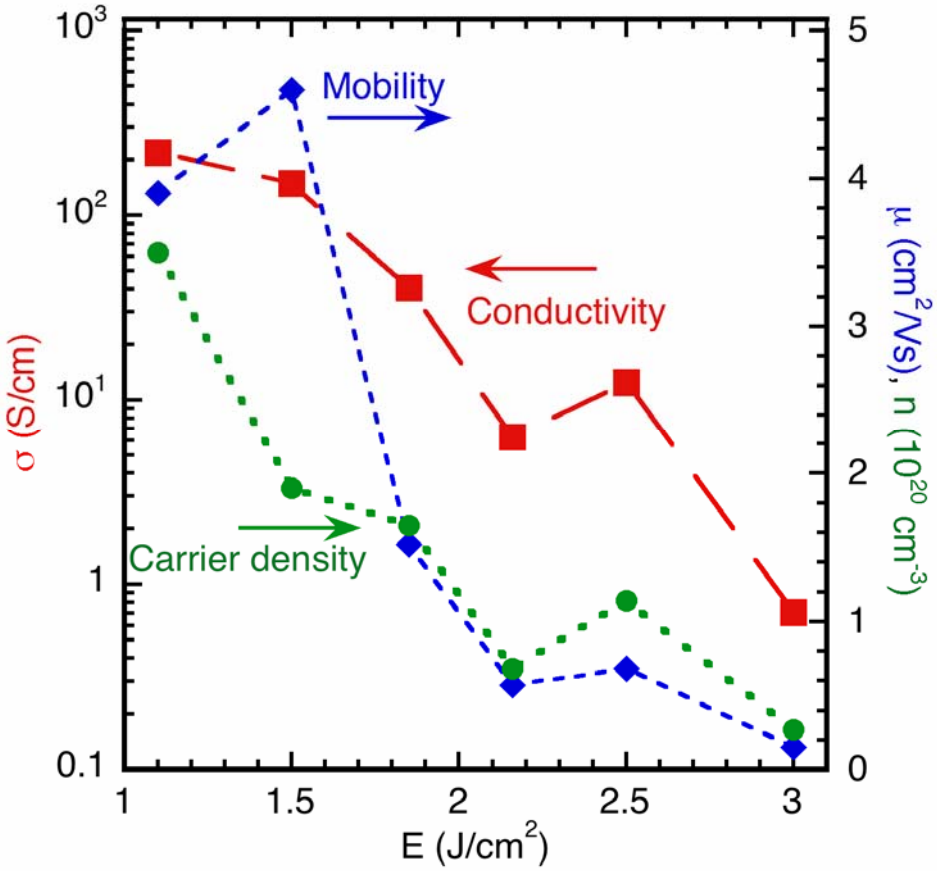

Figure 6.1. Electrical properties of room-temperature-deposited ZIO films strongly depend on the laser fluence E, with notably higher conductivity at low laser energy densities. No deposition gas is used.

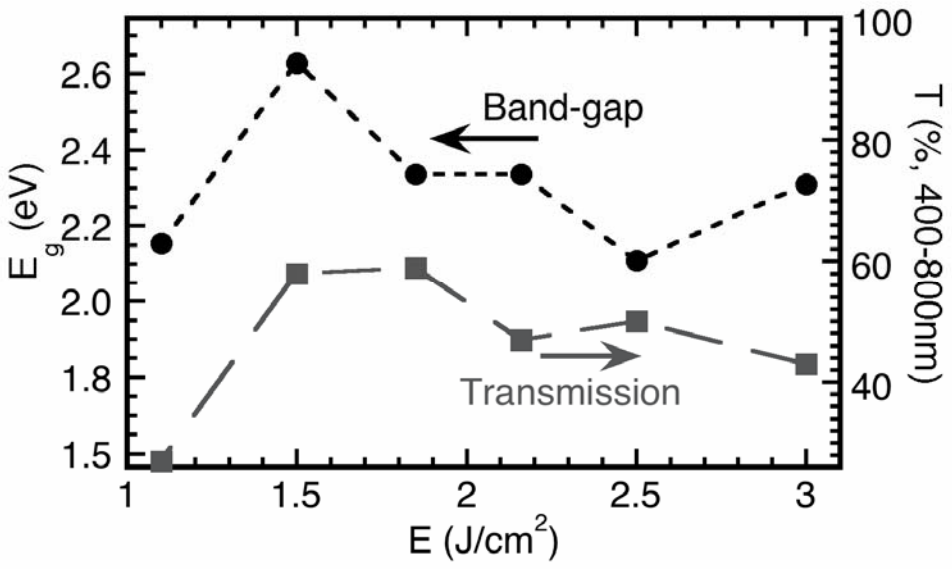

Figure 6.2. Average transmission and optical band gap energy of room-temperature-deposited ZIO thin films deposited at various laser energy densities.

energy axis. There is no clear trend between the band gap energy and the laser fluence. The average band gap value of 2.3 eV obtained for this series of ZIO thin films is somewhat lower than the 2.9 eV value reported in literature [4]. The highest band gap of 2.67 eV occurs for the ZIO film deposited at 1.5 J/cm^2 laser density, possibly associated with good transfer of target stoichiometry. All amorphous thin films have a brownish color, due to small band gaps and low average transmission. An absorption feature below the band gap also contributes to the thin film coloration (see Fig. 6.7). The variation of electrical and optical properties with laser fluence can originate from varying Zn/In ratios in the films. Another hypothesis is that passive defects such as oxygen vacancies, unreacted atoms/complexes, and voids that are carrier traps exist in the films and degrade the electrical conduction. All these species are likely to form during PLD deposition [15] particularly under UHV at low substrate temperature conditions, due to high energy of the plasma particles at

substrate surface and the deposition rate (typically 20 nm/min). The energetic species (~40 eV) bombarding the surface can cause bond-breaking leading to escape of oxygen atoms. A high deposition rate can also lead to burying of physisorbed species, without forming bonds to the bulk of the film, owing to low surface diffusion. Voids are less likely to form in PLD films, because rearrangement of surface atoms occurs by means of the dissipated energy of the arriving atoms. A larger number of such defects could be the reason for lower transmission in Fig. 6.2.

Based on above results summarized in Fig. 6.1 and Fig. 6.2, we find an optimum laser fluence of 1.5 J/cm^2 at the set 5 cm substrate target distance for amorphous $Zn_2In_2O_5$ thin film deposition at room temperature. These deposition parameters give the highest mobility and lowest optical absorption, but these values are not good enough for a commercially competitive TCO.

The target-substrate distance and laser pulse repetition rate are also important parameters. Table 6.1 shows that films deposited in UHV at room temperature and 1.5 J/cm^2 laser fluence show an increase in conductivity of almost a factor of 2 when the target-substrate distance increases from 3.75 cm to 7.5 cm. This is due to both carrier concentration and mobility enhancement. A lower laser pulse repetition rate also slightly enhances the electrical properties. In both cases, the improvement in electrical conductivity can be tied to the lower deposition rate, allowing more time for surface atoms to diffuse and yielding denser films.

Optimized room temperature deposition of ZIO films produces amorphous films with smooth surfaces but with relatively low conductivity and high absorption –

properties not desired of a good TCO. Optimization of other deposition parameters, such as substrate temperature and deposition gas ambient, is thus required.

Table 6.1. Amorphous ZIO thin film data deposited at room temperature at 1.5 J/cm^2 fluence and various target-substrate distances and laser repetition rates.

Target-substr. distance, cm	Repetition rate, Hz	Conductivity S/cm	Mobility cm^2/Vs	Carrier Dens. x10^{20} cm^{-3}	Deposition rate, nm/min
3.75	10	130	3.5	2.27	22
5	10	150	4.6	1.9	20
7.5	10	230	4.85	2.93	6
5	5	190	4.8	2.55	7

6.3.2. $Zn_2In_2O_5$ on heated substrates

Crystallization of $Zn_2In_2O_5$ films takes place by heating the substrate. Thin films are deposited in ~10^{-8} Torr vacuum (UHV) at substrate temperatures up to 400˚C, 1.5 J/cm^2 laser fluence, 5 cm target-substrate distance and 10 Hz pulse repetition rate. The X-ray diffraction patterns of selected ZIO films deposited at elevated temperatures are shown in Fig. 6.3. Use of 100˚C substrate temperature results in a completely amorphous film, with a surface roughness of 0.4 nm (Fig. 6.4a), close to that measured for films deposited at room temperature. At 200˚C, we find a broad diffraction peak around 30˚ in Fig. 6.3 is characteristic of XRD spectra of materials composed of very small particles and/or a large range of *d*-lattice spacings. A possible explanation of these results is the crystallite nucleation of $Zn_2In_2O_5$, which has been reported to be single-phase and stable at room temperature

only in thin film form [3,6,2]. AFM images on this film (Fig. 6.4b) clearly show that few-hundred-nanometer-sized grains are present in an otherwise amorphous matrix. As seen in Fig. 6.3, the observed XRD peak near 30˚ is very broad, contrary to the expected narrow peak width from the 400 – 500 nm size crystallites (Fig. 6.4b). The presence of a wide range of *d* lattice-spacings due to varying Zn/In ratio in the crystallites may be responsible for the broadening. The average surface roughness of this film substantially increases to 11 nm due to the large crystallites, but the matrix in-between is still smooth (RMS ~ 0.6 nm), characteristic of amorphous films.

The intensity of the $Zn_2In_2O_5$ XRD peak further increases for the 250˚C – 350˚C deposited films. Surface imaging of these films reveals 25 – 40 nm sized grains (Fig. 6.4c) and low 0.8 nm surface RMS roughness, indicating smooth crystalline surfaces.

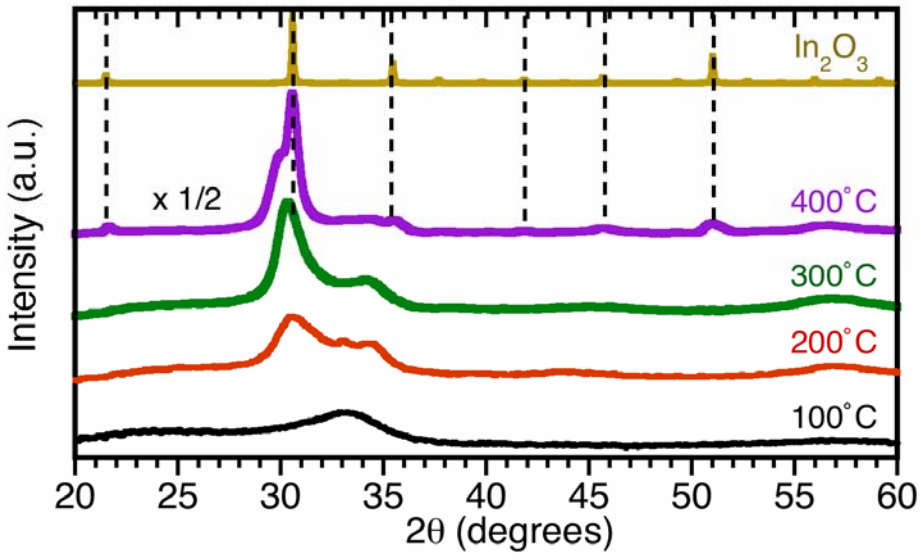

Figure 6.3. XRD patters of ZIO thin films deposited at various substrate temperatures in ultra high vacuum. The diffraction pattern of In_2O_3 is also shown for reference.

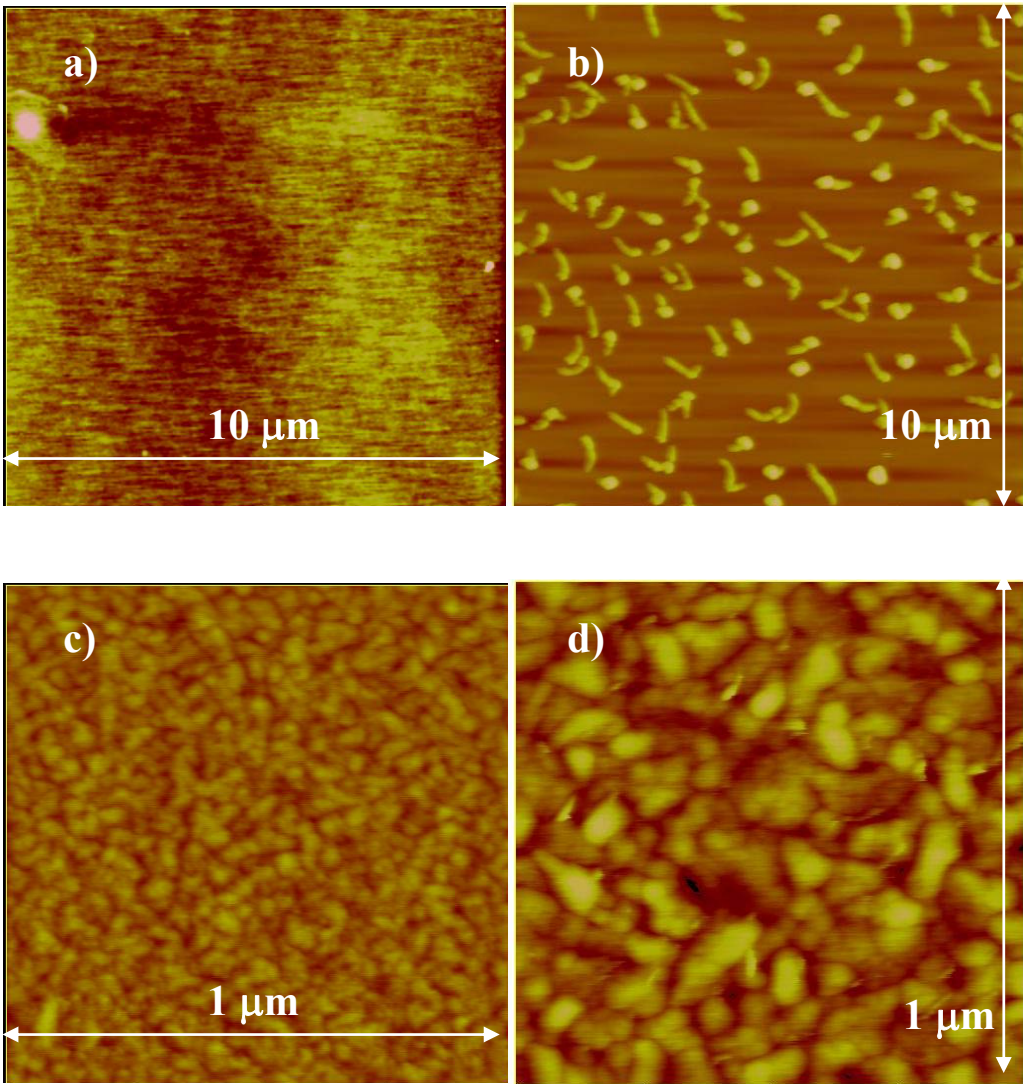

Figure 6.4. AFM images of amorphous (a), mixed crystalline-amorphous (b), nano-crystalline (c) and multi-phase polycrystalline (d) thin films from a $Zn_2In_2O_5$ target.

We find that single-phase, crystalline $Zn_2In_2O_5$ (c-ZIO) films are formed only in the 250˚C – 350˚C substrate temperature range. At 400˚C, multi-phase polycrystalline thin film growth occurs. Broad $Zn_2In_2O_5$ and sharp In_2O_3 XRD peaks are observed, as seen in Fig. 6.3. Variation of deposition parameters (laser fluence, target-substrate distance, deposition gas) does not yield single-phase ZIO at 400˚C substrate temperature. It is thus concluded, that phase pure $Zn_2In_2O_5$ films can be

obtained only at deposition temperatures up to 350˚C. This finding is in agreement with the reports of T. Minami *et al.* [3,4], but the authors did not investigate deposition temperatures above 350˚C. C. Marcel *et al.* [16] reports on ZIO films deposited at 500˚C, but evidence of phase purity is not presented.

The electrical properties of ZIO films deposited at various substrate temperatures are shown in Fig. 6.5. The conductivity of the amorphous phase reaches 480 S/cm at 100˚C substrate temperature, which is 3 times higher than the value measured for the room temperature deposited films. The increase of carrier concentration and mobility may be a result of producing electro-active oxygen vacancies (V_O) at elevated substrate temperatures, instead of passive ones in room temperature deposited films. Improvement in film structure by densification is also expected.

Deposition at substrate temperatures between 200˚C (onset of crystallization) and 350˚C results in crystalline films of the $Zn_2In_2O_5$ phase, as discussed above. The 100 – 150 nm films have similar conductivities around 1300 - 1600 S/cm in this deposition temperature range (compare to 7500 S/cm of crystalline ITO). The conductivity of the c-ZIO is higher than that of the amorphous phase of presumably the same Zn:In stoichiometry. A similar trend is found for amorphous-crystalline transition in In_2O_3 thin films [12]. The carrier mobility improves up to ~14 cm^2/Vs, which is somewhat lower compared to values found in the literature (~ 30 cm^2/Vs) [3,8]. Carrier densities of 5 – 7 x 10^{20} cm^{-3} are typical.

The optical properties of the ZIO thin films are summarized in Fig. 6.6. The band gap of the room temperature deposited ZIO film is 2.67 eV, as stated in the

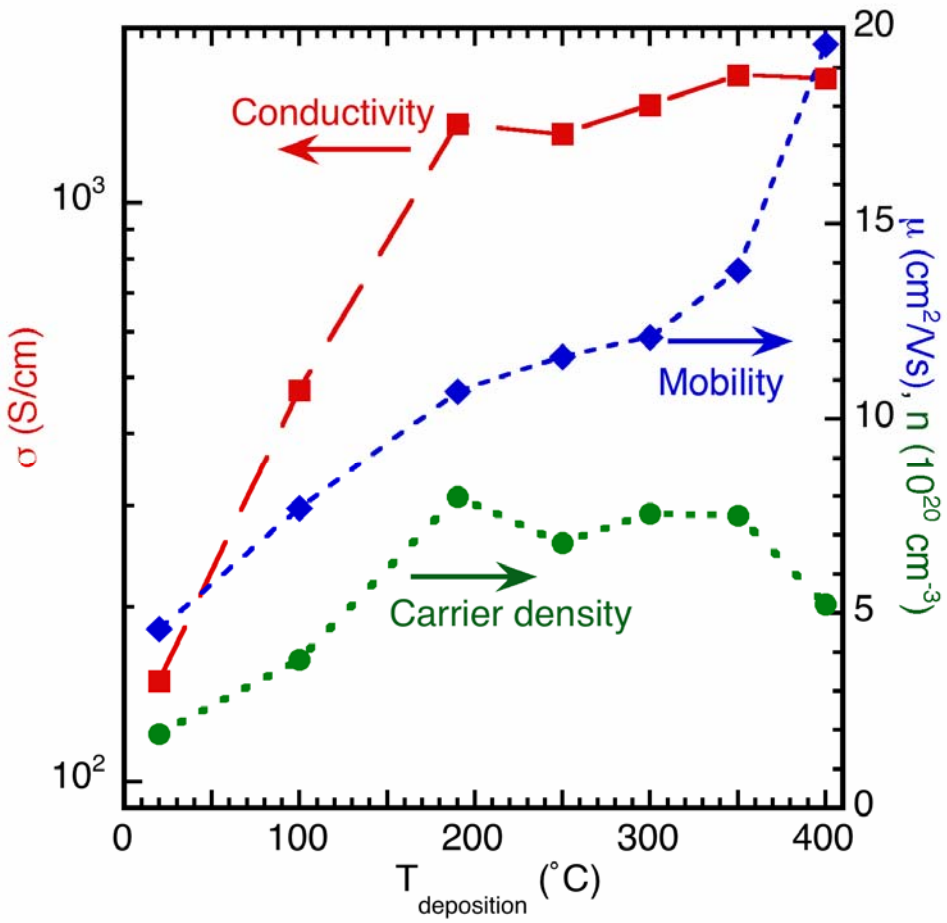

Figure 6.5. Electrical properties of nominally $Zn_2In_2O_5$ thin films with increase of deposition temperature from 20˚C to 400˚C.

previous section. Increasing the deposition temperature to 100˚C results in lower absorption and a 2.95 eV band gap. This has a net effect of improving the transparency (average 68% for a 120 nm thick film) in a wider range of the visible spectrum of the amorphous film. The 200˚C deposited film is comprised of crystalline and amorphous ZIO and produces intermediate optical properties: the absorption is similar to that of amorphous ZIO films, but the wider band gap is characteristic of the crystalline phase.

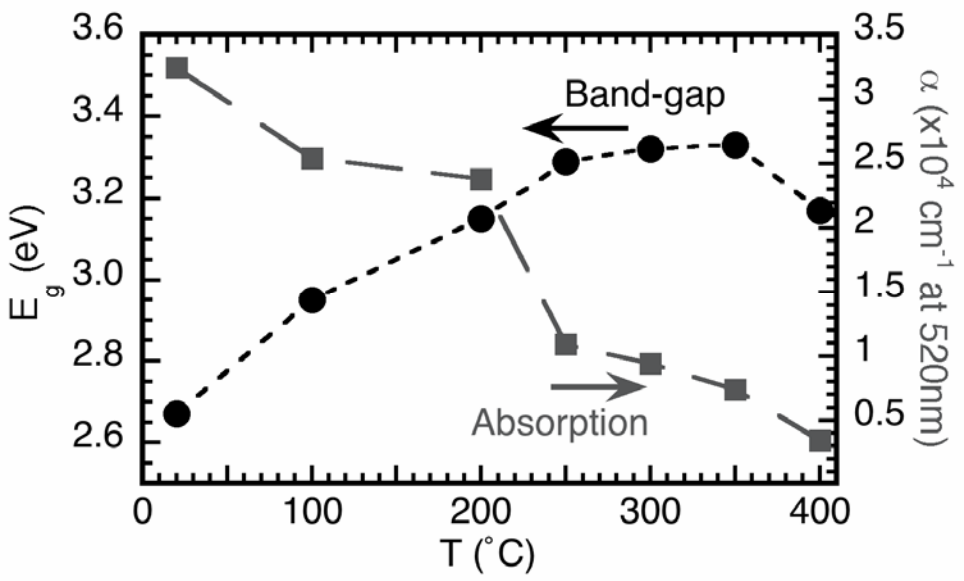

Figure 6.6. Optical band gap (circles) and absorption coefficient (squares) of ZIO films at elevated substrate temperatures. Absorption coefficients are evaluated at 520 nm.

Crystalline $Zn_2In_2O_5$ films deposited at 250˚C – 350˚C are far superior to their amorphous counterparts. First of all, a sharp drop in the absorption occurs when fully crystallized films are made full crystallization of the films. The 3.3 eV band gaps of the c-ZIO films are determined to be indirect (Fig. 6.7). These films are clear due to the low absorption and high band gap, as shown in Fig. 6.6 and Fig. 6.7. We assign the band gap widening observed in the amorphous and crystalline films to the Burstein-Moss shift [17,18], according to which an increase of carrier concentration blue-shifts the onset of transmission. Our measured band gap values lie between the reported optical gaps of $Zn_2In_2O_5$ of 2.9 eV [4] and 3.5 eV [6].

The transmission and reflection spectra of a 150 nm thick $Zn_2In_2O_5$ film deposited at 300˚C are shown on the inset of Fig. 6.7. An average transparency of over 77% in the visible range is typical for UHV deposited c-ZIO thin films.

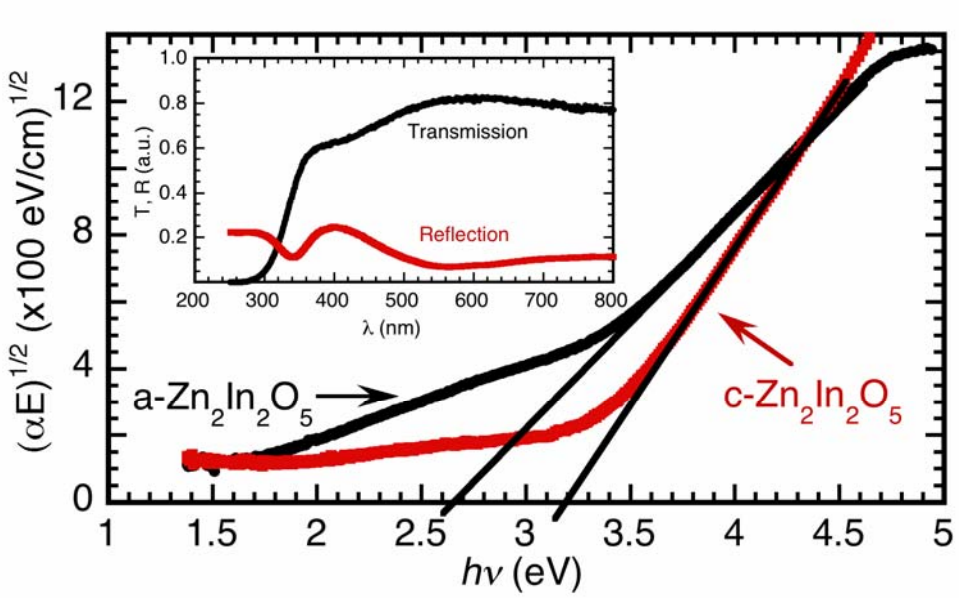

Figure 6.7. Indirect band gap evaluation of amorphous ZIO film deposited at room temperature (black) and c-$Zn_2In_2O_5$ film at 300˚C (red). The inset shows the transmission and reflection spectra of the same c-$Zn_2In_2O_5$ film.

This transparency translates into an absorption coefficient of 9 x 10^3 cm^{-1}. For comparison, the 180 nm thick commercial ITO has a higher average transparency of 85% in the visible range and thus lower absorption coefficient of 1.5 x 10^3 cm^{-1}.

Further increasing the deposition temperature to 400˚C results in the phase separation into $Zn_2In_2O_5$ and In_2O_3 (Fig. 6.3 and Fig 6.4d). The carrier mobility is somewhat higher in this film, most likely due to the presence of crystalline In_2O_3. We expect films deposited at even higher temperatures also to be phase separated.

To conclude, $Zn_2In_2O_5$ thin films deposited in UHV at substrate temperatures 250˚C – 350˚C are crystalline, and partially or fully amorphous below that. c-ZIO films exhibit conductivities up to 1600 S/cm and mobility of 14 S/cm. Optical transparency and conductivity of a-ZIO are lower then of the c-ZIO counterparts.

6.3.3. Influence of deposition gas

In the following, thin films of $Zn_2In_2O_5$ are deposited at 350˚C in 10^{-3} and 10^{-2} Torr total gas pressure of pure Ar, Ar – 20% O_2 (Ar/O_2) and pure O_2 deposition gases. For optimal film deposition in the gas ambient, a laser fluence of 1 J/cm^2 is used in all cases. Films deposited at 350˚C using the higher 1.5 J/cm^2 fluence and 10^{-3} Torr chamber pressure show In_2O_3 peaks, indicating Zn deficiency in the films.

Improved structural properties are expected in films prepared using deposition background gas pressure. Collisions with gas molecules reduces the energy of particles in the plume is decreased by upon arrival to the substrate. This causes less re-sputtering at the substrate surface and consequently less bond breaking (molecular dissociation), thus enhancing grain growth and crystalline lattice structure of the growing films [15]. In case of deposition in oxygen rich ambient, incorporation of atoms from the gas also takes place, due to dissociation of O_2 (g) molecules by the energetic ions of the plume. These $½O_2$ anions readily react with the film surface and get incorporated into the growing film.

Indeed, XRD patterns of $Zn_2In_2O_5$ films deposited at various oxygen partial pressures, presented in Fig. 6.8, show improved crystal quality compared to UHV deposited films. The better lattice structure is manifested in narrower diffraction peaks. A peak shift towards higher 2θ angles is seen with increasing O_2 partial pressure, indicating a decrease in the unit cell volume. Such a volume decrease during deposition in O_2 (g) could be due to the filling of oxygen vacancies relieving strain in the crystal lattice. The XRD pattern of the 10^{-2} Torr O_2 deposited film is in

good agreement with $Zn_2In_2O_5$ reference peaks [JCPDS #20-1442]. The increasing intensity and narrowness of all reflection in Fig. 6.8 (glancing incidence geometry) points to an improved crystallinity of O_2 (g) deposited films, and observation of mainly (00*l*) diffraction peaks in the θ - 2θ geometry, shown in Fig. 6.9, indicates that in fact ZIO films grow primarily *c*-axis oriented in the presence of deposition gas on fused SiO_2 substrates.

The RMS surface roughness of the films vary between 0.8 – 3 nm over a 100 μm^2 area, with low values for the UHV and 10^{-2} Torr O_2 deposited films. The higher RMS roughness is a result of larger polycrystalline grains. The low roughness of films deposited in UHV and O_2 (g) at 10^{-2} Torr pressure occur for different reasons. In the former case, the small crystallite sizes, and the textured crystalline lattice in the latter case produce the smooth surfaces.

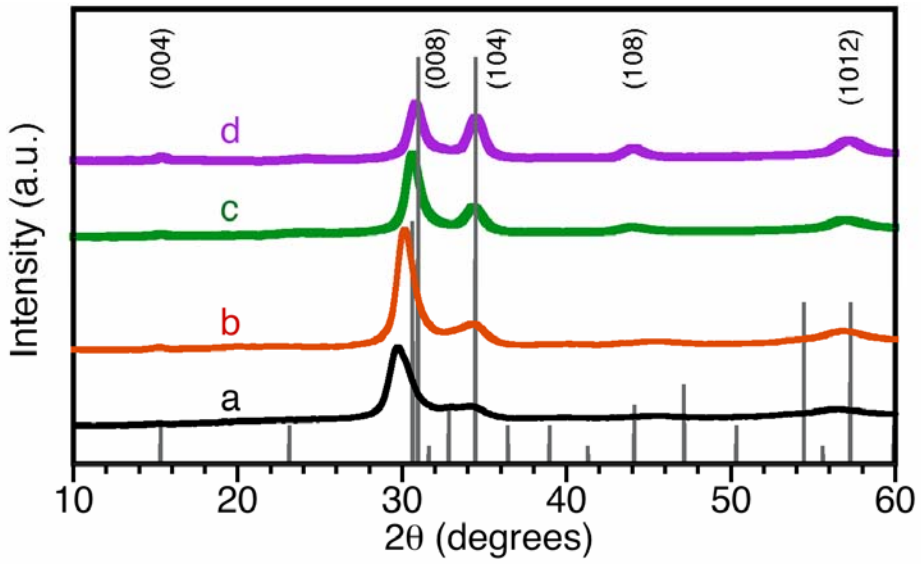

Figure 6.8. XRD patterns of ZIO films grown at 350˚C and (a) UHV, (b) 10^{-3} Torr Ar/O_2, (c) 10^{-3} Torr O_2 and (c) 10^{-2} Torr O_2 deposition gas pressure. The vertical lines are the $Zn_2In_2O_5$ reference pattern and reflection peaks observed in the films are indexed at the top of the graph. Glancing incidence geometry and an area detector are used to obtain these diffractograms.

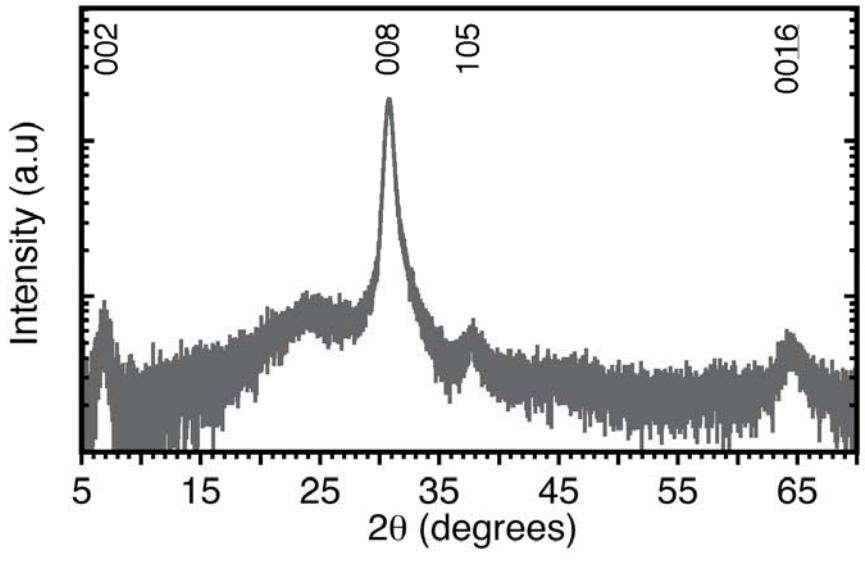

Figure 6.9. XRD pattern of $Zn_2In_2O_5$ film deposition parameters 350˚C and 10^{-2} Torr O_2, in the θ - 2θ configuration. The broad background is due to the SiO_2 substrate.

The introduction of deposition gas enhances the electrical and optical properties of the ZIO thin films, as shown in Fig. 6.10. Deposition in pure Ar (g) produces the highest measured conductivity of 1920 S/cm amongst c-ZIO. The high conductivity is the product of a carrier mobility of 17 cm^2/Vs and carrier concentration 7 x 10^{20} cm^{-3}. These values are very close to those of UHV deposited films at 350˚C. Thus introduction of a 10^{-3} Torr inert gas pressure only slightly improves the mobility and increases carrier concentration.

The electron mobility increases with higher O_2 (g) pressures used in the deposition due to lower scattering of carriers on oxygen vacancies. It reaches a maximum at 28 cm^2/Vs (Fig. 6.10), comparable to values reported in literature [8]. Although high mobility is achieved, the overall conductivity decreases to 660 S/cm due to the lower carrier concentration of O_2 ambient deposited films. Such a trend is commonly observed in *n*-type oxides with better oxygen stoichiometry.

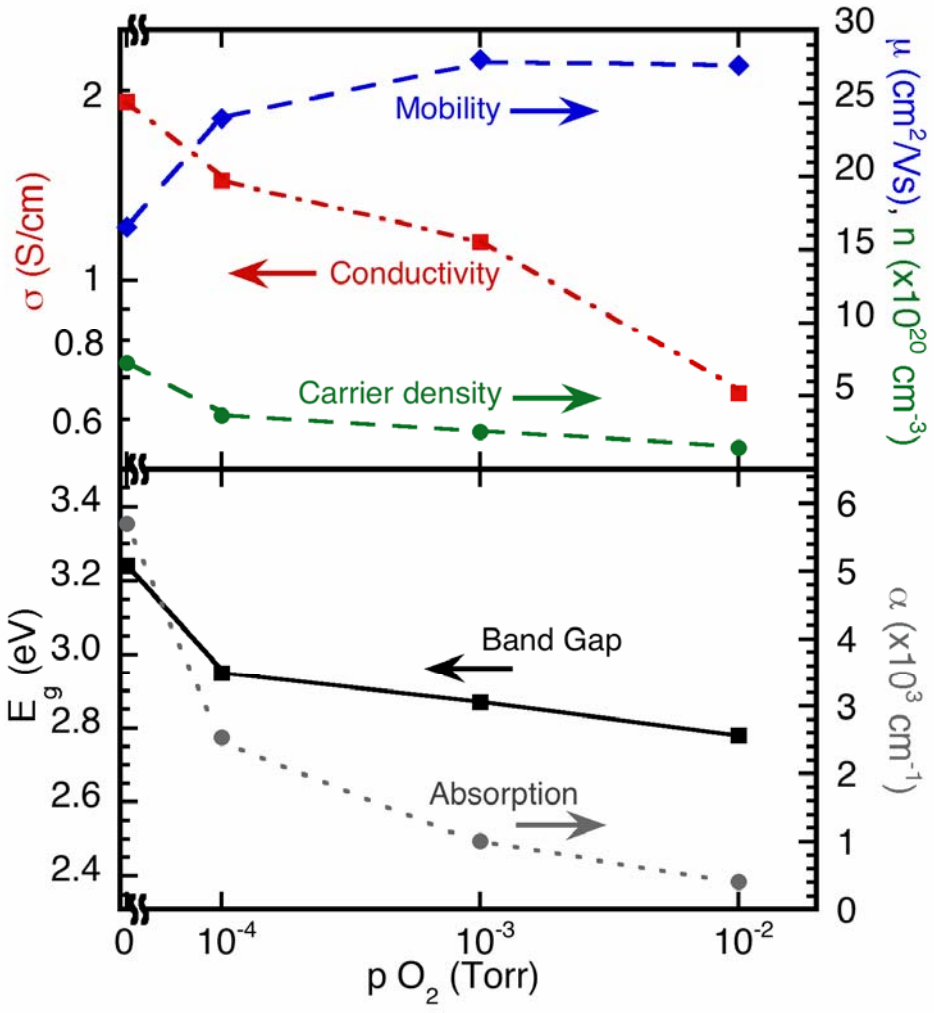

Figure 6.10. Electrical (conductivity, mobility and carrier concentration) and optical (band gap and absorption) properties of ZIO films deposited at various O_2 partial pressures and 350˚C substrate temperature. Pure Ar (g) is used at the zero point.

The average transparency of these ZIO films is about 80% in the visible (400 – 800 nm) wavelength range, due to the film thickness variation between 160 – 220 nm. The indirect band gap narrows from 3.24 eV to 2.78 eV with increasing O_2 (g) pressure. Once again, the decrease in band gap is consistent with the decrease of the carrier concentration (Fig. 6.10). The absorption coefficient (evaluated at 520 nm photon wavelength) decreases below 1000 cm^{-1}, considerably lower compared to pure

Ar (g) deposited films (about 6000 cm^{-1}). We find that low absorption and high conductivity does not coexist in c-ZIO films.

The wavelength dependence of the absorption coefficient of ZIO films deposited at various O_2 (g) partial pressures are shown in Fig. 6.11. An order of magnitude decrease of the absorption in the visible range is observed, when pure O_2 (g) is used. The decrease in absorption implies that oxygen vacancies are strong absorption centers in ZIO thin films, throughout the visible spectrum.

The Burstein-Moss shift can be followed at the onset of absorption in Fig. 6.11. The decreasing band gap results in a yellow tinge, of the otherwise clear films. Transmission and reflection spectra of selected films are shown in Fig. 6.12, corresponding to the measured absorption values in the UV – near IR spectral region.

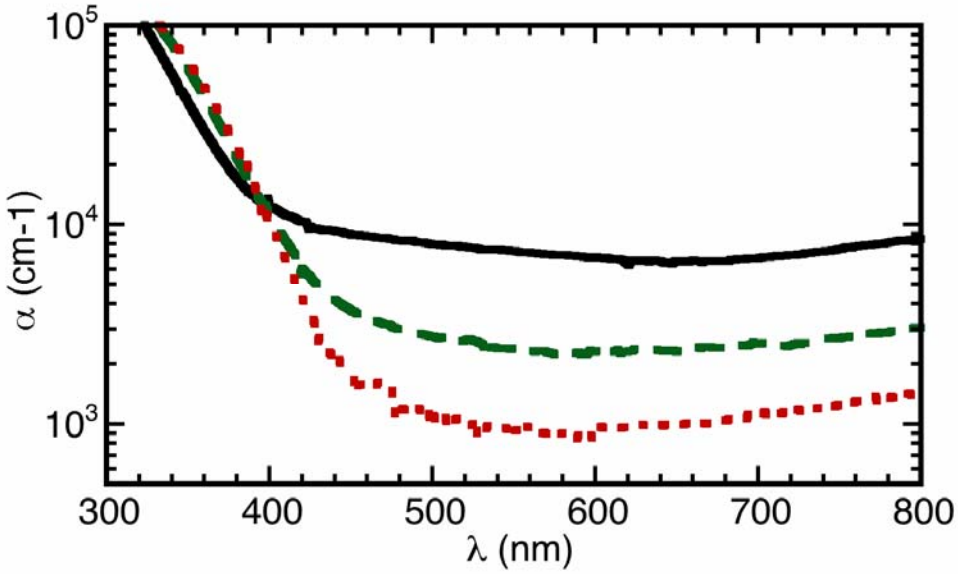

Figure 6.11. Absorption coefficient of ZIO thin films deposited in 10^{-3} Torr Ar (solid line), Ar – 20% O_2 (dashed line) and O_2 (dotted line) gasses.

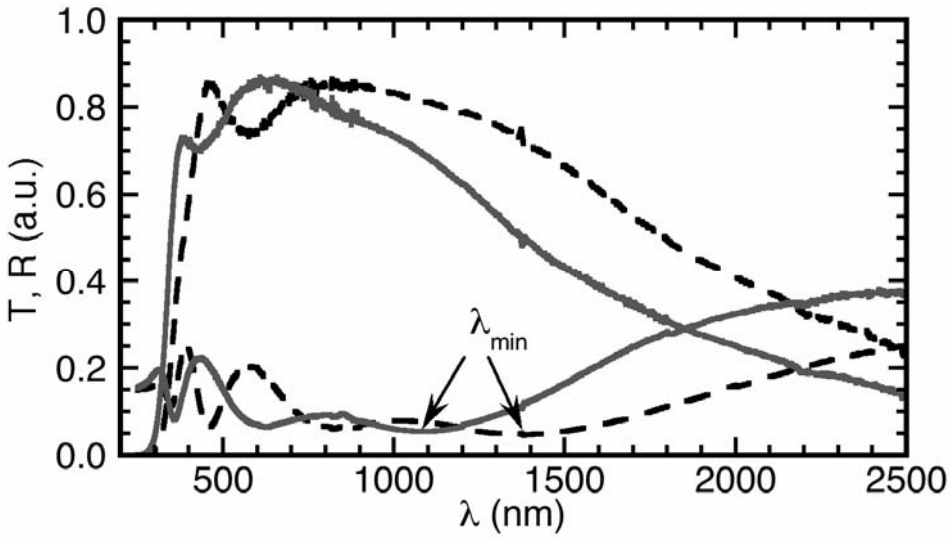

Figure 6.12. Transmission and reflection spectra of ZIO films deposited in 1 mTorr Ar (g) (solid lines) and Ar – 20% O_2 (dashed lines).

ZIO films are prepared at the same deposition parameters, except varying the O_2 (g) partial pressure in the chamber between 2 x 10^{-4} and1 x 10^{-2} Torr. Therefore the observed reduction of carrier concentration is exclusively due to reduction of donor vacancies by oxygen incorporation in the films. The band gap also decreases with the higher oxygen partial pressure. The variation of band gap ΔE with carrier concentration n is described by the Burstein-Moss shift [20]:

$$\Delta E_g^{BM} = \frac{\hbar^2}{2m^*}(3\pi^2 n)^{2/3} \tag{6.1}$$

where m^* is the reduced effective mass. Plotting the band gap *vs*. $n^{2/3}$, as shown in Fig. 6.13, results in a linear dependence, indicating similar effective mass in all films. The effective mass calculated from the slope equals to 0.5 m_0. A similar red-shift of the band edge is observed in [4], but the carrier effective mass is not reported.

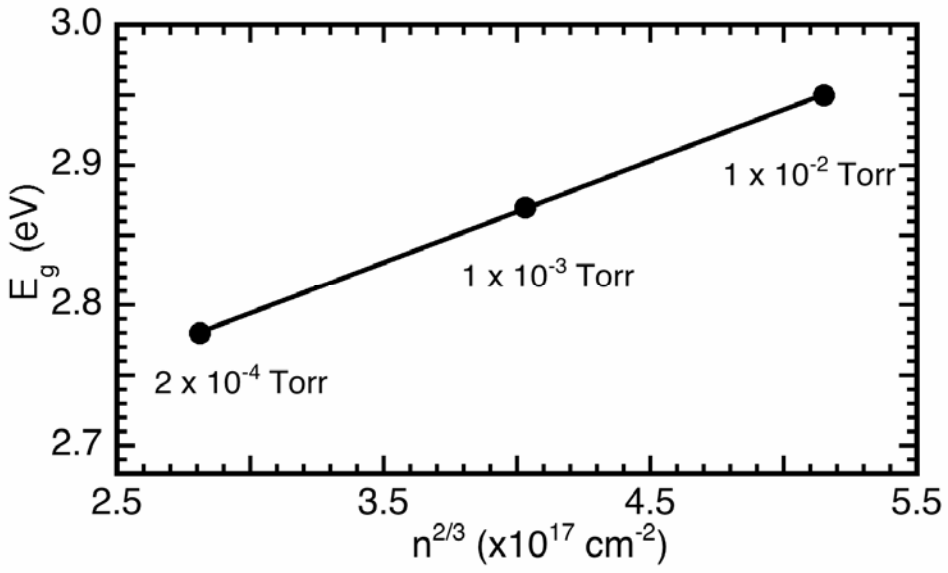

Figure 6.13. The band gap varies linearly with 2/3 power of the carrier concentration in ZIO films deposited at 350˚C and various O_2 (g) partial pressures. Number labels represent the O_2 pressure in chamber during film deposition.

Carrier effective masses of 0.2 – 0.3 m_0 reported in the literature [6,16] are lower than our estimate of 0.5 m_0. We will now also employ a similar method used in Ref [16] to find effective mass involving the calculation of the plasma wavelength λ_p. $Zn_2In_2O_5$ films deposited at 0 and 10^{-4} Torr O_2 partial pressures exhibit a crossover of the transmission and reflection spectra in the near-infrared spectral region at 1700 – 2000 nm, as shown in Fig. 6.12. To calculate the plasma wavelength the following equation is employed [19]:

$$\lambda_p = \lambda_{\min}\sqrt{n^2/\left(n^2-1\right)}$$

where λ_{min} is the last reflection minimum before the transmission and reflection lines cross on the long wavelength side (see Fig. 6.12) and n is the refractive index. A minimum in reflectivity R_{min} can be observed (and n ~ 1) just before the plasma edge in this approximation (or empirical observation) of Ref [19], in case of low losses.

This R_{min} should not correspond to a thin film interference minimum and may also be observed in bulk samples. In fact, the fringe structure of a thin film is periodic in energy, and thus the nature of the last observed minimum in the reflection spectra can be verified. In this case λ_{min} does not belong to the fringe pattern of the thin film. The refractive index n varies from 1.6 for Ar (g), to 1.75 for Ar – 20% O_2 (g), and to 1.79 for pure O_2 (g) deposited films, evaluated at 1100 nm. These values are much lower than the previously estimated refractive index of 2.4 [4]. The dielectric constant is then calculated from the refractive index. The measured carrier concentrations and reflection minima λ_{min} of 10^{-3} Torr Ar, Ar – 20% O_2 and O_2 gas deposited ZIO films are used, respectively. Inserting these values into Eg. (3.3) (Chapter 3) results in electron effective masses of $m^* = 0.5$ for Ar (g), 0.31 for Ar – 20% O_2 (g) and 0.27 for O_2 (g) deposited ZIO films. The value of 0.5 m_0 is the same as determined above from the Moss-Burstein shift. The latter two values are closer to effective masses reported for In_2O_3 thin films with Sn- and W-doping [20,11]. Also, Marcel *et al*. [16] reports low effective masses for $Zn_2In_2O_5$ composition films deposited at 500˚C using PLD evaluated by the this method. According to results presented in this work, ZIO phase separates above 350˚C deposition temperature, resulting in primarily In_2O_3 phase films. We find that the plasma wavelengths calculated from λ_{min} does not correspond to respective absorption maxima (where the absorption $A = 1 - T - R$, with T and R being the transmission and reflection coefficients). Moreover, a variation of effective mass implies changes in the dispersion near the conduction band minimum, which seems implausible without varying the Zn/In ratio in the films.

The determination of the effective mass is more rigorous using the Burstein-Moss shift, because only two measurables, band gap and carrier concentration, are required. The 0.5 m_0 value is consistent throughout this work in amorphous and crystalline ZIO films, and believed to be characteristic to the $Zn_2In_2O_5$ composition thin films prepared by PLD.

Assuming that changes in at optical absorption edge take place only due Burstein-Moss effect the fundamental gap of intrinsic c-ZIO is calculated to be 2.6 eV. Therefore, decreasing the carrier concentration in crystalline ZIO to obtain semiconducting behavior would lead to a red-shift of the absorption edge far into the blue region of the visible spectrum. This feature makes ZIO unattractive for transparent channel material application in TTFTs.

To summarize, the use of a deposition gas enhances the properties of $Zn_2In_2O_5$ thin films. Films deposited in Ar (g) produce the highest conductivity of 1920 S/cm amongst crystalline films. Introduction of O_2 (g) during deposition increases electron mobility and reduces the carrier concentration. Low absorption is achieved in the visible optical range, but the absorption edge red-shifts below 3 eV, when O_2 (g) is used. Thus reducing the absorption in ZIO films is accompanied by a reduction in conductivity. This issue may be resolved by substitutional doping. Carrier effective mass of 0.5 m_0 is calculated for crystalline ZIO thin films.

6.3.4. $Zn_2In_2O_5$ growth in O_2 gas

In the previous section $Zn_2In_2O_5$ thin films are deposited at various O_2 (g) gas pressures and 350˚C substrate temperature. These films grow *c*-axis oriented, and have moderate conductivity and low absorption in the visible spectrum, compared to films deposited in UHV or 10^{-3} Torr Ar (g). In this section, we extend the investigation of such films to study the combined effect of substrate temperature and O_2 deposition gas. Moreover, industrial applications favor low or room temperature preparation of TCO films due to lower cost and possibility of deposition onto flexible substrates.

ZIO thin films are crystalline in the 200 – 350˚C deposition temperature range in 10^{-3} Torr O_2 (g) ambient. The use of oxygen induces grain growth and results in an average RMS roughness of about 3 nm. Films deposited at 100˚C and room temperature are amorphous verified by XRD and absence of crystallites on AFM surface images. The surface roughness of these a-ZIO films decreases to ~0.7 nm.

The change in conductivity, carrier concentration and mobility with deposition temperature is shown in Fig. 6.14. We find that the electrical properties of ZIO thin films are enhanced with decreasing substrate temperature. The carrier mobility is 25 – 29 cm^2/Vs for the crystalline films above 200˚C, and increases to about 40 cm^2/Vs in the amorphous region below 100˚C. The maximum conductivity of amorphous film is 2030 S/cm, similar to that achieved for crystalline ZIO deposited in Ar (g) at 350˚C, where the high conductivity resulted from a high carrier density. Room temperature deposited ZIO films exhibit some variation in electrical properties,

described below, but representative values of conductivity, mobility and carrier concentration are shown in Fig. 6.14.

The conductivity of the room temperature deposited films varies between 1400 – 1800 S/cm. The carrier concentration and mobility are responsible for the conductivity changes in the investigated film thickness range of 100 – 320 nm. We find that thinner films have lower carrier mobility and higher carrier concentration, and *vice versa* in thicker films. This can be associated with higher levels of oxygen vacancies at the initial stages of film growth, generating a higher carrier concentration. As the film thickness increases, the oxygen stoichiometry improves and causes less impurity scattering. A similar dependence of electrical conductivity on film thickness is reported [9] in ZIO films deposited by sputtering, but an opposite trend between the carrier concentration and mobility is observed.

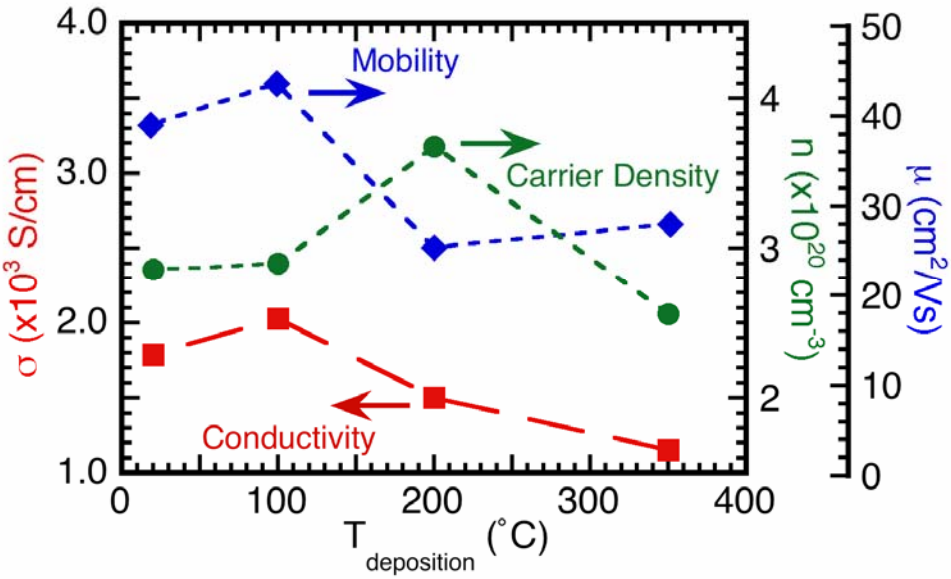

Figure 6.14. Conductivity, mobility and carrier concentration of ZIO films deposited in 10^{-3} Torr O_2 (g) at various substrate temperatures.

The higher conductivities of the amorphous ZIO films arise from an increase in carrier mobility. Such an enhancement can be associated with the absence of grain boundaries, which are scattering sites in the crystalline films. Indium oxide based TCO's are found to possess high electron mobility [1] due to a high dispersion of electronic states at the bottom conduction band [21]. Amorphous $Zn_2In_2O_5$ can be classified as a heavy metal cation double oxide [22,23], where high mobility is expected due to an overlap of atomic orbitals to form a conduction band. Thus a high mobility of 40 cm^2/Vs in amorphous $Zn_2In_2O_5$ is expected. In fact, even higher electron mobility of 50 cm^2/Vs is recently achieved [24] for room temperature deposited films near $Zn_2In_2O_5$ composition by the rf cosputtering method.

The optical band gap and absorption coefficient of crystalline (200˚C and above) and amorphous ZIO films prepared in O_2 (g) are shown in Fig. 6.15. The absorption varies little around 1000 cm^{-1} with the deposition temperature. The band gap of the films closely follows changes in the carrier concentration. It is worth noting that a carrier concentration of 2.9 x 10^{20} cm^{-3} in the amorphous films (below 100˚C) results in a 2.82 eV band gap. This optical gap is lower than 2.88 eV of a crystalline film of a lower 2.6 x 10^{20} cm^{-3} carrier concentration. Smearing of the band edge is typical in amorphous materials and may cause the lower band gap. We thus find that intrinsic a-ZIO would have a 2.5 eV band gap, which is 0.1 eV lower than that of intrinsic c-ZIO (using equation (6.1) for Burstein-Moss shift and the estimated effective mass of 0.5 m_0).

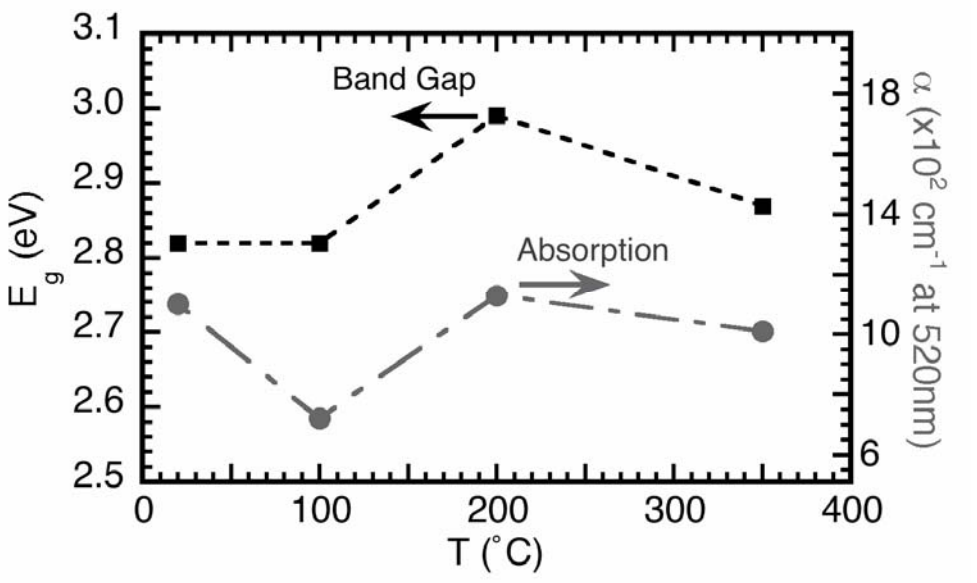

Figure 6.15. Optical band gap and absorption coefficient (at 520 nm wavelength) of ZIO films deposited in 10^{-3} Torr O_2 at various substrate temperatures.

The lower absorption in a- and c-ZIO films compares favorably to the 1600 cm^{-1} measured for commercial ITO. Yet the conductivity of 7500 S/cm is almost 4 times of that measured in any ZIO films prepared in this work. Because the mobilities in both materials are the same, the difference lies in the effective carrier generation up to 10^{21} cm^{-3} achieved by substitutional doping of Sn into In_2O_3. An attempt of donor doping ZIO with W is described below in section 6.3.6.

The electrical and optical performance of amorphous and crystalline ZIO films produced by PLD is similar to the results previously reported. In Ref. [4] rf magnetron sputtering in Ar gas is employed to obtain the highest conductivity (2500 S/cm) films. Our results compare well with the novel In_2O_3 – 10 wt.% ZnO TCO [14], with a high temperature stability of the amorphous phase [25], discussed for a-ZIO in the next section. The conductivity of amorphous ZIO surpasses that of amorphous In_2O_3 and ITO films [1].

A comparison of carrier concentration, mobility and absorption of a-ZIO films deposited in UHV and 10^{-3} Torr Ar and O_2 (g) at room temperature is shown in Fig. 6.16. The low 150 S/cm conductivity of the UHV deposited film increases to 800 S/cm when Ar (g) is used. This higher conductivity arises from an increase of carrier mobility to 13 cm^2/Vs and carrier density to 3.9 x 10^{20} cm^{-3}. Use of O_2 (g) further enhances the conductivity to 1750 S/cm, due to a high mobility of 38 cm^2/Vs, but a decrease in carrier concentration is also observed.

The use of a 10^{-3} Torr gas ambient during deposition enhances the carrier mobility in a-ZIO (Fig. 6.16). The use of Ar (g) reduces the re-sputtering of the growing film surface during deposition, possibly improving oxygen stoichiometry in the film. Deposition in O_2 (g) reduces the number of V_O, yielding even higher mobility. The high energetics of the plume in PLD enables dissociation of O_2

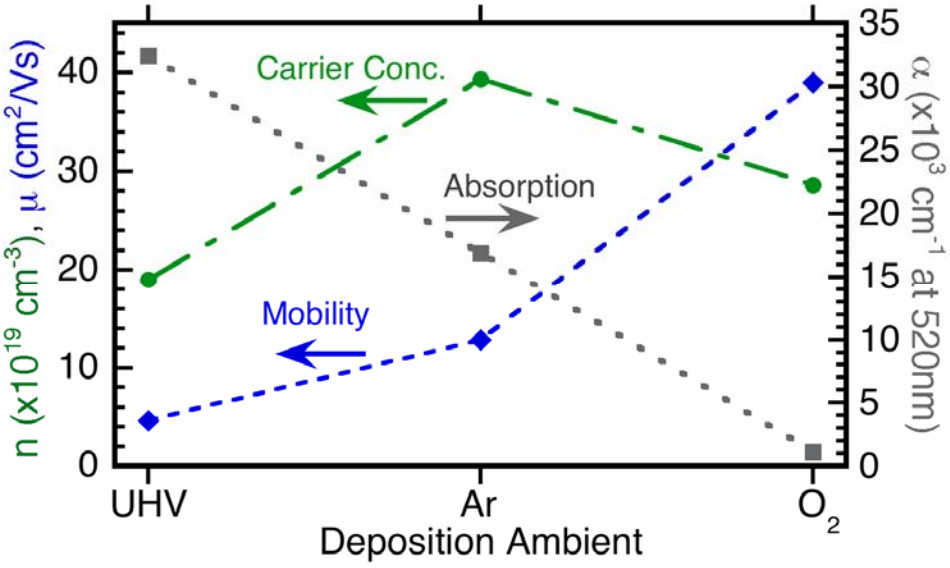

Figure 6.16. Properties of ZIO films prepared in various deposition gases at room temperature. When gas is used, a 10^{-3} Torr pressure is maintained during the deposition.

molecules of the deposition gas resulting in its effective incorporation into the film. This reduction in V_O can also be followed by the over an order of magnitude decrease of absorption in the visible range (Fig. 6.16) from 32000 cm^{-1} to 1000 cm^{-1}. It is evident that a-ZIO films deposited in O_2 (g) have by far superior properties then those prepared in UHV and Ar (g).

In summary, c-$Zn_2In_2O_5$ deposited in O_2 (g) at 350˚C results in lower conductivity compared to UHV and Ar (g) deposited crystalline films. In a-$Zn_2In_2O_5$ films the use of O_2 (g) produces high mobility of 40 cm^2/Vs and conductivity up to 2030 S/cm at low 100˚C substrate temperatures, desirable for flexible electronics technology. The a-ZIO films deposited in O_2 (g) have low absorption coefficients and band gap of 2.8 eV.

6.3.5. Post-deposition annealing in air

Temperature stability of electrical properties is a desirable feature of amorphous thin films. Amorphous $Zn_2In_2O_5$ is deposited at room temperature, 10^{-3} Torr O_2 (g) pressure and laser fluence of 1 J/cm^2, and post-annealed in air. The 190 nm ZIO sample used for the air annealing is blanket coated onto a 1 x 1 in^2 substrate. The film is then cleaved into several pieces and oven annealed at various temperatures in air. This rules out the possibility of physical property variation in films prepared even under identical deposition parameters.

Amorphous ZIO films are oven annealed for 40 min at temperatures up to 500˚C. The films are amorphous even after the 500˚C anneal, with only a typical

broad XRD reflection spanning over 5˚ in 2θ angles. The surface morphology of the film changes following a lower 300˚C annealing and is typical for films annealed at higher temperatures. The smooth amorphous surface of the as deposited film with RMS roughness of 0.7 nm becomes rougher (~1.5 nm) due to appearance of bubble-like particles. It is possible that these bubbles indicate crystallization of the film, but we do not see XRD reflections of c-ZIO or precipitation of other crystalline phases, like In_2O_3.

The high temperature stability of the amorphous phase in ZIO is comparable to that of In_2O_3 – 10 wt. % ZnO (IZO) thin films [14]. The high variability of electrical properties allows application of IZO as a transparent conductor [1] and thin film transistor channel layer [26]. Other amorphous TCO's such as In_2O_3 and ITO have much lower crystallization temperatures around 150 – 200˚C [12,25]. Higher annealing temperatures are not accessible in this work, due to the low softening temperature of the substrate.

Figure 6.17 depicts the electrical properties of the air-annealed films. The film conductivity increases from 1650 S/cm of the as deposited film to 1940 S/cm after a 300˚C air anneal. The conductivity decreases sharply at annealing temperatures above 400˚C. A decrease in carrier concentration and mobility decreases film conductivity to 8 S/cm after 500˚C annealing. The high 40 cm^2/Vs electron mobility of room temperature deposited film is maintained up to 400˚C annealing temperature.

Similar air annealing experiments are reported for amorphous IZO thin films [14,25]. The authors find that IZO films crystallize at 500˚C after ~2.5 h anneal in air, and the conductivity of the films decreases with higher annealing temperatures.

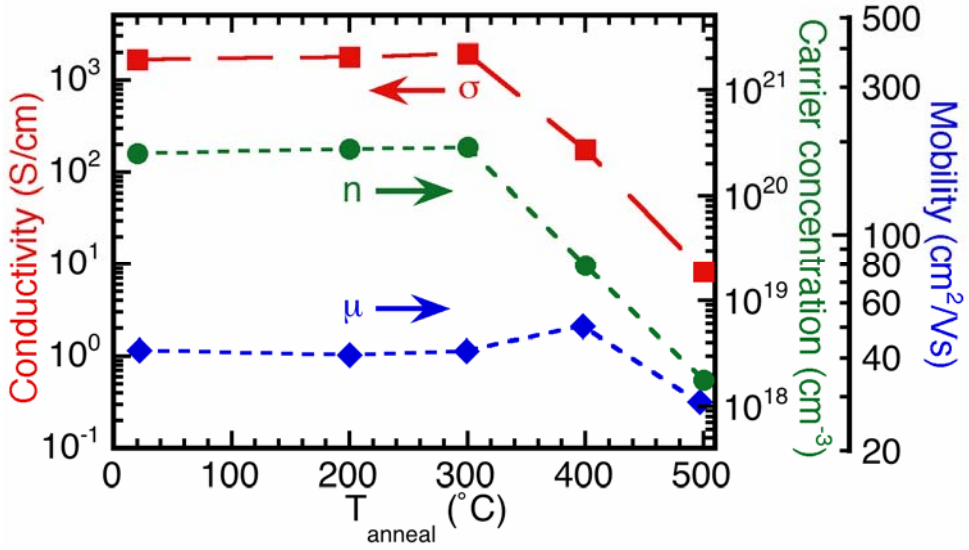

Figure 6.17. Conductivity of air annealed amorphous ZIO films as a function of annealing temperature.

In our case of a-$Zn_2In_2O_5$ air annealed films, a decrease in conductivity is also observed above 400˚C annealing temperatures. The carrier concentration also drops by orders of magnitude. Such changes can be the consequence of neutralization of electron donors such as filling of oxygen vacancies or oxidation of Zn interstitials, suggested in [14].

Air annealing results in a conductivity increase when temperatures up to 300˚C are used. This initial increase may be associated with the change in carrier concentration from 2.5 x 10^{20} cm^{-3} to 2.9 x 10^{20} cm^{-3}, because the mobility remains constant at 42 cm^2/Vs (less then 5% variation). Two possible explanations for this behavior are proposed. Upon heating some oxygen could be lost, creating more vacancies. Another possibility is the existence of previously mentioned neutral defect states in the room temperature films, which release electrons upon annealing. The

second possibility is more likely to take place due to the low annealing temperatures involved.

Figure 6.18 shows a linear dependence between the measured band gap and $n^{2/3}$ for as deposited and 300 – 400˚C air annealed films. An electron effective mass of 0.5 m_0 is calculated using the Burstein-Moss law. This carrier effective mass in amorphous ZIO films is the same as obtained in previous sections for crystalline films, thus a similar density of states and "band structure" governs the electron transport in both cases.

Annealing at 400˚C and 500˚C leads to appearance of a yellow color to the films due to the decrease of the band gap to 2.55 eV. The reduced absorption (at 520 nm) of 450 cm^{-1} for the 500˚C annealed film (compare to 1000 cm^{-1} for as deposited film) is consistent with less color centers, due to filling of oxygen vacancies.

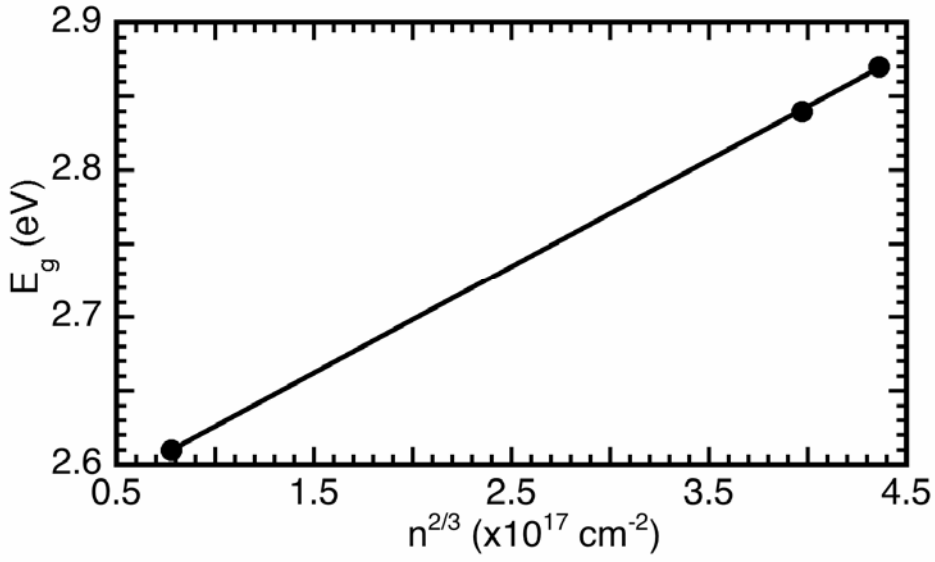

Figure 6.18. Linear dependence of band gap vs. $n^{2/3}$ of as prepared, 300˚C and 400˚C air annealed ZIO films.

The average transmission of the 185 nm films is 83 % when annealed at temperatures up to 300˚C. At higher temperatures average transmission somewhat decreases due to red-shift of the band gap deeper into the visible spectrum. No noticeable thickness variation with annealing temperature is observed.

To conclude, amorphous $Zn_2In_2O_5$ films deposited in O_2 (g) at room temperature are highly stable structurally, electrically and optically at temperatures up to 300˚C. The electro-optical properties degrade above 400˚C due to a reduced carrier concentration and a discoloration, although the amorphous structure of the films prevails. A high conductivity of 1900 S/cm is measured. Further investigation of air-annealed films is required, in particular using transient conductivity measurements with annealing time, and higher annealing temperatures to find a possible crystallization temperature of the amorphous films.

6.3.6. Doping of $Zn_2In_2O_5$

In an attempt to increase the conductivity of the crystalline or amorphous $Zn_2In_2O_5$ thin films, W-doping is studied. It has been found that a moderate ~3% W-doping [11] in In_2O_3 thin films produces electron carriers and greatly enhances their mobility. A 5% tungsten doped target of $Zn_2In_{1.95}W_{0.05}O_{5+\delta}$ (ZIOW) stoichiometry is used to deposit thin films in vacuum and 10^{-3} Torr O_2 (g) on unheated or 350˚C-heated substrates.

ZIOW films remain amorphous at substrate temperatures up to 350˚C and 10^{-3} Torr O_2 (g) during the deposition. Undoped ZIO are crystalline at equivalent

deposition parameters, thus W-doping inhibits the crystallization of the $Zn_2In_2O_5$ crystalline phase. In_2O_3 XRD peaks are observed for 400˚C substrate temperature deposited films. The surface roughness of the films is low, < 1 nm, as expected for amorphous films.

An experiment on e*x-situ* heating in air at temperatures up to 500˚C does not lead to crystallization of ZIOW films, similar to the undoped films.

Electrical characteristics of the ZIOW thin films are inferior to those of undoped ZIO, as shown in Table 6.2. The presence of W in the films reduces carrier concentration and mobility, as also reported in literature with other dopants such as Al, Sn, Ga *etc*. [7,9,10]. We speculate that the W-dopant may be incorporated predominantly onto In sites in the 2+ state and thus act as an electron acceptor with a high carrier scattering cross-section. This leads to an overall lower conductivity of ZIOW films with respect to the undoped ZIO films. The experiment of room temperature deposited films in O_2 (g) and post-annealing in air also results in lower conductivities. However, low carrier concentrations of about 10^{16} cm^{-3} are not obtained for application in amorphous transparent thin film transistors as a channel material by any of the aforementioned preparation methods. The inferior carrier mobility with doping is also undesirable in thin film devices.

Optical properties of the ZIOW films are similar to those of undoped films, also compared in Table 6.2. The band gaps of the W-doped films increase with a decrease in carrier concentration, compared to the undoped counterparts. The absorption coefficient in the visible optical range is higher in almost all cases.

Table 6.2. Electrical and optical properties comparison of W-doped and undoped $Zn_2In_2O_5$ thin films.

Sample preparation	Conductivity, S/cm	Carrier Conc., $x10^{20}$ cm^{-3}	Mobility, cm^2/Vs	Absorption @520 nm, cm^{-1}	Band Gap, eV
undoped, 10^{-3} Torr Ar-20%O_2, 350˚C	1441	3.7	24	2620	2.95
W-doped 10^{-3} Torr Ar-20%O_2, 350˚C	818	2.9	17	11000	3.08
undoped 10^{-3} Torr O_2, rT	1720	2.87	37	1140	2.8
W-doped 10^{-3} Torr O_2, rT	645	2.71	15	6050	2.9
undoped, 500˚C post-annealed	8.3	$1.8x10^{-2}$	29	450	2.54
W-doped, 500˚C post-annealed	1.4	$6.6x10^{-3}$	13	295	2.65

A ZIO film doped with 5 at. % Si substituting for In is also deposited and characterized. The electrical measurements result in low conductivity, consistent with an acceptor doping reducing the carrier concentration. Similar to W-doping, the incorporation of Si prevents the formation of crystalline films at elevated substrate temperatures.

In review, a 5% substitutional doping of In by W in ZIO results in highly stable amorphous films. The presence of the dopant reduces the carrier concentration and mobility of electron carriers. Further experiments with various dopant concentrations are required to show solubility in the crystalline lattice.

6.4. Conclusions

Amorphous ZIO films deposited at room temperature in O_2 (g) yield high electrical conductivity near 1700 S/cm. A high carrier mobility of 40 cm^2/Vs is typical for these films. The amorphous phase is stable up to 500˚C annealing in air. The carrier effective mass of 0.5 m_0 is the same as in crystalline ZIO. Optical band gaps of 2.8 eV are typical of amorphous ZIO films, somewhat below the desired 3.1 eV for TCO applications.

The electrical and optical properties of 350˚C deposited crystalline ZIO thin films are strongly affected by the oxygen gas pressure in the deposition chamber. An increase of O_2 (g) pressure during deposition leads to a decrease carrier concentration. Mobility values up to 28 cm^2/Vs are measured, due to reduced carrier scattering. The carrier effective mass of 0.5 m_0 is calculated from observed Burstein-Moss shifts, characteristic to ZIO thin films. The upper limit of substrate heat for single-phase $In_2Zn_2O_5$ thin film deposition by PLD has been established at 350˚C.

Amorphous ZIO thin films deposited in ultra-high vacuum are only moderately conductive around 150 S/cm and with a low band gap of 2.6 eV. High absorption from structural defects contributes to a strong discoloration of films. Deposition of ZIO films above 200˚C in UHV leads to crystallization of the $In_2Zn_2O_5$ phase. The crystalline films are predominantly *c*-axis oriented. Oxygen vacancies contribute to generation of high electron carrier densities. Introduction of 1×10^{-3} Torr Ar (g) during the deposition enhances the mobility to 17 cm^2/Vs and results in the high conductivity of 1920 S/cm in crystalline ZIO films. A wide band

gap of 3.2 eV is measured. Based on these results, UHV and Ar (g) deposited crystalline ZIO films are suitable candidates for TCO application.

Structural, electrical and optical properties of undoped and W-doped $Zn_2In_2O_5$ thin films are evaluated and compared in the amorphous and crystalline phases. W-incorporation into $Zn_2In_2O_5$ reduces carrier concentration and mobility. Doping is found to stabilize the amorphous phase of ZIO films even at elevated substrate temperatures during deposition, where crystalline films of undoped $Zn_2In_2O_5$ are prepared.

References

1. Flexible Flat Panel Displays, Ch.5, Edited by G.P. Crawford, John Wiley & Sons 2005
2. T. Moriga, D.D. Edwards, T.O Mason, G.B. Palmer, K.R. Poppelmeier, J.L. Schindler, C.R. Kannewurf and I. Nakabayashi, J. Am. Ceram. Soc. 81 (1998) 1310
3. T. Minami, T. Kakumu, Y. Takeda, S. Takata, Thin Solid Films 317 (1998) 326
4. T. Minami, H. Sonohara, T. Kakumu and S. Takata, Jpn. J. Appl. Phys. 34 (1995) L971
5. R. Wang, L. L. H. King, and A. W. Sleight, J. Mater. Res. 11 (1996) 1659
6. N. Naghavi, C. Marcel, L. Dupont, A. Rougier, J. Leriche and C. Guery. J. Mater. Chem 10 (2000) 2315
7. K. Tominaga, T. Takao, A. Fukishima, T. Moriga and I. Nakabayashi, Vacuum 66 (2002) 505
8. J.M. Phillips, R.J. Cava, G.A. Thomas, S.A. Carter, J. Kwo, T. Siegrist, J.J. Krajewski, J.H. Marshall, W.F. Peck, Jr., and D.H. Rapkine, Appl. Phys. Lett., 67 (1995) 2246

9. T. Minami, T. Kakumu, and S. Takata, J. Vac. Sci. Technol. A 14 (1996) 1704
10. T. Minami, S. Takata and T. Kakumu, J. Vac. Sci. Technol. A 14(1996) 1689
11. P. Newhouse, C.-H. Park, D.A. Keszler, J.Tate, and P.S. Nyholm, Appl. Phys. Lett. 87 (2005) 112108
12. H. Nakazawa, Y. Ito, E. Matsumoto, K. Adachi, N. Aoki and Y. Ochiai, J. Appl. Phys. 100 (2006) 093706
13. H. Hosono, J Non-Cryst Solids 352 (2006) 851, N.Ito etal, TSF 496 (2005) 99
14. N. Ito, Y. Sato, P. K. Song, A. Kaijio, K. Inoue and Y. Shigesato, Thin Solid Films 496 (2005) 99
15. D. L. Smith, Thin-Film Depostion, Ch.5. McGraw-Hill (1995)
16. C. Marcel, N. Naghavi, G. Couturier, J. Salardenne, J.M. Tarascon, J. Appl. Phys. 91 (2002) 4291
17. E. Burstein, Phys. Rev. 93 (1954) 632
18. T. S. Moss, Proc. Phys. Soc. London B67 (1954) 775
19. C. R. Pidgeon, Handbook on semiconductors, North Holland, Amsterdam 1980 vol.2, p.231
20. T. Hamberg and C. G. Granqvist, J. Appl. Phys. 60 (1986) R123
21. O. N. Mryasov and A. J. Freeman, Phys. Rew. B 64 (2001) 233111
22. H. Hosono, N. Kikuchi, N. Ueda, H. Kawazoe, J. Non-Cryst. Solids 198-200 (1996) 165
23. H. Hosono, M. Yasukawa, H. Kawazoe, J. Non-Cryst. Solids 203 (1996) 334
24. B. Kumar, H. Gong, R. Akkipeddi, J. Appl. Phys. 98 (2005) 073703
25. B. Yaglioglu, Y.-J. Huang, H.-Y. Yeom and D. C. Paine, Thin Solid Films 496 (2005) 89
26. N.L.Dehuff, E.S. Kettenring, D. Hong, H. Q. Chiang, J. F. Wager, R. L. Hoffman, C.-H. Park, and D. A. Keszler, J. Appl. Phys. 97 (2005) 064505

Chapter 7. Summary

In this work thin films of various *p*- and *n*-type wide band-gap semiconductors have been prepared by the PLD technique, characterized by structural, electrical and optical methods, and compared to other existing transparent conductors. First, we summarize the *p*-type thin films of the BaCuQF (Q = S, Se, Te) family – promising candidates for passive and active device applications. This is followed by a summary of the high conductivity, electron majority carrier crystalline and amorphous $Zn_2In_2O_5$ films as possible replacements for the high-cost In_2O_3 based TCOs. Recommendations for future investigation conclude this chapter.

7.1. BaCuQF (Q = S, Se, Te)

BaCuQF film properties strongly depend on the PLD deposition parameters. We find that crystalline BaCuSeF and BaCuTeF films form *in-situ* during deposition at elevated (300˚C or above) substrate temperatures. Epitaxial BaCuTeF and highly textured BaCuSeF film growth on MgO substrates is achieved. Preferential *c*-axis orientated growth of BaCuSeF films on SiO_2 substrate develops at temperatures above 450˚C. BaCuSF films do not form under such deposition conditions, and a different route of an amorphous film deposition at room temperature and *ex-situ* post-annealing is used. BaCuSF films also show preferential *c*-axis orientation on SiO_2 substrates upon crystallization above 400˚C by rapid thermal annealing (RTA).

Laser fluence is identified as the most important deposition parameter to produce single-phase films. Epitaxial and polycrystalline BaCuTeF films are achieved using laser power of 1.0 J/cm^2, on a single-crystal MgO and fused silica substrates, respectively. A lower, 0.5 J/cm^2 fluence, produces *c*-axis oriented BaCuSF films following an RTA process, on amorphous substrates. We estimate that best quality BaCuSeF films can be deposited using ~ 0.75 J/cm^2. Hence progressively lower laser fluence of 1.0 to 0.5 J/cm^2 is required for deposition of phase-pure BaCuQF films in the order of smaller Q = Te, Se, and S chalcogen anions. Introduction of a inert deposition gas, for example Ar, background pressure considerably improves the crystalline structure of the deposited BaCuQF films, resulting in narrower XRD peaks and higher carrier mobility.

The electrical properties of the films are in good agreement with trend of decreasing conductivity with smaller chalcogen atom in BaCuQF powders. Epitaxial BaCuTeF films (on MgO substrates) exhibit a high conductivity of 167 S/cm, which decreases to 0.5 S/cm S/cm for BaCuSeF (on MgO substrate) and to 0.2 S/cm for BaCuSF (on SiO_2 substrate). Carrier mobility also decreases with smaller chalcogen atom, as expected from band structure calculations. The mobility of 8 cm^2/Vs (BaCuTeF) and 1.5 cm^2/Vs (BaCuSeF) are high in the framework of p-TCs. The lower conductivity in BaCuSeF is due to a 1.7 x 10^{18} cm^{-3} carrier concentration, two orders of magnitude smaller than in BaCuTeF. Polycrystalline films have lower mobility due to grain boundary scattering. For BaCuSF films, a reliable measurement of the Hall coefficient is not available, but low mobility is expected. Similar values of

positive Seebeck coefficients indicate comparable hole carrier concentrations in BaCuSF and BaCuTeF.

High carrier concentration produces conductivity in BaCuSF thin films by rapid thermal annealing in Ar (g). Similar crystallization of amorphous BaCuTeF films by Ar (g) RTA also leads to high carrier concentration of ~10^{21} cm^{-3} and improved conductivity of polycrystalline films. Application of these high hole-carrier concentration materials in solar cells as wide-band gap p^+-contacts is currently under investigation. BaCuSF films crystallized in flowing H_2S (g) have lower carrier concentrations, estimated at 5 x 10^{19} cm^{-3}, and application in TTFT devices is attempted.

We now turn to the optical properties of BaCuQF films. Excitonic absorption features are observed in BaCuSF and BaCuSeF films indicating the upper limit of transmitted photon energies. A binding energy of 36 meV is estimated for BaCuSF excitons forming a series of absorption peaks at 3.3 eV and 3.4 eV. Excitons shift towards lower energies in BaCuSeF, in good agreement with the expected smaller band gap. This exciton pair near 3.0 eV and 3.1 eV impinges on the transparency of BaCuSeF films in the visible range. BaCuTeF films exhibit a 3 eV direct band gap, much higher than 2.3 eV measured in bulk samples, and no excitonic absorptions are present. Absorption coefficients of 5000 – 15000 cm^{-1}, evaluated at 520 nm photon wavelength, and over 70% transparency in the visible range are typical for BaCuQF films.

The summarized properties identify BaCuQF films as good candidates for application is solid-state devices. For example, BaCuSF and BaCuTeF with high

carrier concentrations are prospective candidates for p^+-contacts in solar cells, LEDs and TTFTs. The low carrier concentration and good mobility in BaCuSeF are attractive properties for active channel layer application in TTFTs.

7.2. $Zn_2In_2O_5$

Crystalline and amorphous $Zn_2In_2O_5$ (ZIO) thin films are produced by PLD under various deposition conditions. Single-phase crystalline films are preferentially *c*-axis oriented on fused SiO_2 substrates, when optimal 1 J/cm^2 laser fluence and 200˚C – 350˚C substrate temperatures are used. ZIO films remain amorphous at lower substrate temperatures. The amorphous phase is extremely stable and no crystallization is observed at temperatures as high as 500˚C, although electrical conductivity decreases above 400˚C.

A high conductivity of 1.92 x 10^3 S/cm is achieved in the crystalline phase of ZIO. The indirect band gap is 3.2 eV – blue-shifted due to the high carrier concentration in the film. Amorphous ZIO films exhibit comparable conductivity to the crystalline counterparts, but the band gap shrinks to 2.8 eV. The electron carrier effective mass of 0.5 m_0 is characteristic for the crystalline and amorphous phases.

Although ZIO films have lower conductivity than other crystalline *n*-type TCOs, it is a potential competitor for reduced cost replacement of ITO in the amorphous phase, due to higher conductivity and phase stability.

7.3. Recommendations for future investigations

To date, BaCuSF films have not been prepared by an *in-situ* PLD process. We believe that the use of 2 J/cm^2 laser fluence causes the formation of multi-phase films deposited from a BaCuSF target at elevated substrate temperatures. Recently, *ex-situ* crystallized single-phase films are achieved using a lower 0.5 J/cm^2 laser fluence for the deposition of the amorphous BaCuSF film at room temperature. It is possible that single-phase crystalline BaCuSF can be prepared by an *in-situ* PLD process at optimal deposition conditions, such as 0.5 J/cm^2 laser fluence and high substrate temperature. Preparation of textures BaCuSF thin films on single-crystal substrates would allow us to directly determine the carrier concentration and mobility, and clarify the properties of excitons observed in polycrystalline films. High quality thin films of BaCu(S,Se)F and BaCu(Se,Te)F solid solutions would provide further insight into the spin-orbit splitting of the exciton peaks observed in BaCuSeF, and their disappearance in BaCuTeF.

High mobility, low carrier concentration and wide band-gap thin films are required for successful application in TTFT devices. High mobility, but also high carrier concentrations are obtained in epitaxial BaCuTeF films with a 3 eV band gap. Donor doping on the Cu site by M^{2+} cations, such as Zn, would reduce the carrier concentration. Such doping method also lowers carrier mobility, due to introduction of scattering centers into the conduction path of the layered structure. Doping on the Ba-site by Ln^{3+} lanthanides is promising, placing the defects into the BaF_2 layer. However, lanthanides generally have smaller ionic radii than the Ba ion, such that the

doping is unlikely to take place. ACuQF (Q = S, Se) compounds can also be prepared with the smaller A = Sr alkali atom. The smaller ionic radius of Sr makes lanthanide doping possible. Thus we propose to attempt synthesis of SrCuTeF and ($Sr_{1-x}La_xCuTeF$), in which lower carrier concentrations are expected, while maintaining high carrier mobility.

Investigation of the β–$BaCu_2S_2$, $BaCu_2Se_2$, $BaCu_2Te_2$ and the respective solid solutions in the thin film form are promising candidates for thermoelectric applications. These materials have a common naturally layered structure, where layers of $(CuQ)_2$ (Q = S, Se, Te) are separated by Ba sheets. A low thermal conductivity is expected due to this layered structure, whereas conductivities much higher than in BaCuQF materials can be achieved by doping.

Amorphous $Zn_2In_2O_5$ thin films are highly conductive. In this research work, annealing in air on the order of an hour indicates high stability of the amorphous phase at temperatures as high as 500˚C, although a noticeable decrease in conductivity takes place. Long-term (many hours, days) exposure to elevated temperatures, its effect on the thin film crystalline structure and electrical performance are yet to be studied.

Bibliography

A. Romeo, M. Terheggen, D. Abou-Ras, D.L. Batzner, F.-J. Haug, M. Kalin, D. Rudmann and A.N. Tiwari. Progr. Photovolt. 12 (2004) 93

A.N. Banerjee, K.K. Chattopadhayay, Review Article, Progress in Crystal Growth and Characterization of Materials 50 (2005) 52

B. Kumar, H. Gong and R. Akkipeddi, J. Appl. Phys. 98 (2005) 073703

B. Yaglioglu, H. Y. Yeom, R. Beresford, and D. C. Paine, Appl. Phys. Lett. 89 (2006) 062103

B. Yaglioglu, Y.-J. Huang, H.-Y. Yeom and D. C. Paine, Thin Solid Films 496 (2005) 89

C. C. Chang, X. D. Wu, R. Ramesh, X. X. Xi, T. S. Ravi, T. Venkatesan, D. M. Hwang, R. E. Muenchausen, S. Foltyn, and N. S. Nogar, Appl. Phys. Lett. 57 (1990) 1814

C. L. Yaws, Handbook of Thermal Conductivity, v. 4, Gulf Publication Co., 1995

C. Marcel, N. Naghavi, G. Couturier, J. Salardenne, J.M. Tarascon, J. Appl. Phys. 91 (2002) 4291

C. R. Pidgeon, Handbook on semiconductors, North Holland, Amsterdam 1980 vol.2, p.231

C.-H. Park, D. A. Keszler, H. Yanagi, and J. Tate, Thin Solid Films 445 (2003) 288

C.-H. Park, PhD dissertation, Oregon State University, 2005, Call # LD4330 2005D .P37.

C.-H. Park, R. Kykyneshi, A. Yokochi, J. Tate, and D. A. Keszler, J. Solid State Chem. 180 (2007) 1672

Chapters 4,5 and 8; Pulsed Laser Deposition of Thin Films, edited by D.B. Chrisey and G.K. Graham, John Wiley and Sons, (1994)

CRC Handbook of Chemistry and Physics, 58th edtion, edited by R. C. Weast, CRC Press Inc. 1977

D. K. Schroder, Semiconductor Material and Device Characterization, John Wiley and Sons, (2005)

D. L. Smith, Thin-Film Depostion, Ch.5. McGraw-Hill (1995)

E. Burstein, Phys. Rev. 93 (1954) 632

Flexible Flat Panel Displays, Ch.5, Edited by G.P. Crawford, John Wiley & Sons 2005

G. K. Williamson and W. H. Hall, Acta Metallurgica 1 (1953) 22

G. Thomas, Nature 389 (1997) 907

H. Hiramatsu, H. Ohta, T. Suzuki, C. Honjo, Y. Ikuhara, K. Ueda, T. Kamiya, M. Hirano, and H. Hosno, Crystal Growth and Design 4 (2004) 301

H. Hiramatsu, K. Ueda, H. Ohta, M. Hirano, T. Kamiya, and H. Hosono, Appl. Phys. Lett. 82 (2003) 1048

H. Hiramatsu, K. Ueda, H. Ohta, M. Hirano, T. Kamiya, H. Hosono, Thin Solid Films 445 (2003) 304

H. Hiramatsu, K. Ueda, H. Ohta, M. Orita, M. Hirano, and H. Hosono, Appl. Phys. Lett. 81 (2002) 598-600

H. Hiramatsu, K. Ueda, K. Takafuji, H. Ohta, M. Hirano, T. Kamiya, and H. Hosono, J. Mater. Res. 19 (2004) 2137-2143

H. Hiramatsu, K. Ueda, K. Takafuji, H. Ohta, M. Hirano, T. Kamiya, H. Hosono, Appl. Phys. A 79 (2004) 1521-1523

H. Hiramatsu, M. Orita, M. Hirano, K. Ueda, and H. Hosono, J. Appl. Phys. 91 (2002) 9177

H. Hosono, M. Yasukawa, H. Kawazoe, J. Non-Cryst. Solids 203 (1996) 334

H. Hosono, N. Kikuchi, N. Ueda, H. Kawazoe, J. Non-Cryst. Solids 198-200 (1996) 165

H. Kabbour, L. Cario, S. Jobic, and B. Corraze, J. Mater. Chem 16 (2006) 4165

H. Kawazoe, M. Yasukawa, H. Hyodo, M. Kurita, H. Yanagi, H. Hosono, Nature 389 (1997) 939

H. L. Tuller and A. S. Nowick, J. Phys. Chem. Solids 38 (1977) 859

H. Nakazawa, Y. Ito, E. Matsumoto, K. Adachi, N. Aoki and Y. Ochiai, J. Appl. Phys. 100 (2006) 093706

H. Q. Chiang, D. Hong, C. M. Hung, R. E. Presley, J. F. Wager, C.-H. Park, D. A. Keszler, G. S. Herman, J. Vac. Sci. Technol. B 24 (2006) 2702

H. Yanagi, J. Tate, S. Park, C.-H. Park and D. A. Keszler, Appl. Phys. Lett. 82 (2003) 2814

H. Yanagi, J. Tate, S. Park, C.-H. Park, D. A. Keszler, M. Hirano, and H. Hosono, J. Appl. Phys. 100 (2006) 083705

H. Yanagi, K. Ueda, H. Ohta, M. Orita, M. Hirano, H. Hosono, Solid State Commun. 121 (2001) 15

H. Yanagi, S. Park, A. D. Draeseke, D. A. Keszler, and J. Tate, Sol. St. Chem. 175 (2003) 34

H. Yanagi, T. Hase, S. Ibuki, K. Ueda, H. Hosono, Appl. Phys. Lett. 78 (2001) 1583

Handbook of Photovoltaic Science and Engineering, edited by A. Luque and S. Hegedus, John Wiley and Sons, Ltd (2003)

Hosono, J Non-Cryst Solids 352 (2006) 851, N.Ito etal, TSF 496 (2005) 99

I. Grozdanov and M. Najdoski. J. Solid State Chem. 114 (1995) 469

J. F. Wager, Science 300 (2003) 1245

J. Tate, M.K. Jayaraj, A.D. Draeseke, T. Ulbrich, A.W. Sleight, K.A. Vanaja, R. Nagarajan, J.F. Wager, R.L. Hoffman, Thin Solid films 411 (2002) 119

J.M. Phillips, R.J. Cava, G.A. Thomas, S.A. Carter, J. Kwo, T. Siegrist, J.J. Krajewski, J.H. Marshall, W.F. Peck, Jr., and D.H. Rapkine, Appl. Phys. Lett., 67 (1995) 2246

K. Nomura, H. Ohta, K. Ueda, T. Kamiya, M. Hirano, and H. Hosono, Science 300 (2003) 1269

K. Tominaga, T. Takao, A. Fukishima, T. Moriga and I. Nakabayashi, Vacuum 66 (2002) 505

K. Ueda, H. Hiramatsu, H. Ohta, M. Hirano, T. Kamiya, and H. Hosono, Phys. Rev. B 69 (2004) 155305

K. Ueda, S. Inoue, S. Hirose, H. Kawazoe, and H. Hosono, Appl. Phys. Lett. 77 (2000) 2701

L. Kilcher, senior thesis, Oregon State University (2003), unpublished

M. C. Spiegelberg MS thesis, Oregon State University, 2006, Call #LD4330 2006 .S66

M. Elazhari, A. Ammar, M. Elaatmani, M. Trari, J. P. Doumerc, Eur. J. Solid State Chem. 34 (1997) 503

M. K. Jayaraj, A.D. Draeseke, J. Tate, A.W. Sleight, Thin Solid Films 397 (2001) 244

N. Naghavi, C. Marcel, L. Dupont, A. Rougier, J. Leriche and C. Guery, J. Mater. Chem. 10 (2000) 2315

N. Naghavi, C. Marcel, L. Dupont, A. Rougier, J. Leriche and C. Guery. J. Mater. Chem 10 (2000) 2315

N. Ito, Y. Sato, P. K. Song, A. Kaijio, K. Inoue and Y. Shigesato, Thin Solid Films 496 (2005) 99

N. L. Dehuff, E.S. Kettenring, D. Hong, H. Q. Chiang, J. F. Wager, R. L. Hoffman, C.-H. Park, and D. A. Keszler, J. Appl. Phys. 97 (2005) 064505

NIST, Standard Reference Materials, www.nist.gov

O. N. Mryasov and A. J. Freeman, Phys. Rew. B 64 (2001) 233111

P. Blaha, K. Schwarz, G. K. H. Madsen, D. Kvasnicka and J. Luitz, WIEN2k, An Augmented Plane Wave + Local Orbitals Program for Calculating Crystal Properties (Karlheinz Schwarz, Techn. Universitat Wien, Austria), 2001. ISBN 3-9501031-1-2

P. J. Cannard and R. J. D. Tilley, J. Solid State Chem. 116 (1988) 418

P. Kubelka and F. Munk, Zh. Tekh. Fiz. 12 (1931) 593; P. Kubelka, J. Opt. Soc. Am. 38 (1948) 448

P. Newhouse, C.-H. Park, D.A. Keszler, J.Tate, and P.S. Nyholm, Appl. Phys. Lett. 87 (2005) 112108

P. Y. Yu and M. Cardona, Fundamentals of Semiconductors: Physics and Materials Properties, 3rd edition, Springer, 2001 p. 269.

Pulsed Laser Deposition of Thin Films, edited by D. B. Chrisey and G. K. Graham, John Wiley and Sons,New York, Chichester, Brisbane, Toronto, Singapore (1994)

R, L. Hoffman, B. J. Norris, and J. F. Wager, Appl. Phys. Lett. 82 (2003) 733

R. E. Presley, D. Hong, H. Q. Chiang, C. M. Hung, R. L. Hoffman, J. F. Wager, Solid-State Electronics 50 (2006) 500

R. Kykyneshi, B. C. Nielsen, J. Tate, J. Li, and A. W. Sleight, J. Appl. Phys. 96 (2004) 6188

R. Kykyneshi, D. H. McIntyre, J. Tate, C.-H. Park, D. A. Keszler, J. Solid State Sci. (2007) in print

R. Kykyneshi, MS thesis, Oregon State University (2004), Call # LD4330 2005 .K95

R. L. Hoffman, B. J. Norris and J. F. Wager. Appl. Phys. Lett. 82 (2003) 733

R. Nagarajan, A. Draeseke, A. W. Sleight, and J. Tate, J. Appl. Phys. 89 (2001) 8022

R. Wang, L. L. H. King, and A. W. Sleight, J. Mater. Res. 11 (1996) 1659

Raytek Marathon pyrometer, Operator's manual

S. M. Sze, Physics of Semiconductor Devices, 2nd edition, John Wiley and Sons, New York , Chichester, Brisbane, Toronto (1981), p. 828

S. Park, D. A. Keszler, M. M. Valencia, R. L. Hoffman, and J. F. Wager, Appl. Phys. Lett. 80 (2002) 4393-4394

S.B.Zhang, S.-H. Wei, and A. Zunger, Jour. Appl. Phys. 83 (1998) 3192

S.-M. Park, T. Ikegami, K. Ebihara, Jpn. J. Appl. Phys. 44 (2005) 8027

SPI Supplies, www.2spi.com

T. Hamberg and C. G. Granqvist, J. Appl. Phys. 60 (1986) R123

T. Minami, H. Sonohara, T. Kakumu and S. Takata, Jpn. J. Appl. Phys. 34 (1995) L971

T. Minami, S. Takata and T. Kakumu, J. Vac. Sci. Technol. A 14(1996) 1689

T. Minami, T. Kakumu, and S. Takata, J. Vac. Sci. Technol. A 14 (1996) 1704

T. Minami, T. Kakumu, Y. Takeda, S. Takata, Thin Solid Films 317 (1998) 326

T. Moriga, D.D. Edwards, T.O Mason, G.B. Palmer, K.R. Poppelmeier, J.L. Schindler, C.R. Kannewurf and I. Nakabayashi, J. Am. Ceram. Soc. 81 (1998) 1310

T. Moriga, D.D. Edwards, T.O Mason, G.B. Palmer, K.R. Poppelmeier, J.L. Schindler, C.R. Kannewurf and I. Nakabayashi, J. Am. Ceram. Soc. 81 (1998) 1310

T. O. Mason, G. B. Gonzalez, D. R. Kammler, N. Mansourian-Hadavi, B. J. Ingram, Thin Solid Films 411 (2002) 106

T. S. Moss, Proc. Phys. Soc. London B67 (1954) 775

W. B. Jackson, R. L. Hoffman, G. S. Herman, Appl. Phys. Lett. 87 (2005) 193503

X. L. Yang, S. H. Guo, F. T. Chan, K. W. Wong, and W. Y. Ching. Phys. Rev. A 43 (1991) 1186

X. Nie, S.-H. Wei, and S. B. Zhang, Phys. Rev. Lett. 88 (2002) 066405

Y. C. Wang, F. J. DiSalvo, J. Solid State Chem. 156 (2001) 44.

Y. Hishikawa, N. Nakamura, S. Tsuda, S. Nakano, Y. Kishi, and Y. Kuwano, Jap. J. Appl. Phys. 30 (1991) 1008-1014

Appendix A. Substrate temperature calibration (Thermionics chamber).

Substrate temperature is an important thin film deposition parameter. It strongly influences the crystal structure of the growing thin films from amorphous to polycrystalline and epitaxial. Good temperature control ensures the reproducibility of desired film properties regardless of the deposition system used.

Elevated substrate temperatures are achieved using radiative heating of halogen lamp sources source during thin film deposition described in this work, in the ultra-high vacuum chamber of an in-house design (built by Thermionics). The substrate temperature is difficult to control. First, it is a thermocouple near the lamp that provides the temperature information to the feedback loop, rather than a substrate surface temperature. Second, large temperature gradients may occur between the platen and the substrate surface and depending on the contact procedure. Third, the surface temperature changes as the film is deposited due to changes in emissivity. This last variable is very hard to control, but optically contacting the substrate to the platen, and directly measuring the substrate temperature at set lamp temperatures can minimize the error in the former two variables.

The substrate holder used for thin film depositions by PLD throughout the experimental work described in this dissertation is shown in Fig. A.1. The substrate is optically connected to the stainless steel disk in the middle of the holder. The steel disk is directly heated by the source. This configuration is used to avoid warping of the substrate holder due to inhomogeneous expansion of its constituents at elevated temperatures. The disk surface is machined flat and polished with 1500 grit sandpaper

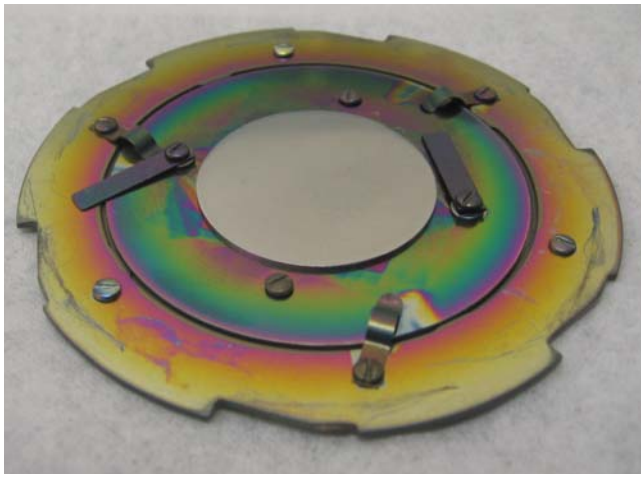

Figure A.1. Substrate holder for PLD deposition. The halogen lamps directly heat the stainless steel disk in the middle through an opening under the disk.

under flowing water. This ensures a smooth contact surface between the disk and the substrate. Newton rings are observable when intimate contact is achieved, and the substrate does not fall off when the platen is flipped upside down. For best results, the substrate is slid onto the disk from one side. To ensure safe transferring into the deposition chamber, the clips around the disk secure the substrate.

A pyrometer (Raytek Marathon series) operating at 1.6 μm is used for the substrate temperature calibration. The emissivity of fused silica, as well as MgO, is very low, therefore the substrate surfaces are coated with a thin layer of graphite. The emissivity of the graphite layer from colloidal solution is determined from simultaneous measurements of a coated substrate temperature by the pyrometer and a type-K thermocouple with the aid of a hot plate. This setup is shown in Fig. A.2. An emissivity of 0.92 is determined, in good agreement with available graphite emissivity data [1]. This value is used for the temperature calibration of various substrates inside the deposition chamber. Placing a view port used on the chamber between the pyrometer and the heated substrate does not affect the temperature reading.

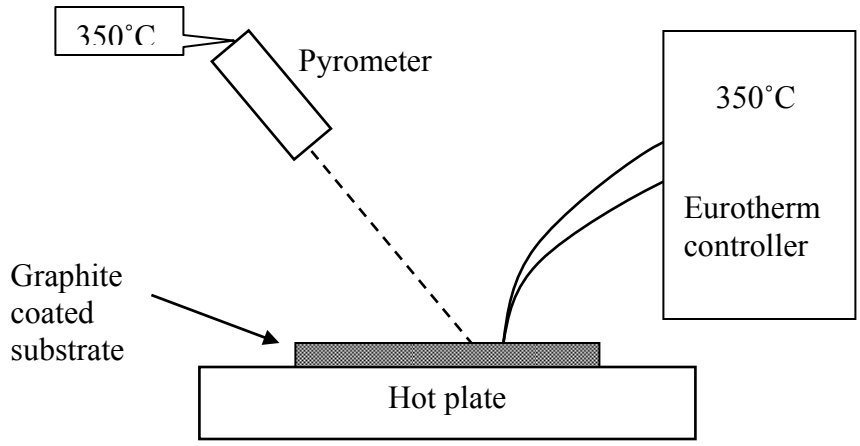

Figure A.2. Determination of graphite emissivity, comparing pyrometer and type-K thermocouple temperature readings on a coated 1.2 mm thick fused silica substrate.

Optically contacted and graphite coated substrates on platens are placed into the deposition chamber. The pyrometer is set up at a view port, which allows temperature reading at about 30˚ from the vertical position. The total distance between the substrate and pyrometer is about 90 cm. The distance to spot-size ratio of the pyrometer is 200:1, thus the spot size on the substrate is 4.5 mm.

Calibration curves are measured for 1.2 mm thick fused-silica and 0.5 mm single-crystal MgO substrates, shown in Fig. A.3. The lamp source is ramped to various set temperatures and reading the corresponding pyrometer reading of the graphite coated substrate surface temperature is recorded. A linear regression is sufficient to fit the calibration data; the line equations for the various substrates are shown in the Fig. A.3. Thinner, 0.5 mm, fused silica substrates result in substrate temperature about 20˚C higher, compared to the thicker 1.2 mm SiO_2 substrate. The maximum temperature rating of the lamp is 1200˚C, thus the highest obtainable temperature of the fused silica substrate is 600˚C. For MgO substrates, a higher 650˚C

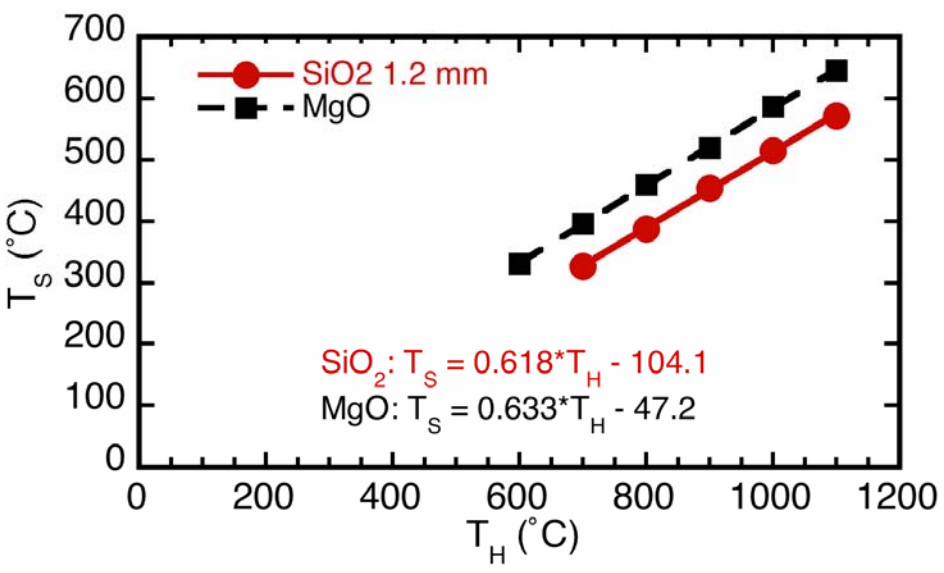

Figure A.3. Calibration curves for 1.2mm thick fused silica and 0.5 mm thick MgO substrates. T_H is the set temperature of the W-lamp heaters and T_S is the actual substrate temperature.

temperature maximum is measured, due to a higher thermal conductivity. Thermal properties of the SiO_2, MgO, and graphite are summarized in Table A.1.

Based on this calibration, we estimate that all temperatures reported here are accurate to 10˚C. This calibration is not applicable for low substrate temperatures below 100˚C.

Table A.1. Thermal conductivity and expansion coefficients of SiO_2, MgO and graphite.

	Thermal conductivity At 0˚C and 600˚C (W/mK)	Thermal expansion coef. at 20˚C, (10^{-6} K^{-1})
Fused silica [2,3]	50, 10	0.5
MgO [2,4]	1, 3	8
Graphite [5]	90.9 (0˚C)	-

References

1. Raytek Marathon pyrometer, Operator's manual
2. C. L. Yaws, Handbook of Thermal Conductivity, v. 4, Gulf Publication Co., 1995
3. CRC Handbook of Chemistry and Physics, 58th edition, edited by R. C. Weast, CRC Press Inc. 1977
4. SPI Supplies, www.2spi.com
5. NIST, Standard Reference Materials, www.nist.gov

Appendix B. An *in-situ* shadow mask exchange system.

Thin films depositions described in the current work used no deposition mask for blanket-coated substrates, or a Hall-cross shadow mask (increasing Hall coefficient measurement reliability). For more complicated structures, such as thin film transistors (TFT), deposition of multiple, various shape layers is required. In the present system, the film structure has to be removed from the chamber and exposed to atmosphere between each layer to change the shadow mask. Exposure to atmosphere may lead to unwanted oxidation of surfaces, and possibly lead to degraded performance of the finished device.

A mask exchange system is developed [1], which makes possible the delivery of new masks for successive deposition layers within the ultra-high vacuum chamber. Parts of the exchange mechanism are shown in Fig. B.1, which works on the same principle of mounting hooks and twist-on substrate holder already present in the Thermionics deposition system. For simplicity of the mask transfer system

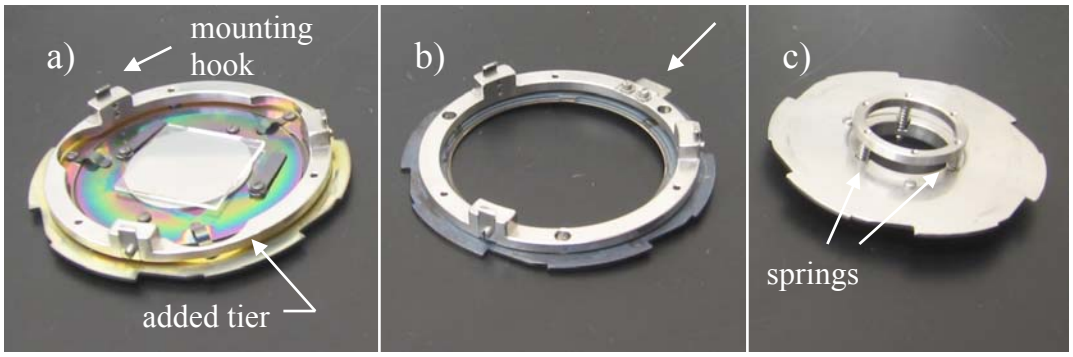

Figure B.1. Mask transfer system: a) platen with substrate with an additional tier of mounting hooks placed into the chamber; b) similar setup to a) equipped with a stopper, marked by arrow; c) spring loaded, twist-on mask-mount.

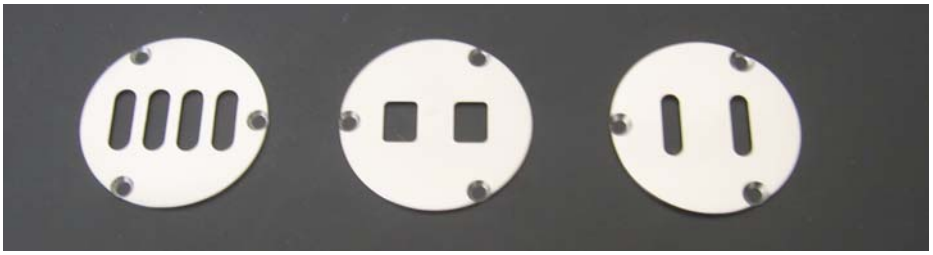

Figure B.2. Currently available masks for the transfer system. The set of masks are designed for *in-situ* TFT structure deposition. The masks, from left to right, are for contacts, channel layer and protective layer depositions.

description its components are referred to as parts "a", "b" and "c", in the order as they appear in Fig. B.1. Part "a" is a modified version of the substrate holder (Appendix A), with an added tier of mounting hooks (Fig. B.1 a). It is placed into the deposition chamber via the load-lock and a transfer arm (Fig. 2.1). The desired mask is attached onto part "c" and transferred into the deposition chamber by the use of part "b" and the transfer arm. After aligning the available grooves on part "c" with the mounting hooks of part "a", the mask is twisted onto the substrate holder. The mask mount is spring-loaded ensuring an intimate pressure contact between the substrate surface and the mask. The stopper prevents part "b" detaching from the transfer arm. For the deposition of a new layer with a different mask, part "c" is removed from the chamber, the mask changed, and placed back into the chamber. Care must be taken for proper alignment of subsequent layers. The currently available masks are shown in Fig. B.2, and can be used for the deposition of a thin film transistor device structure.

References

1. Ted Hinke, OSU Chemistry, provided help with the design and machined the mask.